UNIVERSIDADE FEDERAL DE MINAS GERAIS

INSTITUTO DE CIÊNCIAS EXATAS

PROGRAMA DE PÓS-GRADUAÇÃO EM FÍSICA

RESONANCE RAMAN SPECTROSCOPY IN TWISTED BILAYER GRAPHENE

ELIEL GOMES DA SILVA NETO

Belo Horizonte - MG
Outubro/2017

UNIVERSIDADE FEDERAL DE MINAS GERAIS

INSTITUTO DE CIÊNCIAS EXATAS

PROGRAMA DE PÓS-GRADUAÇÃO EM FÍSICA

RESONANCE RAMAN SPECTROSCOPY IN TWISTED BILAYER GRAPHENE

ELIEL GOMES DA SILVA NETO

Tese de doutorado apresentada ao Programa de Pós-Graduação em Física como requisito parcial para a obtenção do título de Doutor em Física.

ORIENTADOR: PROF. DR. MARCOS ASSUNÇÃO PIMENTA

CO-ORIENTADORA: PROF. DRA. ARIETE RIGHI

Belo Horizonte - MG

Outubro/2017

Contents

List of Figures

List of Tables

Agradecimentos

Agradeço a todos que de alguma forma me ajudaram nessa vida.

Resumo

A compreensão das interações fundamentais em heteroestruturas ultrafinas é crucial para a engenharia de novos dispositivos baseados em materiais bidimensionais (2D). Devido a essas interações surgem novos fenômenos físicos alterando a resposta do material composto em relação às camadas isoladas. Dentre várias técnicas experimentais, a espectroscopia Raman tem desempenhado um papel importante no estudo de materiais 2D, uma vez que os elétrons, os fônons e as interações entre eles podem ser estudados conjuntamente.

Nesta tese, utilizamos a espectroscopia Raman ressonante para estudar essas interações focando em um sistema: o grafeno bicamada girado, sistema composto por duas camadas de grafeno onde a orientação cristalográfica das camadas é diferente, gerando um padrão de moiré . Inicialmente fizemos aquisição de mapas Raman de mais de 100 amostras com distribuição continua de ângulos de desalinhamento entre as camadas de 0 a 30 °, observamos amplificações gigantes da intensidade da banda G (1590 cm^{-}1) do grafeno para amostras em uma faixa intermediária de ângulos de rotação (θ entre 10° e 17°).

As amostras que apresentaram ressonância nos mapas de Raman foram selecionadas para um estudo mais detalhado de perfis de excitação Raman. A análise dos perfis utilizando uma expressão teórica para as intensidades Raman nos permitiu obter as energias das singularidades de van Hove e os parâmetros de amortecimento associados ao processo Raman. Nossos resultados exibem um bom acordo entre energias experimentais e calculadas para as singularidades de van Hove e mostram que o parâmetro de amortecimento não depende do ângulo de desalinhamento na faixa de ângulos intermediários. Observamos que o parâmetro de amortecimento ($\Gamma \approx 250$ meV) é maior do que os obtidos em nanotubos de carbono, estes também apresentam singularidades de van Hove, tanto para o modo de respiração quanto para a banda G. Este resultado é semelhante ao obtido via absorção óptica, sugerindo que os espalhamentos elétron-elétron e elétron-buraco são os mecanismos dominantes.

Observamos o aparecimento de novos fônons nos espectros de Raman e as medidas com diferentes energias de excitação mostram que dois processos de ressonância são responsáveis por tais aparecimentos: o processo de intercamada, onde o espalhamento eletron-fônon ocorre entre estados de camadas diferentes e o processo intracamada que envolve estados na mesma camada de grafeno e um potencial de modulação gerado pelo padrão de moiré.

Com os resultados das medidas de perfis de excitação Raman na região do visível, concluimos que os processos apresentam comportamentos bem distintos. No processo

intercamada, observamos a amplificação da banda G assim como a de outro pico associado ao phonon do ramo transversal óptico do grafeno. Estes dois perfis tem comportamentos similares e estão associados com a ressonância das singularidades de van Hove. Já no processo intracamada, não observamos variação na intensidade da banda G, mas um pico associado ao fônon do ramo longitudinal óptico que apresenta um perfil ressonante.

A energia e o parâmetro de alargamento deste perfil são diferentes quando comparados com os dos perfis do processo intercamada. Desenvolvemos um modelo teórico para explicar ambos os efeitos, em que obtivemos uma grande concordância entre os resultados dos perfis ressonantes. Medidas adicionais nas regiões do infravermelho e ultravioleta foram obtidas. Ao confrontar essas medidas com o resultado teórico, mais uma vez houve um bom acordo entre teoria e experimento.

Afim de comprovar a descrição do processo intracamada, produzimos amostras de grafeno monocamada depositado em cima de um cristal de h-BN. Obtivemos espectros Raman que confirmaram a presença de novos modos ativados pelo processo intracamada elétron-fônon. A possibilidade de distinguir as interações elétron-fônon intracamada e intercamada pela espectroscopia Raman produz uma nova ferramenta para auxiliar na engenharia de heterostruturas em qualquer tipo de dispositivo baseado em grafeno.

Abstract

The understanding of fundamental interactions in ultrathin heterostructures is crucial for engineering novel 2D-based devices. Due to these interactions new physical phenomena arise, altering change the response of the composite material compared with its insulated layers. Among many experimental techniques, Raman spectroscopy has played a major role in 2D materials study, since the electrons, the phonons and the interactions between them can be studied together.

In this thesis, we used resonant Raman spectroscopy to study these interactions focusing on one system: twisted bilayer graphene, a system composed of two layers of graphene where the crystallographic orientation of the layers is different, generating the moiré pattern. Initially we acquired Raman maps of more than 100 samples using visible laser with a continuous distribution of twisting angles from 0 to 30°, we observed huge enhancements of the intensity of G band (1590 cm^{-1}) of graphene for samples in an intermediate range of twisting angles (θ between 10°and 17°).

The samples that showed resonance in the Raman maps were selected for a more detailed study of Raman excitation profiles (REP). The analysis of the profiles using a theoretical expression for the Raman intensities allowed us to obtain the energies of the van Hove singularities and the damping parameters associated with the Raman process. Our results show a good agreement between experimental and calculated energies for van Hove singularities and demonstrate that the damping parameter does not depend on the twisting angle in the range of intermediate angles.

We observed that the damping parameter ($\gamma \approx 250$ meV) is higher than those obtained in carbon nanotubes. They also present van Hove singularities, both for the radial breathing mode and for the G band. The result is similar to the optical absorption, suggesting that electron-electron and electron-hole are the dominant mechanisms.

We observed the appearance of new phonons in the Raman spectra and the measurements with different excitation energies show that two resonance processes are responsible for such appearances: the interlayer process, where the electron-phonon scattering occurs between states of different layers and the intralayer process that involves states in the same graphene layer and a modulation potential generated by the moiré pattern.

With the results of the measurements of REP in the visible region, we conclude that the processes have very different behaviours. In the interlayer process, we observed the enhancement of the G band as well as that of another peak associated to the phonon of the optical transverse branch of the graphene. These two profiles have similar behaviour and are associated with the resonance of van Hove singularities. On the other hand, in

the intralayer process, we did not observe variation in the intensity of the G band, but a peak associated with the phonon of the optical longitudinal branch which presents a resonant profile. The energy and the damping parameter of this profile are different when compared to the interlayer process profiles.

We developed a theoretical model to explain both the effects, in which we obtained a great agreement between the results of the resonant profiles. Additional measurements in the infrared and the ultraviolet regions were obtained. When confronting these measurements with the theoretical result, once again there was a good agreement between theory and experiment.

In order to prove the description of the intralayer process, we produced samples of monolayer graphene deposited on top of a crystal of h-BN. We got Raman spectra that have confirmed the presence of new modes activated by the intralayer electron-phonon process. The possibility of distinguishing the intralayer and the interlayer electron-phonon interactions by the Raman spectroscopy produces a new tool to engineering heterostructures in any type of devices based on graphene.

on a single-layer graphene deposited on the top of h-BN crystal confirmed the presence of new modes activated by the el-ph intralayer process. The possibility of distinguishing intralayer and interlayer el-ph interactions by Raman spectroscopy yields a new tool to engineer electrons and phonons in any kind of graphene-based device. A theoretical model was developed that successfully explains these mechanisms.

1 The Rise of 2D Materials

In the mineralogical classification, many crystals have lamellar morphology. A dominant characteristic in these crystals is the property of having a highly perfect basal cleavage, yielding remarkably thin laminae (sheets). The mica group minerals are known for this property. In the physical point of view, these materials are composed by a stacking of two dimensional(2D) crystals, with a large asymmetry between interactions inside a layer and between atomic layers.

Crystalline graphite is a lamellar crystal presenting an atomically smooth cleavage. Samples of highly oriented pyrolytic graphite (HOPG) are a standard to calibrate scanning probe microscope (LAPSHIN, 1998). Despite the fact that graphite is commonly used to produce samples less than 1 μm of thickness, no one asked: How far can we go in the exfoliation process?. This question was solved in 2004 (NOVOSELOV et al., 2004), when two Russian scientists cleaved the graphite down to obtain a single atomic layer. A. K. Geim and N. S. Novoselov used a Scotch tape to repeatedly exfoliate graphite flakes, with this simple process, they isolated a graphite atomic layer known as graphene. Graphene is the closest you can get from a truly 2D material, with one atom of thickness. For this discovery and fundamental Dirac fermion behaviour of the electrons, they were laureated with the Nobel Prize in Physics in 2010.

This discovery ended a long-lasting theoretical debate about the stability of 2D crystals. According to the so-called Mermin–Wagner theorem (MERMIN, 1968), long-wavelength fluctuations destroy the long range order of 2D crystals. These fluctuations cause a tendency to crumple those 2D materials. However, in 2007 a work showed that intrinsic ripples domains appear in graphene, with typical height displacement sizes of the order of 0,7 Å and typical domain size of 80 Å long. These ripples are responsible for the stability of graphene (FASOLINO; LOS; KATSNELSON, 2007).

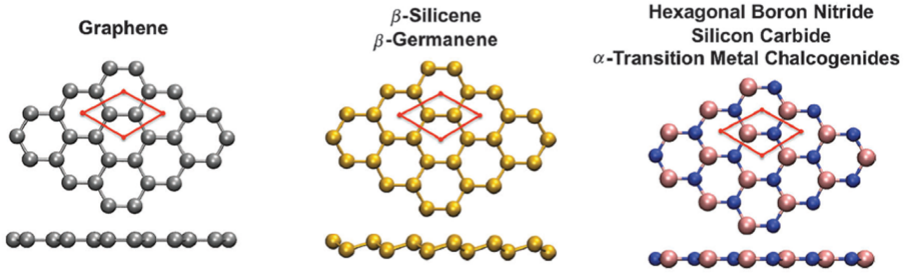

Figure 1 – Atomic structure of atomically thin 2D crystals. Adapted from Ref. (MIRO; AUDIFFRED; HEINE, 2014).

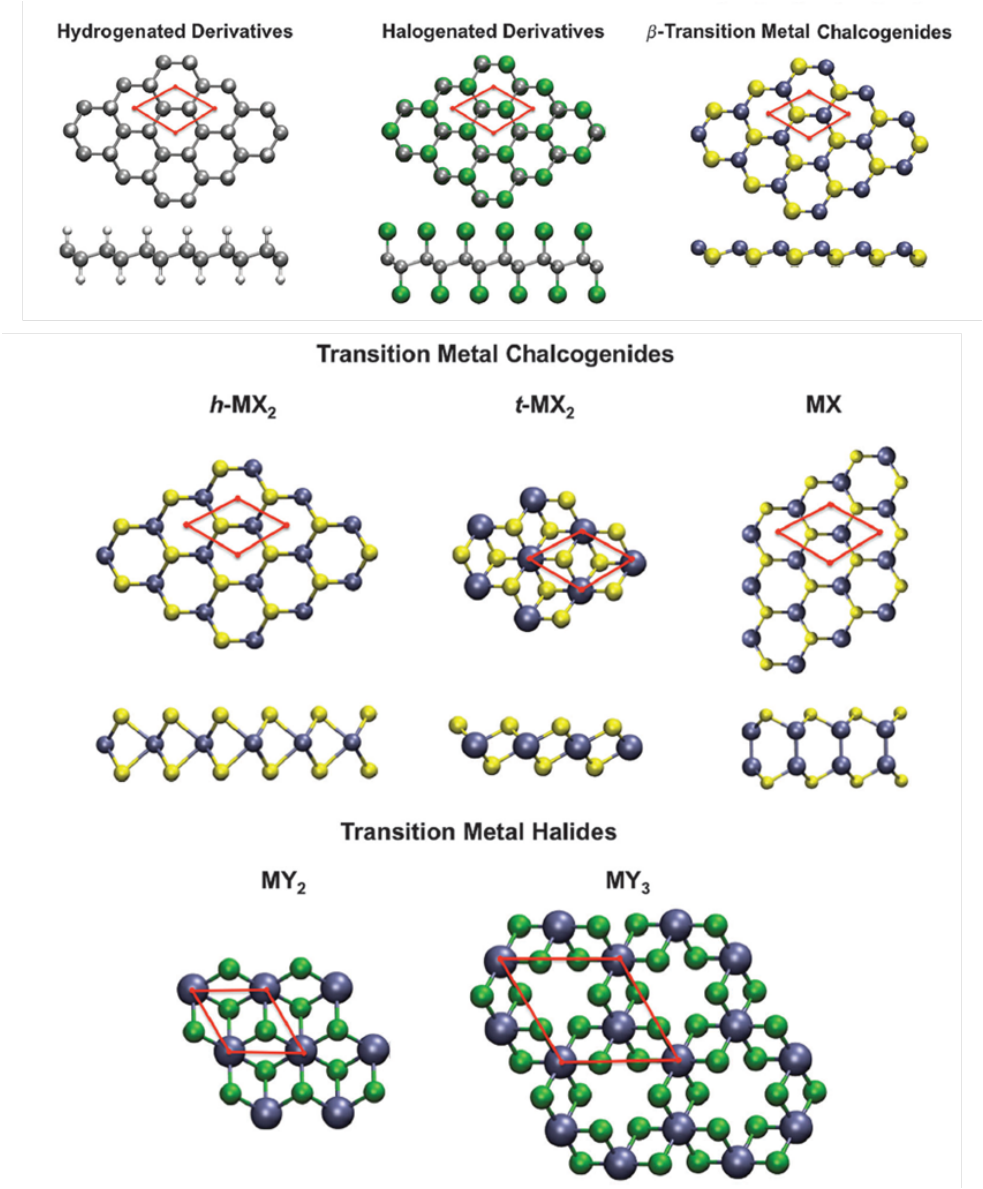

Figure 2 – Atomic structure of some ultrathin 2D crystals. First row presents some derivatives of the atomically thin 2D crystals. M represents the metal, and X(Y) represents the chalcogenides(halides). Adapted from Ref. (MIRO; AUDIFFRED; HEINE, 2014).

Apart from being a 2D material, graphene exhibits outstanding mechanical, electrical and thermal properties, breaking records of charge mobility, thermal conductivity and Young‘s modulus. Naturally, the scientific community searched for other lamellar crystals and applied the same mechanical exfoliation technique to obtain other 2D crystals. In parallel, modern synthetic methods as chemical vapor deposition (CVD) and epitaxial grown techniques have been successfully used to produce graphene and other 2D materials. Nowadays a considerable number of 2D materials can be obtained or synthesized, creating a demand of theoretical models for the understanding of basic properties in these materials, such as electronic, thermal, magnetic and others. The article entitled "An atlas of two-dimensional materials" summarises the combined effort of groups in the calculation of the electronic structures for different 2D crystals (MIRO; AUDIFFRED; HEINE, 2014). The article presents: 28 atomically thin, some are shown in Figure 1; 88 ultrathin (few atoms of height) 2D materials, some examples are shown in Figure 2. Not all of them have been experimentally obtained, and also more 2D materials can exists.

The possibility of assembling materials with diverse electronic behaviour, from metallic to insulator, allows the creation of ultrathin devices. The combination of different materials is called heterostructure and they can be combined in two ways: in-plane or stacking. In a paper published by the Nobel Prize, A. K. Geim, and I. Grigorieva, a discussion about stacking these materials to create van der Waals heterostructures is presented (GEIM; GRIGORIEVA, 2013). These structures are made by a pile of 2D crystals, which are kept together by van der Waals forces. We can for example create a MOSFET by piling a semiconductor, like MoS_2, an insulator (h-BN) and graphene as a conductor. An illustration showing this idea is presented in Figure 3. Comparing to a LEGO, one can stack blocks to build very complex structures. However, physical systems are much richer than LEGO bricks, since the angle between adjacent layers can change electronic properties. This creates the possibility of an angle stacking engineering. Motivated by these new discoveries, the goal of this PhD thesis is understanding, using resonance Raman spectroscopy, how stacking graphene can affect the electronic and vibrational properties.

The structure of this thesis is divided in the following chapters. In chapter 2 we discuss the structural characteristics of graphene, focusing on its electronic and phonon structures and the behaviour of these properties in bilayer graphene and twisted bilayer graphene (TBG). Chapter 3 introduces the concept of Raman spectroscopy and discusses the quantum model for Raman effect. The experimental setups used in this work are also presented. In chapter 4, a brief summary of the Raman effect in graphene is presented. A review of Raman studies in TBG system is also presented. And finally we present the samples used and measurement protocols to guarantee good results. In chapter 5, 6 and 7, we present the results obtained during this PhD. Chapter 5 presents the enhancement of the G band in TBG.We discuss the dependence of G band intensity and width in function of twisting angle in order to prove the theoretical models. In chapter 6, the Raman excitation

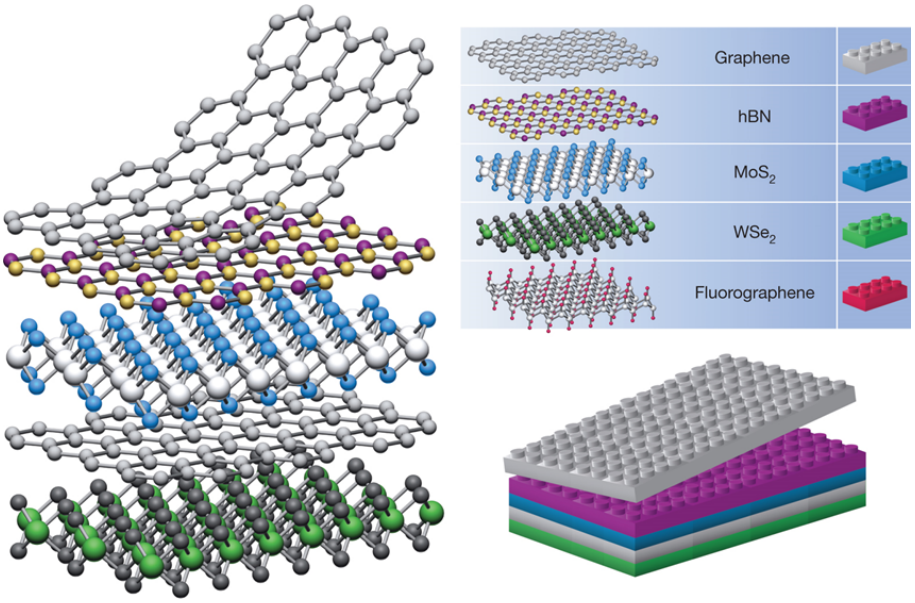

Figure 3 – Analogue between van der Waals and LEGO, showing that devices can be construct as a block building. Adapted from Ref. (GEIM; GRIGORIEVA, 2013).

profile of the G-band enhancement in twisted bilayer graphene is presented. We show the Raman Excitation Profile (REP) for the G band using a multiple excitation Raman spectra. The energy and damping constants are obtained for the first time for more than 10 samples. And finally the chapter 7 named "The Intralayer and the Interlayer Electron-Phonon Interactions in Twisted Graphene Heterostructures". We explain that new phonons in TBG systems are generated via two different processes, intralayer and interlayer. These processes have different physical origins and activation energies. In conclusions and perspectives, we present the main finding that we obtained studying this system and future works.

2 Graphene

In this chapter we will briefly cover a little of the history of the carbon crystals up to the point when graphene was obtained, and we will also discuss some fundamental properties needed to describe the system that we studied in this work, the TBG, focusing on the understanding of the electronic and phonon dispersions in these systems.

2.1 History

Crystalline carbon systems can be found mostly in two forms in nature, diamond and graphite. The atomic structure of diamond is made of tetrahedrally bonded carbon atoms in a covalent network (sp^3). Diamond has unique properties such as hardness of 167 GPa (BLANK et al., 1998), the highest known in natural materials, and very high thermal conductivity (900-2300 $Wm1K^1$) (WEI et al., 1993). Also, it has a wide band gap of 5.5 eV, which explains its transparency. Besides these properties, diamond is a metastable material in standard ambient temperature and pressure (SATP).

Graphite is the most stable form of crystalline carbon in SATP and is formed by stacking layers of hexagonal carbon arrays (honeycomb lattice) that are covalently bonded in the sp^2 configuration. The layers are connected to each other by van der Waals forces, which are very weak compared to the intralayer force. The asymmetry between intralayer and interlayer interactions makes graphite extremely anisotropic, presenting different properties (e.g. electrical conductivity, thermal conductivity, acoustic wave propagation) in the basal plane and in the perpendicular direction. The electrons are delocalized across the basal planes and are responsible for electrical conductivity. A notable consequence of the weak interlayer van der Waals interactions is that a layer can slip over each other. Because of this property, graphite is used as a dry lubricant. Other commercial applications of graphite include batteries, metallurgy, arts, fuel etc.

In the research area of carbon materials, the interest increased significantly after the discovery of new carbon systems, such as the fullerenes, which was discovered in 1985 by Kroto *et al.* (Kroto et al., 1985), a 0D material made of carbons in sp^2 configuration. Few years later, in 1991, another structure of carbon was discovered: the carbon nanotubes. These systems are formed by a tubular structure of carbon atoms and they are considered as 1D form of sp^2 carbon (IIJIMA, 1991). These new materials present a large number of effects and applications. For example, carbon nanotube was the first material to display metallic and semiconducting properties in SATP depending on the tube chirality (SAITO et al., 1992; PIMENTA et al., 1998). It exhibits big Youngs̀ modulus (TREACY; EBBESEN; GIBSON, 1996) and a high thermal conductivity (CHOI et al., 2006).

These materials were hot topics in between 1990s and 2000s in fundamental science. Nowadays a large number of applications are being developed. In the case of nanotubes, the improvement in methodology of chirality separation allowed an increasing number of devices. An example of large-scale devices can be found in the following references (VIJAYARAGHAVAN et al., 2007; KIM et al., 2017).

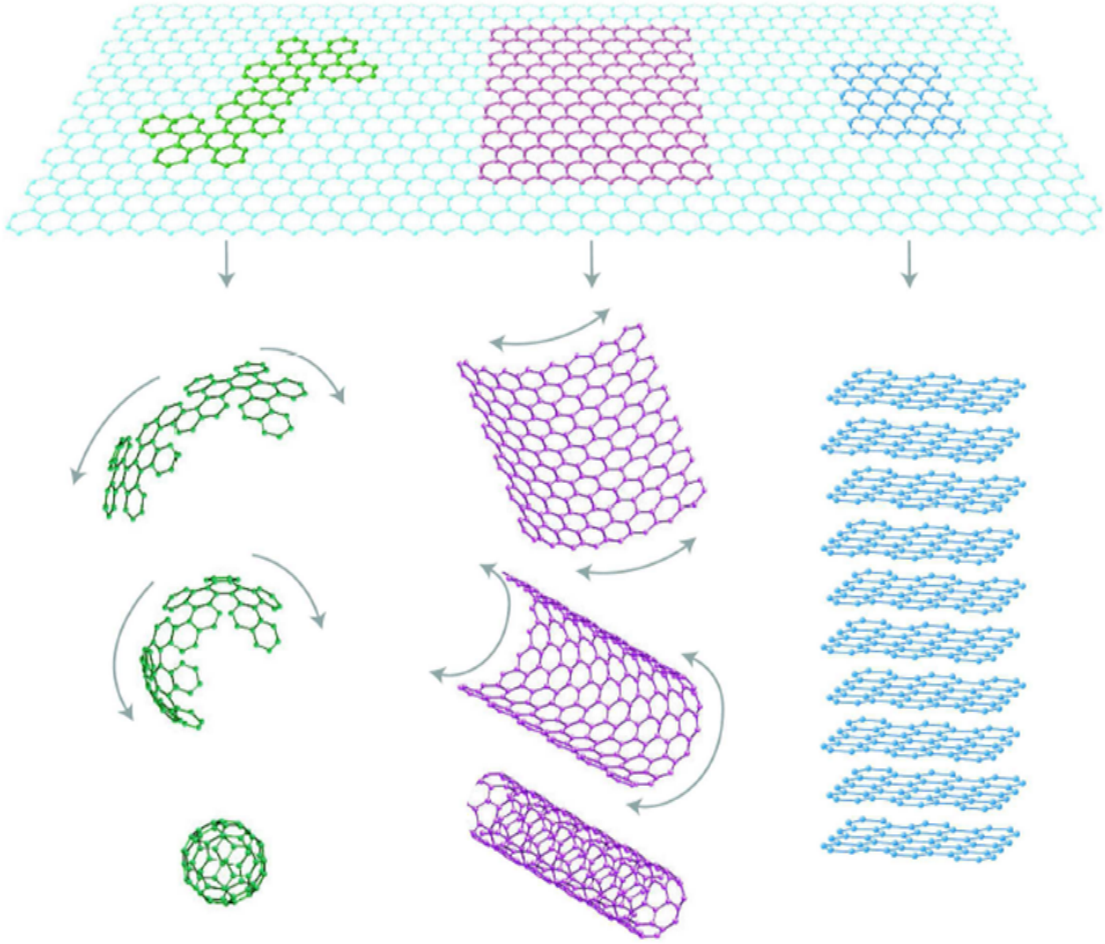

Figure 4 – Illustration representing how fullerenes, nanotubes and graphite can rise from graphene, adapted from Ref. (GEIM; NOVOSELOV, 2007).

Graphene is the newest material of the carbon family, and it is the 2D form of sp^2 carbon. In other words, graphene is an isolated graphite layer. A number of research groups migrated to this field, to study the chemical, mechanical, electrical, optical and optoelectronic properties of these materials using a large number of different techniques.

Besides being the last one to be discovered experimentally, the electronic structure of graphene was already calculated 70 years ago (WALLACE, 1947). It is important understanding graphene theoretically to obtain information about the other sp^2 carbon materials. Figure 4 shows how graphene is related to the other sp^2 carbon materials. The next sections discuss concepts necessary to understand its physics properties.

2.2 Graphene Structure

The graphene crystal is a honeycomb lattice made of covalent bonded sp^2 carbon atoms. The graphene properties can be better understood by explaining its structure. The unit cell of monolayer graphene has two carbon atoms 1(A) and 2(B), each one forming a triangular sublattice as presented in Figure 5(a).

The primitive vectors $\vec{a_1}$ and $\vec{a_2}$ in Figure 5(a) can be written in Cartesian coordinates as:

$$\vec{a}_1 = \left(\frac{\sqrt{3}a}{2}, \frac{a}{2}\right) \quad \vec{a}_2 = \left(-\frac{\sqrt{3}a}{2}, \frac{a}{2}\right) \quad , \tag{2.1}$$

where $|\vec{a}_1| = |\vec{a}_1| = a = 2,46\text{Å}$ is the lattice parameter of a monolayer graphene. Using these vectors, we can obtain the reciprocal lattice vectors with the orthogonality relations:

$$\vec{b_i} \cdot \vec{a_j} = 2\pi\delta_{ij} \quad , \tag{2.2}$$

where $\vec{b_i}$ is the primitive vector of the reciprocal lattice. From this relation, we obtain the vectors of the reciprocal network, $\vec{b_1}$ and $\vec{b_2}$, which are given by:

$$\vec{b}_1 = \left(\frac{2\pi}{\sqrt{3}a}, \frac{2\pi}{a}\right) \quad \vec{b}_2 = \left(-\frac{2\pi}{\sqrt{3}a}, \frac{2\pi}{a}\right) \quad . \tag{2.3}$$

Figure 5(b) shows these vectors. The first Brillouin zone of graphene and the high symmetry lines and points, such as the Γ point, in the origin of the Brillouin zone, the K points, at the corners of the hexagon, and the M points, located in the center of the borders.

2.3 Electronic Structure

In this section we will briefly discuss the electronic structure of graphene, for a better understanding of the Raman process. Initially, Solving the electronic structure of graphene was very important for the understanding the electronic properties of graphite. In the first approaches, calculations were made using the tight-binding approximation. Wallace was the first to calculate (WALLACE, 1947), but only in the 70s, the first principles calculations were reported by Ellis and Painter (PAINTER; ELLIS, 1970).

Nowadays, modern computers make first principle method increasingly viable, that can solve more sophisticated interactions, like many-body interactions, such as electron-electron and electron-hole interactions. This refinement in calculations makes them very costly in time. In practice, a common way to make these calculations temporally viable

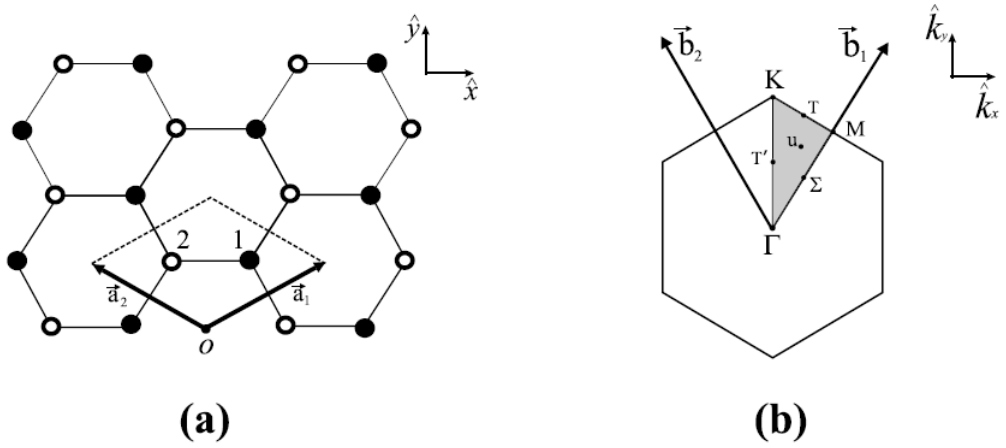

Figure 5 – (a) Graphene lattice and the primitive vectors $\vec{a}_1, \vec{a}_2$ of the unit cell. (b) First Brillouin zone of graphene with its primitive vectors and high symmetry points Γ, M and K

is a two steps approach: first, a very good calculation via first principles, then use a tight-binding method of higher order and to search the tight-binding parameters that replicate the first principle's results. In this way, we can use tight-binding approximation in problems that are too complex for first principle method, such as obtaining a theoretical Raman spectra.

In this thesis, we used a fifth-order approximation developed by P. Venezuela (VENEZUELA; LAZZERI; MAURI, 2011). This calculation reproduces well the calculated structure through density functional theory (DFT) with GW approximation for many-body system of electrons.

Figure 6 presents the electronic structure for the π electrons of graphene. Two peculiarities can be noticed. The first one is the K point where the valence and conduction bands touch each other. The density of electronic states (DOS) is null exactly at this point for a undoped graphene, that corresponds to the Fermi level. Therefore the graphene is a zero gap semiconductor. The second interesting effect is the linear dispersion near the K point, similar to the light's dispersion. As consequence, the electrons behave like massless Dirac fermions in energies near the point K, making it an interesting system to study quantum electrodynamics (NETO et al., 2009). Another consequence of the linear dispersion appears in electrical measurements, that show that the mobility of graphene is superior than $200,000\ \mathrm{cm}^2(\mathrm{Vs})^{-1}$, the highest value among all materials. Measurements realised with suspended graphene have shown an even higher mobility and a smooth curvature in this dispersion near to the K point(ELIAS et al., 2011).

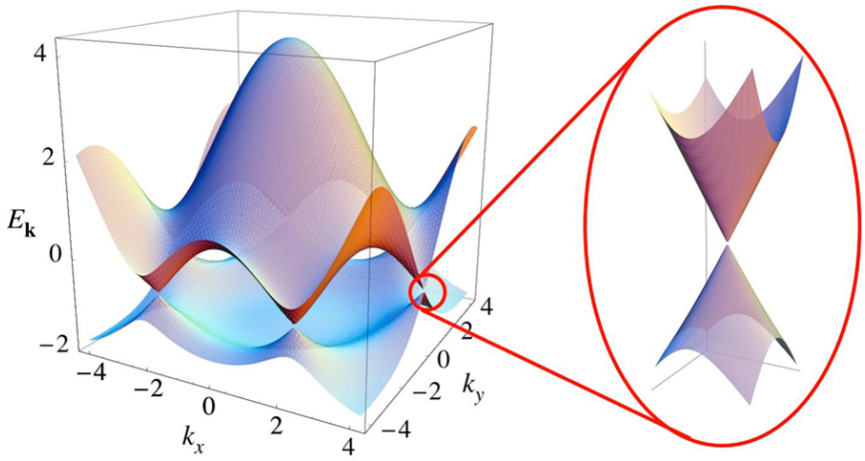

Figure 6 – (left) Graphene electronic structure for π electrons calculated via second order tight-binding. (right) Zoom near to the K point showing the linear dispersion. Adapted from (NETO et al., 2009)

2.4 Phonon Structure

For the development of our work, another factor of crucial importance is the phonon dispersion. The behavior of phonons plays a key role in the interpretation of the Raman spectra. Phonons are fundamental to understand material properties such as vibrations, thermal properties and acoustic waves propagation. Also, in systems with ballistic transport conditions, phonons are one of the main electron scattering mechanisms making their understanding of great value for electronic transport studies (Nika; Balandin, 2012).

Single layer graphene (SLG) presents 2 atoms per unit cell, and it has 6 phonon branches, 3 acoustic (A) phonons (iTA, iLA, oTA) and 3 optical (O) phonons (iTO, iLO, oTO) are expected (JORIO et al., 2011). The phonons with index "i" and "o" refer to in-plane and out-of-plane vibrations, respectively. The index L means that the vibrations are longitudinal, while the T is used to represent transverse vibrations. Figure 7 represents the surface cuts of the phonon dispersion along the lines of high symmetry in the directions ΓKMΓ (SAITO et al., 1992).

Acoustic phonons are important for understanding the thermal properties of the materials. In the case of graphene, the iTA and iLA phonons are the dominant ones because their group velocity is very high, as it can be seen in the Figure 7. The slope of the phonon dispersion near the point Γ is very high, causing the sound speed in the graphene layer to be of the order of 21 km/s (Nika; Balandin, 2012; JORIO et al., 2011). The thermal conductivity of the graphene is also high. The room temperature value is around 5x10^3 W/mK(BALANDIN et al., 2008).

At the Γ point, the in-plane optical modes are degenerate, and these phonons have high energy (1585 cm^{-1}), due to the small mass of the carbon atoms and a high

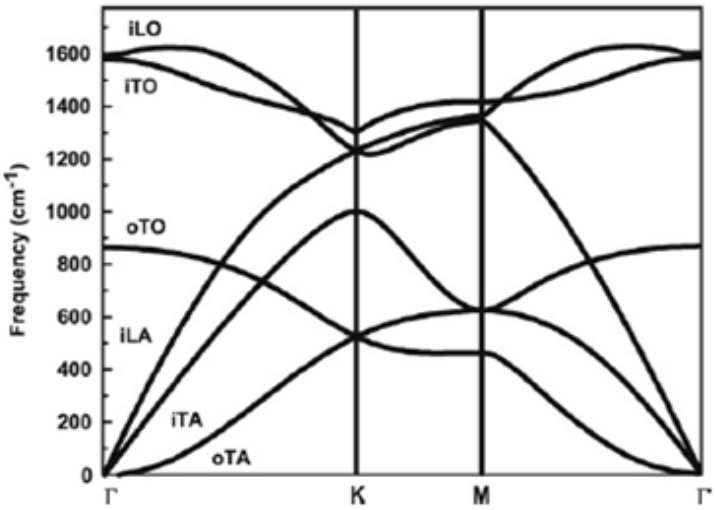

Figure 7 – Phonon dispersion curves of 2D graphite for the high symmetry points and lines in the first Brillouin zone. Adapted from (JORIO et al., 2011)

spring force constant between the adjacent atoms A and B. This vibration is very fast, with a period of 21 fs, it was verified experimentally using coherent phonon generation in a non-degenerate pump-probe scheme (HARTSCHUH, 2008). The dynamics of the processes between electron-electron, electron-phonon and electron-defects are of the order of hundreds of femtoseconds. Moreover, electrons and phonons are strongly coupled, causing the phonon carry an immense amount of information related with: electrical (dopage, defects...), thermal (thermal conductivity, temperature...) and structural (strains, presence of other atoms...) properties (JORIO et al., 2011).

Three techniques are the most common to probe phonons. The first is the inelastic slow neutron scattering, where the neutron interacts directly with the atoms nuclei. This technique can map all phonons in Brillouin zone by tuning the neutron wavelength (). The other two techniques are optical: infrared (IR) spectroscopy which directly measure the light absorption by a vibration mode, and Raman spectroscopy that measures the inelastic scattering of light via phonon through electron-phonon process.

In these optical processes, not all phonons can be observed, since the phonon symmetry selection rule plays a major role in which vibration can be observed. Depending on the vibration symmetry, a phonon can be measured by IR spectroscopy, Raman spectroscopy, by both techniques or none of them. In the last case, the phonon is called silent. For ordinary lasers, the light momentum is much smaller than a typical Brillouin zone, so in principle, optical processes can probe only phonons in the center of Brillouin zone. However, optical techniques are easier and faster than neutron technique.

2.5 Twisted Bilayer Graphene

We start this section with a brief discussion of the most common type of bilayer graphene sample, the Bernal stacked graphene also called AB stacked graphene.

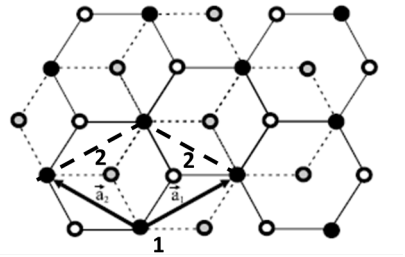

Figure 8 – Atomic structure of Bernal stacked bilayer graphene.

The structure of the Bernal bilayer graphene is shown in Figure 8. It contains 4 atoms per unit cell. Despite this bilayer having the same unit cell size as SLG, it exhibits a totally different electronic behaviour than SLG (NETO et al., 2009; MCCANN; FAL'KO, 2006). The electronic structure has a parabolic dispersion near to K points, as presented in Figure 9. Due to this difference, the behaviour of the electrons in Bernal stacked bilayer graphene is very different than SLG one.

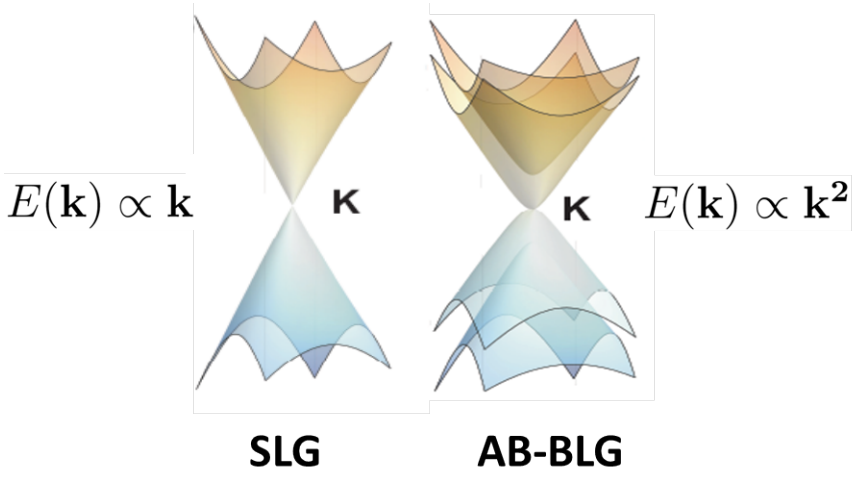

Figure 9 – Electronic structures near to the K point of a single layer graphene (left side), Bernal stacked bilayer graphene (right side).(NETO et al., 2009)

In the case of phonon structure, each phonon branch splits in two branches. However, the weak coupling between the layers causes a very small split, around 5 cm^{-1} in the Γ point of optical phonons (YAN; RUAN; CHOU, 2008).

Some samples of few layers graphene show unusual behaviour compared to AB stacked graphene. In epitaxial graphene over SiC, Scanning tunneling microscope (STM) measurements show moiré patterns generated by the misorientation of the graphene layers,

as shown in Figure 10 (BERGER et al., 2006; HASS et al., 2008). The black diamonds in Figure 10 (b) and (c) represent the moiré cell, which can be obtained by the visualization of the modulation in the electronic potential. Additionally, non AB stacked graphene based systems are also produced by folding exfoliated graphene (SCHMIDT et al., 2008) and by the deposition of graphene on graphite (LI; LUICAN; ANDREI, 2009). When the number of graphene layer is two (bilayer graphene), these systems are called TBG.

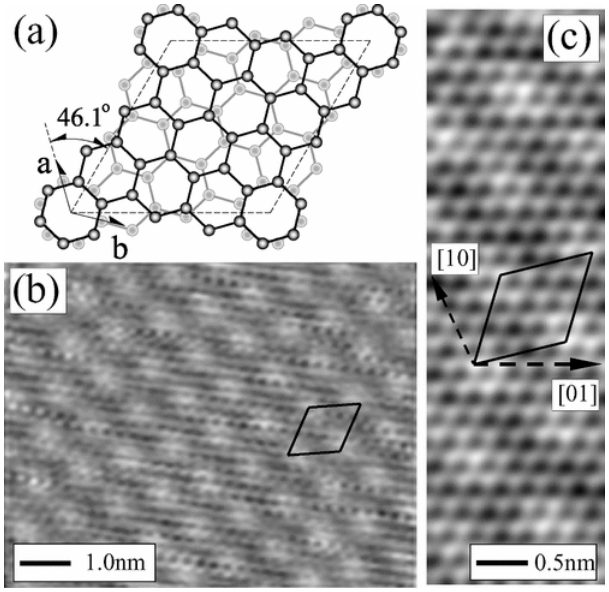

Figure 10 – (a) Schematic graphene superlattice with primitive vectors, in dark the top layer and in gray the bottom one. (b) STM image in the C-face of the SiC showing the superlattice. (c) High resolution STM image. (HASS et al., 2008)

One year after the observation of those TBG samples, a continuum theoretical model that describes the electronic structure for any angle mismatch was developed by Dos Santos *et al.* (SANTOS; PERES; NETO, 2007). They observed that the linear dispersion behaviour of SLG is preserved in the TBG for small angles as well as a decrease in the Fermi velocity, that is stronger in small angles. Li *et al.* have shown that this interaction between the Dirac cones of the two layers generates van Hove singularities (vHs) in these systems (LI et al., 2009). Moreover, the energy separation between the vHs in the valence and conduction bands changes almost linearly with the sample angle. Figure 11 summarizes the continuum model. Figure 11 (a) represents the first Brillouin zones of the two layers, one rotated relative to the other, and the Δk is the distance between two nearest Dirac cones. Figure 11 (b) shows the two Dirac cones superposition. The coupling between the Dirac cones generates an anti-crossing effect, which gives rise to the van Hove singularity shown in Figure 11 (c).

It is possible to relate the energy difference between the van Hove singularities as a function of the angle for the linear dispersion region using the following equation (KIM et

al., 2012):

$$sin(\theta/2) = \frac{\Delta k}{2K} = \frac{3aE_{vHs}}{8\pi\hbar v_f} \quad , \tag{2.4}$$

where θ is the angle, v_f is the Fermi velocity, a is the lattice parameter, E_{VHs} is the energy difference between the van Hove singularities. Δk and K are defined in Figure 11.

In the theoretical studies we highlight some important contributions. First, E. J. Mele have shown that samples with angle θ and 60-θ, with θ in a 0°to 30°range, have the same size of moiré cell, electronic structure calculations for a θ and 60-θ pair only present difference for energies close to fermi level, around 10 meV for 20°case. but this difference becomes stronger in the limit $\theta \to 0$, the AB(60) and AA(0) case (MELE, 2010).

Sato *et al.*, using tight-binding calculations, propose a large number of resonance families like carbon nanotubes in TBG (SATO et al., 2012). The family is given by the difference between m and n, where m and n are the parameters of the translation vector $\vec{T}_{TW}$ ($\vec{T}_{TW} = m\vec{a}_1 + n\vec{a}_2$). Figure 12 (a) presents the unit cell of the superlattice and the vector $\vec{T}_{TW}$. Note that its size is determined as function of n and m as in the case of nanotubes. The size of the unit cell can be obtained by the following equation:

$$L = a\sqrt{m^2 + n^2 + mn} = \frac{|m-n|\,a}{2sin\theta} \quad . \tag{2.5}$$

Using this discrete model, they obtain the energy difference for the van Hove singularities for the first and second resonance, for each family presented in Figure 12 (b). The first resonance has the same energy of calculated by dos Santos *et al.* (SANTOS; PERES; NETO, 2007). On the other hand, this second resonance has higher energy

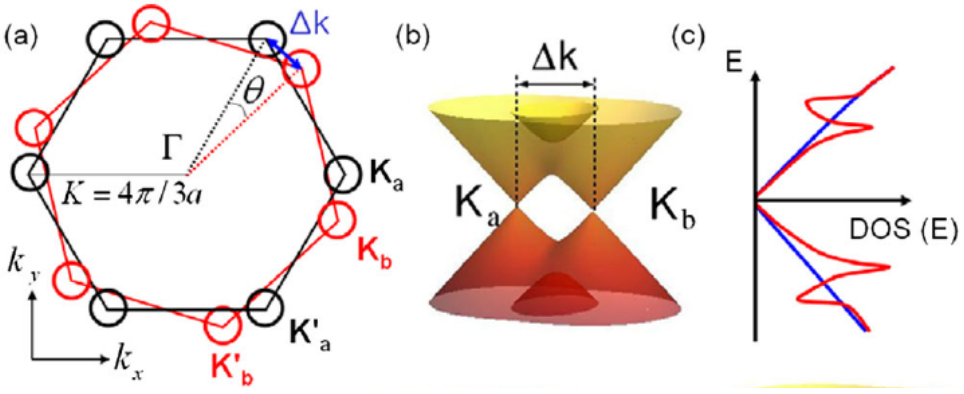

Figure 11 – (a) Brillouin zone of two graphene layers twisted by an angle θ, (b) Dirac cones of two layers showing their coupling. (c) Schematic density of states presenting the singularities in the energy which the cones intercept each other. (KIM et al., 2012)

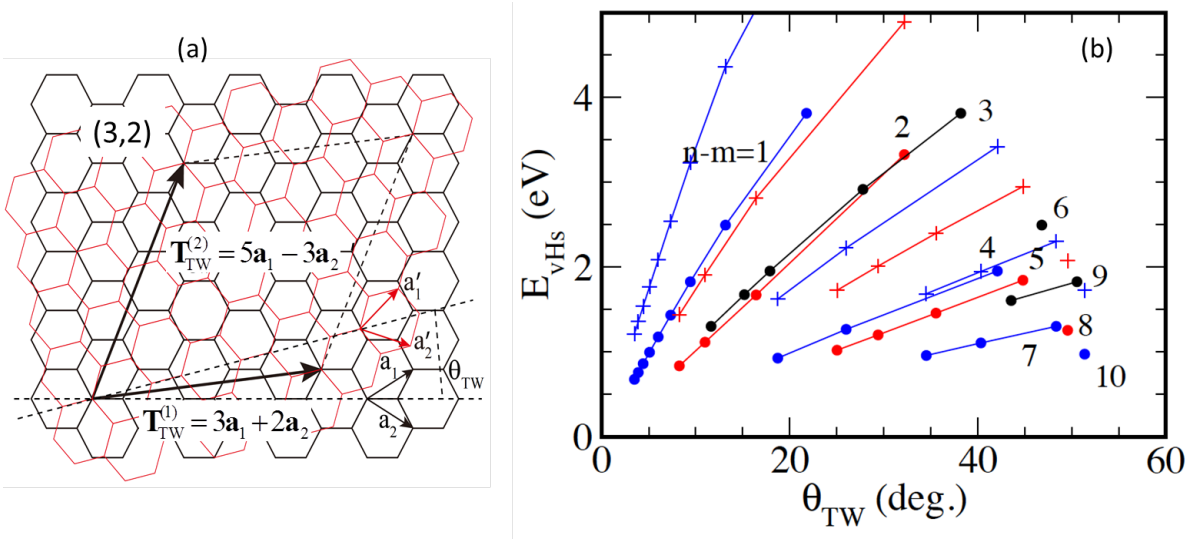

Figure 12 – (a) Two layers of graphene with an twisting angle θ. The parameters m and n are used to measure the superlattice period. (b) The energy separation at the van Hove singularity point as a function of the twisted angle. The numbers near to the curves represents the families of $m - n$, Circle and plus symbols represents E_{11} and E_{22} respectively (SATO et al., 2012)

difference between the van Hove singularities, similar as carbon nanotubes. Note that E_{22} for $|m - n| = 2$ is very close to E_{11} of the $|m - n| = 1$ family.

Using tight binding calculations and an effective continuum model to study commensurate angle TBGs, Moon and Koshino showed that in the continuum case the important cell sizer is the Moiré cell, which is given by(SHALLCROSS et al., 2010):

$$L_M = \frac{a}{2sin\theta} \quad . \tag{2.6}$$

Equation 2.6 shows that, for a commensurate angle, the moiré cell size is not necessarily the same as the unit cell, In fact they can be related by the expression:

$$L_M = \frac{L}{|m - n|} \quad . \tag{2.7}$$

Figure 13 shows moiré and the unit cell for three different commensurate angles. Note that for the (5,7) TBG structure, in the middle of Figure 13, $|m - n| \neq 1$. The moiré cell has half of unit cell size, as a consequence the moiré cell is quasi periodic pattern in those cases.

Moon and Koshino also reported the DOS for commensurate angles and it is shown in Figure 14(a). The van Hove singularity energies increase with increasing twisting angle. For the angle range shown in Figure 14(b), the dependence of the energy on angle for the optical conductivity is linear, which is interesting, since it corresponds to the range

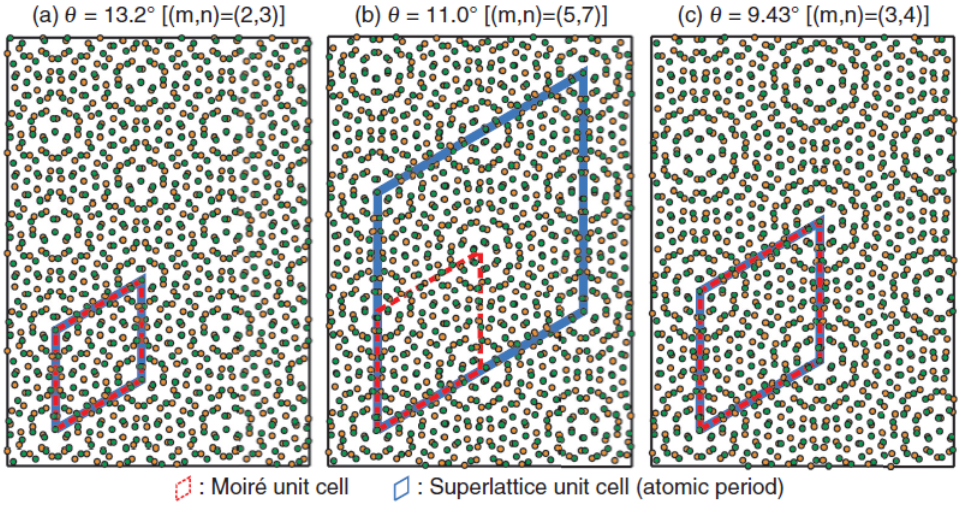

Figure 13 – Atomic Structure of TBG with angles (a) $\theta = 13.2°$ (b) $\theta = 11°$ (c) $\theta = 9.43°$, Dashed (red) and Solid (blue) correspond to the Moiré cell and the superlattice unit cell, respectively.(MOON; KOSHINO, 2013)

that we can measure using a laser in visible range. This energy is very close to the energy presented in Figure 12 for E_{11} when $|m - n| = 1$ (MOON; KOSHINO, 2013). Also, for the angle of 11 degrees, it is equivalent to a (5,7) TBG, a tiny peak is observed in similar energy as E_{11} for $|m - n| = 2$ predicted by Sato *et al.* for this angle.

Comparing the results of the dynamical conductivity for commensurate angles, they concluded that the continuum model describes quite well the energy of the main peak that appear, see Figure 14(b). This quantity is directly related to the optical absorption. However the continuum model does not encounter a split that appears in that peak for angles above 10°. Also, Figure 14 (b) shows that when $m - n > 1$ the signatures of unit cell are weak. Again, comparing with Figure 12, we do not expect to see E_{11} for $|m - n| > 1$ because the unit cell signature may not be detected using Raman technique. Note that E_{22} for $|m - n| = 2$ is very close to the continuum model energy.

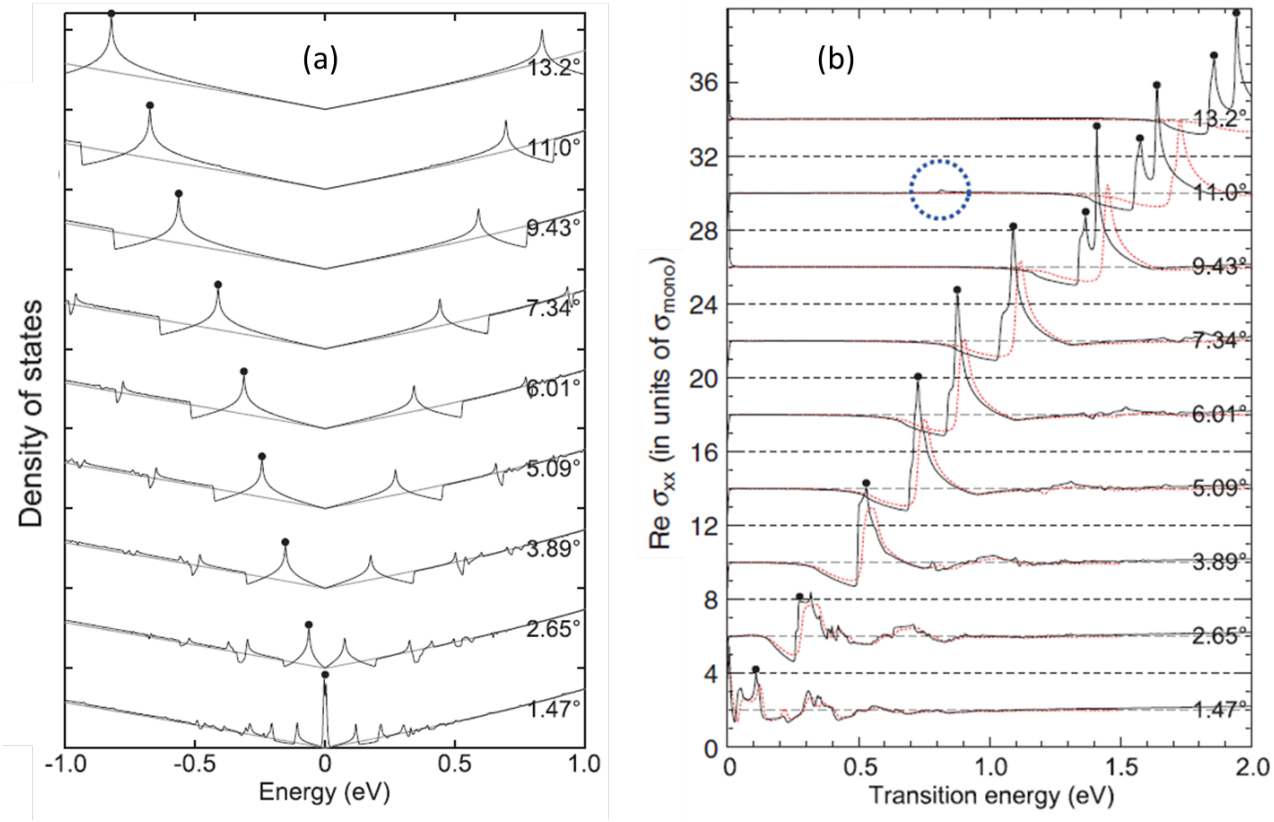

Figure 14 – (a) DOS of TBG (black) with various rotation angles, and uncoupled bilayer graphene (gray) (i.e., twice the monolayer's DOS), black dot marks the van Hove singularity. (b) Real part of the dynamical conductivity, in black the discrete model and in red the continuum model. Both models agree very well for small angles. The blue dashed circle represents one peak that only appears in the discrete model. At the angle of 11°, we have m=5 and n=7, so this peak is the signature of the bigger structure(MOON; KOSHINO, 2013).

3 Raman Spectroscopy

Raman spectroscopy is an optical technique that consists in illuminating a sample with light, usually a laser, and evaluating the inelastic scattering. Using momentum and energy conservation some physical properties of the sample can be obtained as the vibrational and rotational properties and other low energy effects.

3.1 History

The inelastic light scattering was firstly predicted by Adolf Smekal in 1923 (SMEKAL, 1923), and it was observed experimentally few years later by C. V. Raman and K. S. Krishnan in 1928 (RAMAN; KRISHNAN, 1928).

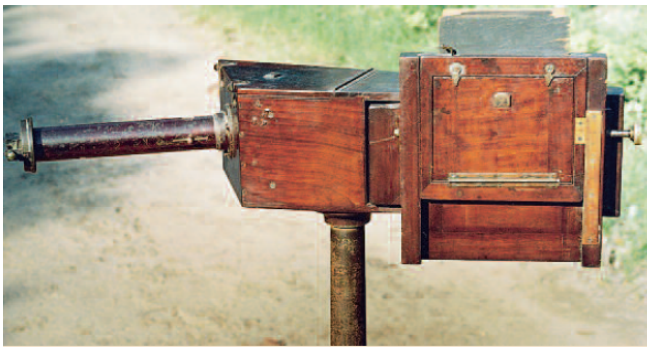

Figure 15 – Photo of the Raman's original setup in 1928. (ACS; IACS, 1998)

The setup consists of a telescope, a chamber and two filters. Its photo is shown in Figure 15. The filters were chosen in such a way that the incident light is totally extinguished when they are coupled. Figure 16 illustrates this process. When the sunlight passes through a violet filter, then through a liquid/gas sample, the majority of the emergent light has the same energy of the incident beam. This process is so-called Rayleigh scattering. However, a small portion of the scattered light has a different colour, and in this way, some light can be observed with the insertion of a green filter after the fluid.

With this setup, Raman and Krishnan observed this effect for more than 60 different fluids, and all showed the same result — some scattered light had a different colour than the incident light. Since other optical effects can change the energy of the light, like luminescence, the fact that this effect was observed in a large number of samples guarantees that it is a scattering effect. Raman and Krishnan reported that two characteristics are important to differentiate the reported scattering from luminescence: the scattered intensity, which is much smaller for their process, and the strong polarization dependence of this scattering process. In virtue of this scattering investigations, C. V.

Raman was honoured with Nobel Prize in Physics in 1930 and the process is now known as Raman scattering.

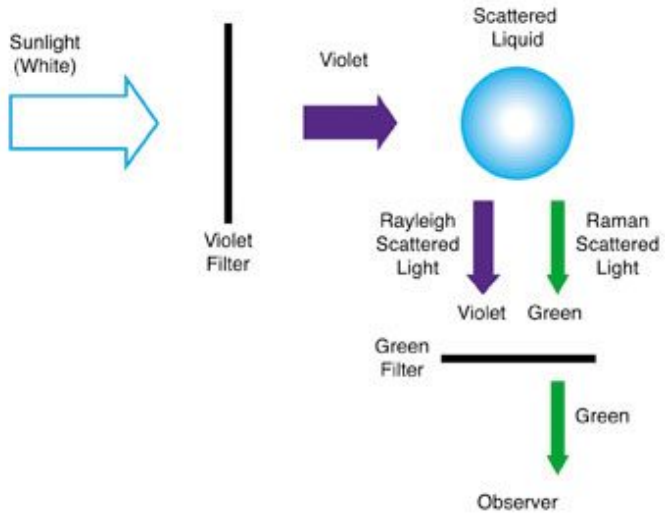

Figure 16 – Illustration of Raman's experiment. (ACS; IACS, 1998)

The following years after Raman and Krishnan's publication, better technologies became available, like mercury arc lamps, and a good quality glass prism. Using these equipments, Raman and Krishnan have performed a more quantitative study, in which they showed that the wavelength generated by each sample was different. Proving that Raman scattering can be used for identification of samples.

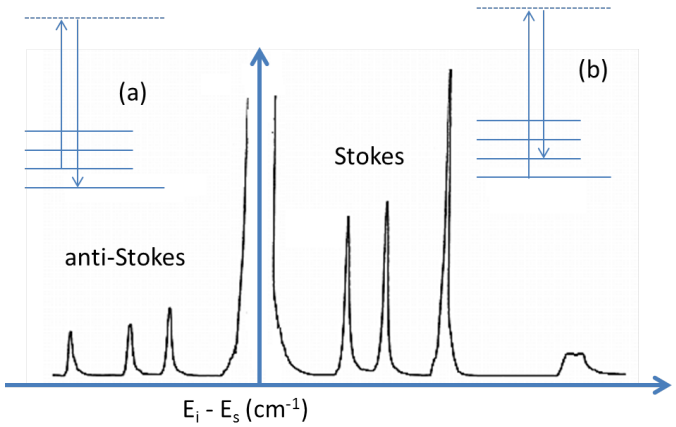

Figure 17 – Typical Raman spectrum, the peak in the middle is related with the Rayleigh scattering, negative x axis peaks are generated via an anti-Stokes process shown in diagram (a) and positive x axis peaks are generated via a Stokes process (b)

In 1930's and 1940's, Raman spectroscopy was used to characterize the vibrational spectra in molecules. However, due to the very weak intensity of the scattered light, measuring the Raman spectrum was a hard task. Nowadays, with the big advance in the field of instrumentation spectroscopy, such as lasers, diffraction gratings, CCD detectors

and better filters, the detection of Raman signals is much faster and effective. Considering its high selectivity of the Raman spectroscopy, it plays a major role in the characterization area, and it has been extensively used in the field of modern material science.

Figure 17 shows an usual Raman spectrum. In the center of the spectrum, it showed the scattered light with the same energy of the incident light, the so-called Rayleigh scattering region, a region of higher energy is called anti-Stokes spectrum (diagram (a)) and a region of lower energy is called Stokes spectrum(diagram (b)). The physical difference between Stokes and anti-Stokes process is related to the creation (Stokes) or annihilation (anti-Stokes) of phonons.

3.2 Quantum Theory of Raman Scattering

The description of the first order Raman effect for crystals from the point of view of quantum mechanics is based on the third order perturbation theory and the Fermi golden rule of the Raman scattering.

The Raman process can be described as follows: the incident photon (ω_λ) interacts with the sample i.e. an electron, changing the electronic state to $|n\rangle$. The electron then interacts with a phonon, changing the electronic state to $|n'\rangle$, emitting a phonon (ω_{ph}). Finally the electron recombines with the hole and a scattered photon (ω_s) is emitted. These steps can occur in any temporal order.

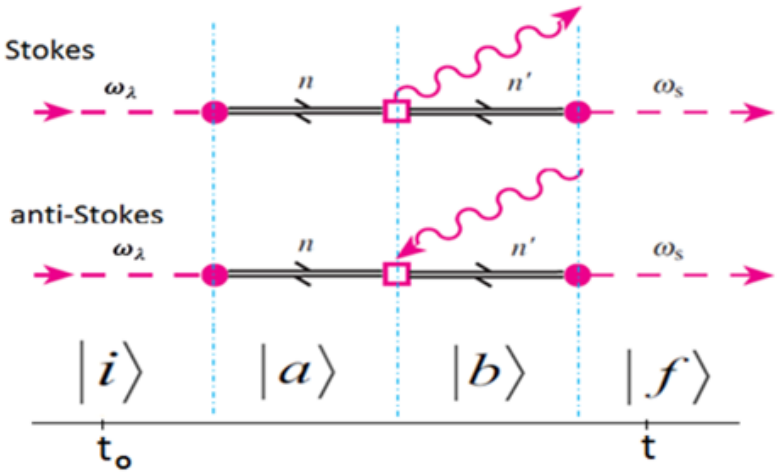

Figure 18 – Diagram representing the first order Raman effect for the Stokes and anti-Stokes processes, in this specific temporal order, the effects are: absorption of a photon, creation/annihilation of a phonon and emission of a photon.

In order to describe this process using the perturbative approach, one needs to

consider the following Halmiltonian:

$$\begin{aligned} H &= H_0 + H_1 \quad , \\ H_0 &= H_C + H_R \quad , \\ H_1 &= H_{e-r} + H_{e-ph} \quad , \end{aligned} \tag{3.1}$$

where the non-pertubated Halmitonian H_0 is composed of the crystal (H_C) and the radiation (H_R) Hamiltonians. The perturbation Halmitonian H_1 contains the electron-radiation H_{e-r} and the electron-phonon H_{e-ph} Halmitonians.

A simplified representation of the states is shown in the diagram of Figure 18 and can be written as:

$$\begin{aligned} |i\rangle &= |n_I, n_S, n_{ph}, \psi^0\rangle \quad , \\ |a\rangle &= |n_I - 1, n_S, n_{ph}, \psi^A\rangle \quad , \\ |b\rangle &= |n_I - 1, n_S, n_{ph} \pm 1, \psi^B\rangle \quad , \\ |f\rangle &= |n_I - 1, n_S + 1, n_{ph} \pm 1, \psi^0\rangle \quad , \end{aligned} \tag{3.2}$$

where the ket $|n_I, n_S, n_{ph}, \psi^e\rangle$ represents the number of incident photons n_I, number of scattered photons n_s, the number of the phonons n_{ph}, and the electronic state ψ^e, respectively. The signs of the phonon terms refer to the Stokes (+) and anti-Stokes (-) processes. The transition rate is given by:

$$W = \frac{2\pi}{\hbar} \sum_f \left| \sum_{a,b} \frac{\langle f|H|b\rangle \langle b|H|a\rangle \langle a|H|i\rangle}{(E_i - E_a)(E_i - E_b)} \right|^2 \delta(E_f - E_i) \quad . \tag{3.3}$$

The energies of each state are given by the following expressions:

$$\begin{aligned} E_i &= n_I\hbar\omega_I + n_S\hbar\omega_S + n_{ph}\hbar\omega_{ph} + E_0 \quad , \\ E_a &= n_I - 1\hbar\omega_I + n_S\hbar\omega_S + n_{ph}\hbar\omega_{ph} + E_A \quad , \\ E_b &= (n_I - 1)\hbar\omega_I + n_S\hbar\omega_S + (n_{ph} \pm 1)\hbar\omega_{ph} + E_B \quad , \\ E_f &= (n_I - 1)\hbar\omega_I + (n_S + 1)\hbar\omega_S + (n_{ph} \pm 1)\hbar\omega_{ph} + E_0 \quad , \end{aligned} \tag{3.4}$$

Adding the damping constant Γ related to the finite lifetime of the states, the intensity of Stokes process can be obtained using the following equation:

$$I = A \left| \sum_{a,b} \frac{\langle f|H_{e-r}|b\rangle \langle b|H_{e-ph}|a\rangle \langle a|H_{e-r}|i\rangle}{[\hbar\omega_I - (E_A - E_0) - i\Gamma_A][\hbar\omega_I - \omega_{ph} - (E_B - E_0) - i\Gamma_B]} \right|^2 \quad , \tag{3.5}$$

where Γ_j is the damping constant associated with the j-th energy level. This equation will be used to fit our results in this thesis.

When the denominator's real of one element of the equation 3.5 becomes a minimum, a resonance condition occurs, and the Raman signal is given rise to the so-called resonance Raman effect. In practical terms, the first term represents the resonance with the incident photon and the second one with the scattered photon.

Apart from energy conservation mentioned before, the momentum conservation also holds for the Raman effect:

$$\hbar\vec{k}_I = \hbar\vec{k}_S \pm \hbar\vec{q}_{ph} \quad , \tag{3.6}$$

where k is the momentum of the excitation. The momentum of the light is very small compared with the size of the Brillouin zone in crystals, first order Raman effect can only probe phonons near to the center of the Brillouin zone, and therefore the momentum of the phonon is close to zero, $\vec{q_k} \approx 0$. In higher order processes it is possible to rewrite this phonon restriction as $|\sum_i \vec{q_i}| \approx 0$ where q_i can come from any momentum source like a phonon or defect. So the momentum conservation plays a major role in understanding the defect-like processes like a moiré assisted Raman scattering.

Additionally, the symmetry selection rules can prevent some processes from being observed. In the study of vibrational spectra of materials, Raman and infrared spectra can be very different, since these process present different symmetry selection rules. In many systems some vibration modes are silent, and cannot be observed with optical techniques. In a group theory language, a Raman process can occur when:

$$\Gamma_{absorption} \otimes \Gamma_{e-ph} \otimes \Gamma_{emission} = \Gamma_1 \quad , \tag{3.7}$$

where $\Gamma_{emission}$, Γ_{e-ph} and $\Gamma_{absorption}$ correspond to the irreducible representation of the three matrix elements in the numerator of equation 3.5, respectively. Γ_1 is the totally symmetric representation. In the electric dipole approximation and linear polarized light, the absorption and emission basis functions are given by x, y, z, that corresponds to the polarization of light. The electron-phonon term belongs to the same irreducible representation as the associated vibration.(MALARD et al., 2009; NETO; GUINEA, 2007)

3.3 Experimental Details

Two different spectrometers were used to obtain the Raman spectra: a Jobin-Yvon Dilor XY (left) and a Witec Alpha 300R(right), shown in Figure 19. The Dilor XY system is a versatile instrument that can operate in a micro- and macro-Raman as well as both in a single- and triple-monochromator. All our measurements were obtained in the micro-Raman triple-monochromator configuration. In the micro setup, a confocal microscope was used as a spatial filter to detect only the signal from the focus region. An Ar/Kr laser

was used to excite the samples with 11 laser lines in range 1.9 to 2.7 eV. A nitrogen cooled CCD was used as detector.

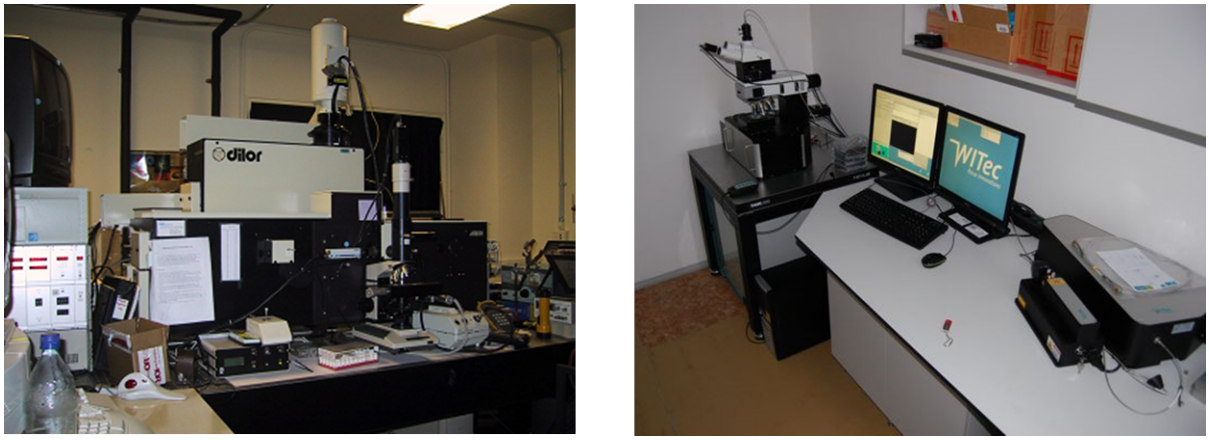

Figure 19 – Raman spectrometers used in this work, Dilor XY (left) and Witec Alpha 300R (right)

Witec Alpha 300 R system is a modern single-monochromator with confocal micro-Raman. To avoid light losses, the signal is transmited through an optical fiber from the laser to the microscope, and from the microscope to the monochromator. High quality filters are used to separate the laser from Raman signal. This equipment is two orders of magnitude more sensitive than Dilor XY, but unfortunately, our equipment has only 3 laser lines available.

4 Raman spectroscopy in Twisted Bilayer Graphene

We begin this chapter with a short discussion about Raman spectroscopy in graphene as a characterization tool, discussing the important features of its Raman spectrum. Also, we present the dependence of the spectra on the number of layers. Then, we focus on the results in TBG, discussing some works that are important in understanding the work done in this thesis. Finally, we discuss our samples and protocols.

4.1 Raman in Graphene

The first experimental result of Raman spectroscopy in graphene was reported by Ferrari *et al.* (FERRARI et al., 2006). They presented the Raman spectra of SLG and few layers graphene. After this work, Raman spectroscopy played a major role for the study of graphene and related systems (MALARD et al., 2009).

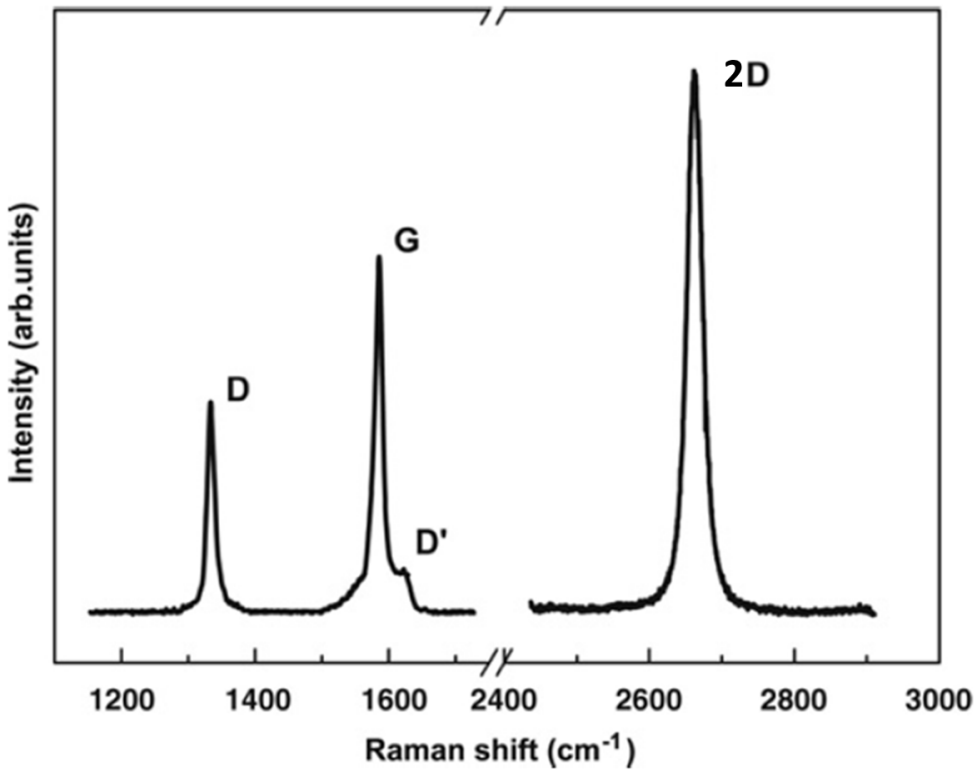

Figure 20 – Raman spectrum of graphene edge presenting the main bands: D, G, D', 2D.(MALARD et al., 2009)

In a high quality graphene sample only two bands can be observed, the G band($\sim 1585cm^{-1}$) and the 2D band($\sim 2700cm^{-1}$), see Figure 20. The G band is originated from the degenerated phonons iTO and iLO at the center of the Brillouin zone (Γ point) and corresponds to the vibration of the sublattice 1 against the sublattice 2. The G band is the only first order band in the graphene Raman spectrum.

The 2D band is a second order band that involves two iTO phonons near the K point in an intervalley double resonance Raman(DRR) process. One of those phonons carry the excitation to a state near to K' point and the other one brings the electron back to near the initial excited state and conserves momentum. Hence, it has twice the energy of the iTO phonon near to the K point of graphene.

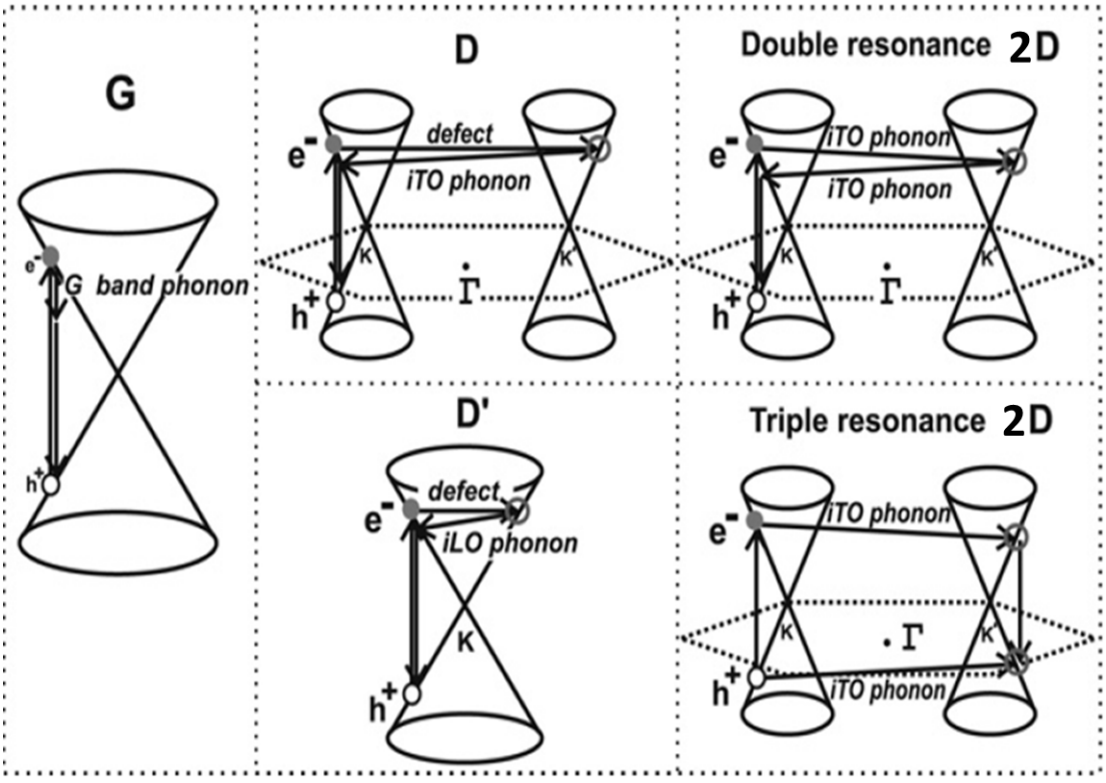

Figure 21 – Raman process diagrams in graphene of the bands: G, D, D' and 2D. The last one showing two processes. In the top a double resonance process and in the bottom a triple resonance presented by Venezuela *et al.*(VENEZUELA; LAZZERI; MAURI, 2011). D band and 2D involves iTO phonons going between two nonequivalent K points in Brillouin zone K and K'. (MALARD et al., 2009)

It is not rare to observe the presence of the other two peaks (D and D‘), shown in Figure 20. These peaks are generally associated with defects in the sample, that are responsible to the momentum conservation in the Raman process.

Differently from the 2D band that is originated by two iTO phonons, the D band($\sim 1350cm^{-1}$) is originated by a defect and one iTO phonon, and therefore the 2D

band is the second order of the D band. On the other hand, D' band($\sim 1620 cm^{-1}$) is originated by one iLO phonon, in an intravalley DRR process.

Figure 21 presents the diagram of those processes. Note that a triple resonance model of the 2D band is presented as discussed by Venezuela *et. al.*(VENEZUELA; LAZZERI; MAURI, 2011). These authors conclude that this process is the most significant for the origin of 2D-band.

Ferrari *et al.* showed that Raman spectroscopy can distinguish the number of layers in a few layer graphene sample in the Bernal stacking from the shape of 2D band, as presented in Figure 22 (FERRARI et al., 2006).

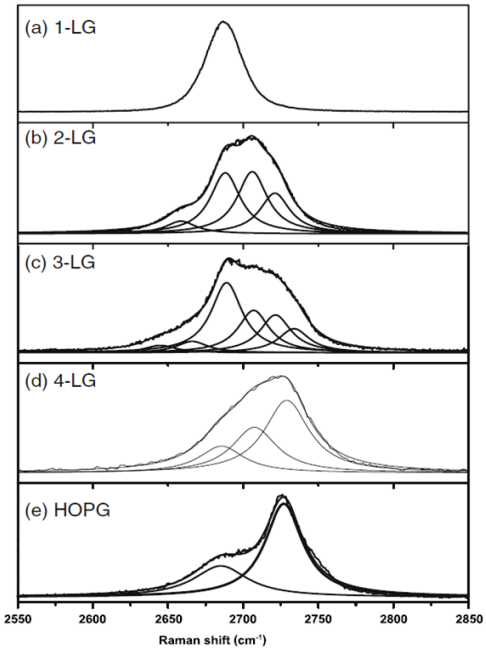

Figure 22 – 2D-band dependence with number of graphene layers in Bernal stacking configuration, for the number of layers varying from 1 to 4 and a bulk(MALARD et al., 2009)

Other works on multilayer graphene show a dependence of the 2D band with the graphene stacking. In the special trilayer case, the deconvolution of the 2D is different for the ABA and ABC stacking configurations(CONG et al., 2011).

4.2 Twisted Bilayer Graphene

In this section, we make a review of important works on Raman spectroscopy in TBGs.

Ni *et al.* reported the production of TBG via mechanical exfoliation, which were folded by smoothly flushing deionized water across the surface of the substrate containing single layer graphene(NI et al., 2009). They reported a huge enhancement in the G-band

in 2 different regions of a sample, X(13°) and Y(7.5°), as shown in Figure 23. In Figures 23 (c) and (d), an intensity switching between regions X and Y is observed when the excitation energy changes. Figures 23 (e) and (f) show the Raman spectra for regions X and Y, respectively. These spectra suggest a dependence of the resonance on the twisting angle. In Figure 23 (f), the 2D/G intensity ratio is different for excitation above and below the resonance energy, and 2D band shape is different from the AB stacked bilayer.

According to Ni *et al.*, this effect was interpreted as a transition between π levels mediated by the G-band phonon, in the double resonance Raman process presented in Figure 23 (g).

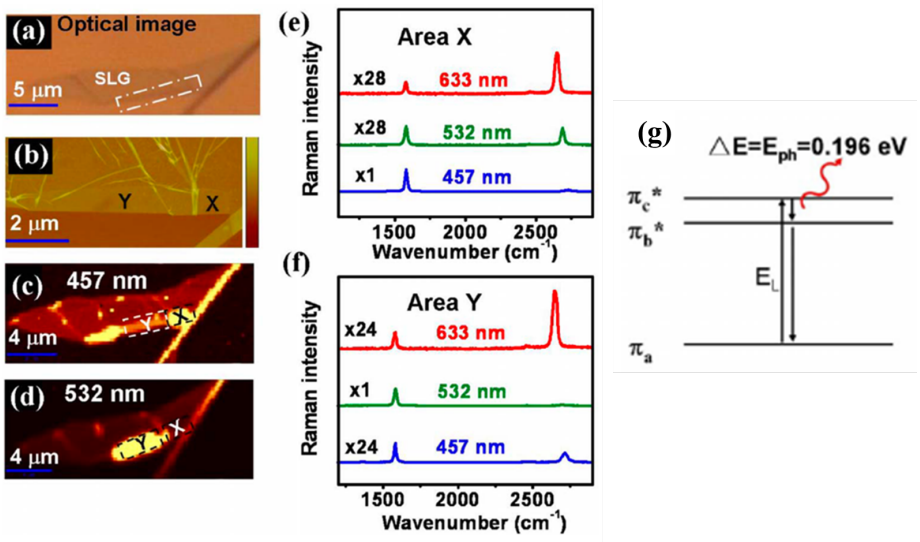

Figure 23 – (a) Optical image of a single-layer graphene containing some folded regions. (b) AFM image of the sample shown in (a). Raman imaging of the G band intensity of the graphene sample excited by 457 nm and 532 nm lasers lines, respectively. (e) and (f) Raman spectra of folded graphene, when excited by 457, 532, and 633 nm laser line, from area X and Y, respectively. (g) Simplified diagram of the double resonance Raman process(NI et al., 2009)

In 2012, a Raman study using three excitation energies and many CVD grown TGB domains with different twisting angle (over 50) was reported by Havener *et al.* (HAVENER et al., 2012). Besides Raman spectroscopy, dark field- transmision electronic microscopy (DF-TEM) was used to obtain the twisting angles. Their samples were transferred to a few nm silicon nitride membranes, which are compatible with both techniques.

Figure 24 summarizes the experimental results. In part (a) the angle-dependence of the G band intensity is presented, showing that the G band exhibits a huge enhancement for a narrow angle range of 2°around $\theta = 12.5$. Figure 24(b) shows experimental DF-TEM results. in the middle of the image we can observe a multilayer graphene region, and around it there are TBG domains, where the numbers represent the mis-orientation angle between graphene layers. Figure 24 (c) and (d) show the Raman maps of G and 2D bands,

respectively. The G band maps show a huge contrast generated by resonance in one domain. On the other hand, 2D band contrast is much smaller, but some angle-dependence of its intensity is observed. In Figure 24 (e), the Raman spectra show that higher twisting angle samples present more intense 2D bands.

Havener *et al*(HAVENER et al., 2012) also reported a simplified model that explains this enhancement. It comes from interlayer transition between valence band of one layer and the conduction band of the other. Because graphene dispersion of those bands are parallel, in the linear region, the Raman process originated from these parallel band transitions add coherently for the total resonance Raman intensity.

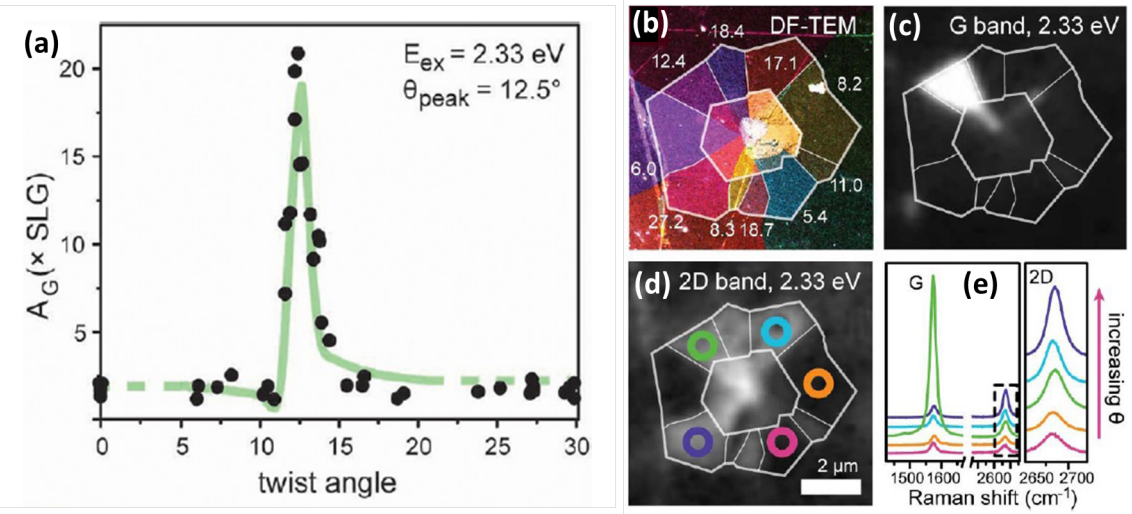

Figure 24 – (a) G-band enhancement versus twisted angle for a large number of samples for a 2,33 eV excitation energy. (b),(c),(d) are DF-TEM, G band map and 2D band, respectively of the same region. (e) Raman spectra of selected domains of (d) (HAVENER et al., 2012)

In a pioneer Raman study of graphene folded on itself, Gupta *et al.* reported the observation of a non-dispersive D-like band, called "I band", where I stands for interlayer (GUPTA et al., 2010). Figure 25(a) shows that the I band presents different positions and intensities for different samples when measured with the same excitation energy. Samples S1, S2 and S4 have better signal to noise ratio. In these samples, the new peak is narrower when compared to the regular D band ($I_{enveloped}$). Figure 25 (b), a multi-line Raman spectra of the same sample is presented. This figure suggests a resonance behavior of the non-dispersive I band, denoted as I_{fixed}. In addition, a new I band is reported for UV excitation (363 nm). It is important to mention that no G band enhancement was reported in their measurements.

An explanation for this peak was given as an umklapp double resonance intervalley process similar to D band in Figure 21, mediated via a Bragg scattering. However, they could not obtain a dependence of the peaks frequencies on the twisting angle, neither from

experiments nor from computational simulations.

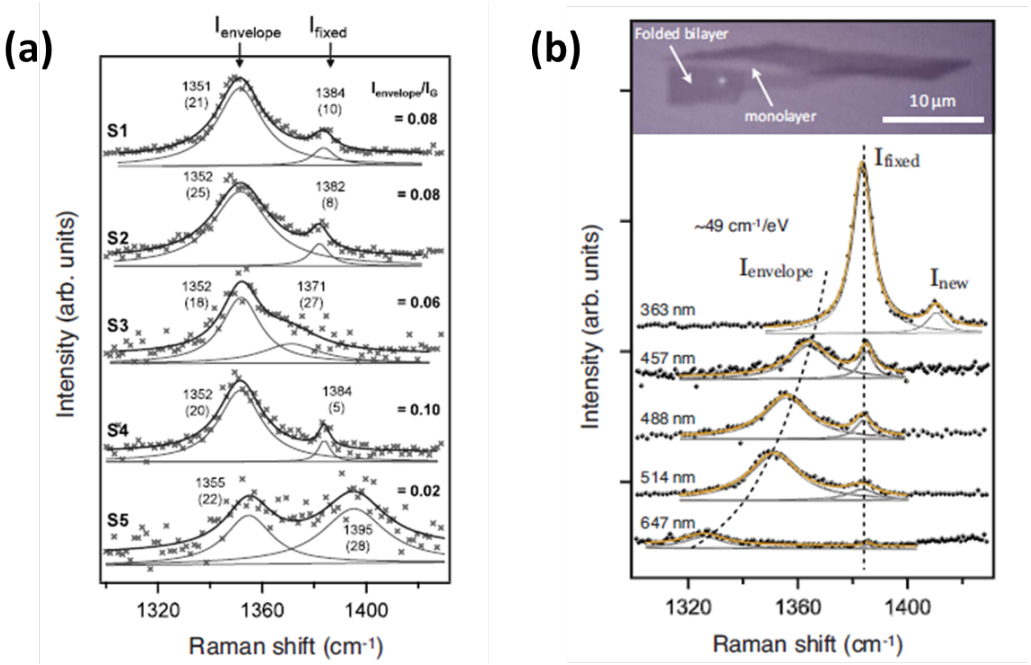

Figure 25 – (a) Raman spectra in the frequency range from 1300 to 1430 cm^1 for five different TBG samples, S1–S5. All spectra are collected using a 514 nm laser excitation at room temperature under ambient conditions. Peak positions and FWHM in parentheses are marked next to each Raman peak. The lower-frequency peak is called $I_{envelope}$(D-band) and the higher-frequency peak I_{fixed}. $I_{envelope}/I_G$ is shown to the right of each spectrum. (b) Top: optical image of TBG sample. Bottom: Raman spectra in the range from 1300 to 1430 cm^1 for excitation wavelengths of 363, 457, 488, 514, and 647 nm, showing the dispersion of $I_{envelope}$ and the unusual absence of dispersion for I_{fixed}. At the highest laser excitation energy, a new I-band peak emerges near 1410 cm^1. (GUPTA et al., 2010)

Using UV lasers, Righi *et al.* reported new families of Raman peaks in the range of 1000 to 1620 cm^{-1} in CVD graphene on the top of a copper substrate(RIGHI et al., 2011). In their results, the presence of one, two and sometimes three peaks was observed in the different domains. Also, the peaks positions changed from one domain to another, suggesting that they have different twisting angles, as shown in Figure 26(a). These peaks come from the iLA, iTO and iLO phonons. In Figure 26(b), the Raman spectra show a resonance behaviour in a domain with a single peak, similar to I_{fixed} in Gupta *et al.*(GUPTA et al., 2010). Notice that in Figure 26(a), these peaks are always much smaller than G band. On the other hand in the spectra obtained with the 3.40 eV line shown in Figure 26(b) the peak intensity has the same order of magnitude of the G band.

They explain the existence of the peaks by an umklapp double resonance Raman process presented in Figure 26(d). Note that q_{intra} and q_{inter} represent the Moiré wavevectors that satisfy the intravalley and intervalley double resonance processes, respectively. Figure

26(c) shows a TBG unit cell in real space used in calculations that show the presence of new peaks. However, these calculations were restricted to some commensurate angle cases, and no angle information was obtained from experimental data, preventing correlation between experimental and theoretical results.

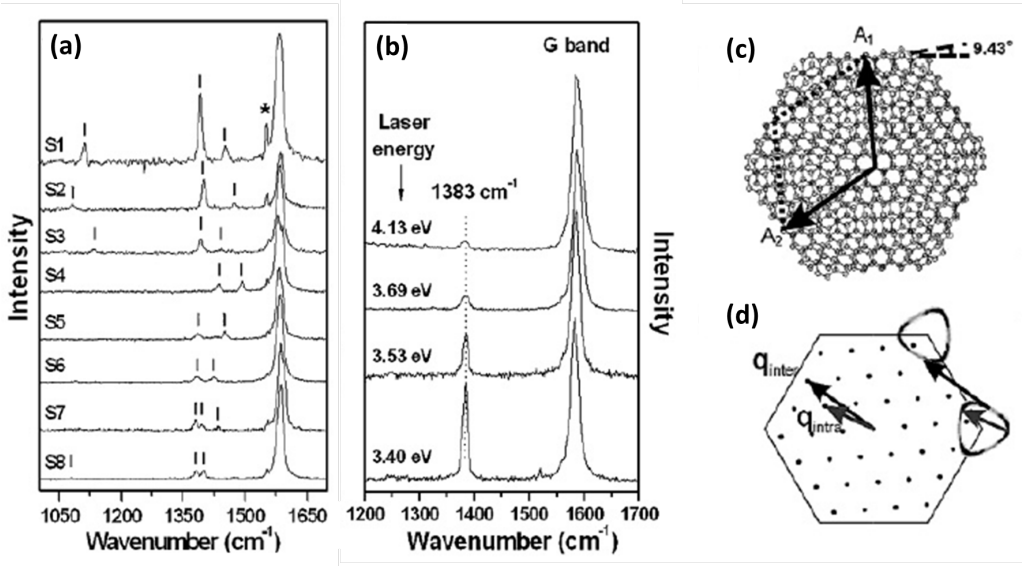

Figure 26 – ((a): Raman spectra in the frequency range from 1000 to 1700 cm^1 for different TBG domains, S1–S8. All spectra are collected using a 325 nm laser excitation. (b): Raman spectra in the range from 1200 to 1700 cm^1 for excitation energies of 3.40 eV (364.0 nm), 3.53 eV (351.1 nm), 3.69 eV (335.8 nm) and 4.13 eV (300.3 nm), showing the resonance behaviour of the non-dispersive 1383 cm^{-1} peak. (c): atomic configuration of a 9.43°TBG. (d): Wavevectors of the Moiré pattern superlattice and two possible double resonance Raman processes (intervalley and intravalley)(RIGHI et al., 2011).

Carozo *et. al.* reported a Raman study of TBG samples formed by folding graphene on itself, and observed two new bands called R($\sim 1480cm^{-1}$) and R'($\sim 1630cm^{-1}$)(CAROZO et al., 2011). These bands are explained considering the DRR processes of D and D' bands, related to TO and LO branches respectively. For those disorder-induced bands, momentum conservation for DRR process is provided by elastic scattering in defects, whereas for TBG, it is given by scattering in the moiré lattice. Figure 27 shows their calculation of the angle dependence of the phonon frequencies and the resonance energies of the intervalley and intravalley DRR processes. For the intravalley case, see Figure 27(a,b). A good agreement was found between the experimental data and calculations. On the other hand, for the intervalley process, see Figure 27(c,d). The expected resonance energy is more than 4 eV higher than the excitation energies used. The prediction of intravalley and intervalley resonance energies is larger than the M point band gap ($\approx 5.1eV$) shown in Figure 27(b) and (d) has no physical meaning.

Campos-Delgado *et al.* identified a large number of peaks that appear in a wide

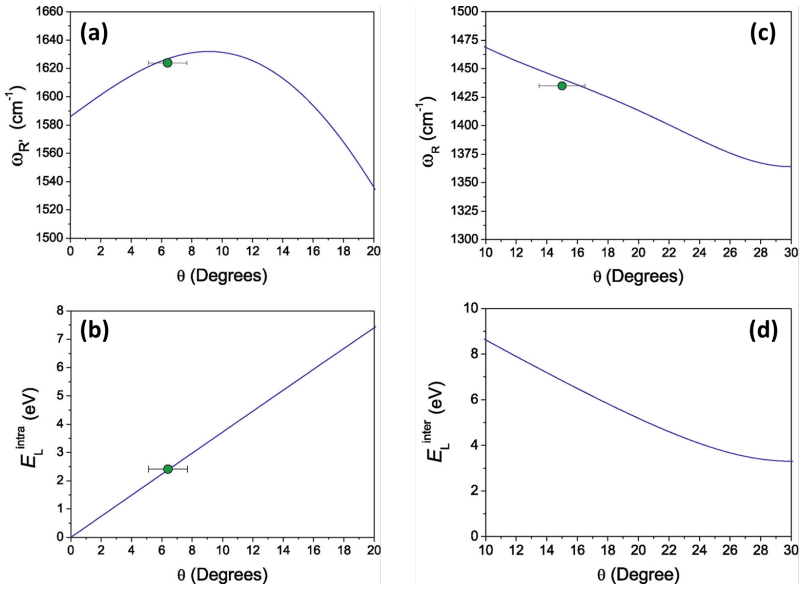

Figure 27 – (a) and (c) Phonon energy in function of the twisting angle for intravalley and intervalley processes, respectively. (b) and (d) Resonance excitation energy in function of the twisting angle for intravalley and intervalley processes, respectively. Green points are experimental data extracted from the most intense spectrum relative to that sample(CAROZO et al., 2011).

spectral range in spectra where the G band was also resonantly enhanced(CAMPOS-DELGADO et al., 2013). These peaks were associated with the graphene phonon branches considering an approximate expression relating the phonon wavevector and the twisting angle θ. They used the TO branch position along the ΓK to convert in q and θ, presented in Figure 28(a), and then used this calibration in (b) and (c) to extract the angle θ and moiré vector (q) dependence. The group of modes were mapped in the graphene phonon dispersion.

In 2013, two independents publications reported a correlation between the intensities of the so-called R-band and the G band (WANG et al., 2013; CAROZO et al., 2013). Wang *et al* reported a resonance Raman spectroscopy study in TBG grown by CVD technique. Each layer of those TBG samples present an hexagonal shapes. They obtain the twisting angles using TEM and STM, and conclude that the twisting angle can be obtained by the relative edge mis-orientation (WANG et al., 2013).

Wang *et al* present a resonance Raman data for twisting angles from 9°to nearly 30°using 6 laser lines from 1.94 eV to 3.4 eV. Figure 29(a) shows the results for high angle samples for a 364 nm excitation energy. The black line is a non-resonant sample ($\theta = 16°$). Note that all other sample spectra $\theta > 21°$ present a G band enhancement. Figure 29(b) shows a zoom in 2D band region. The intensity of the 16° sample is the smallest, other samples present almost the same 2D signal. The R band is shown in Figure 29(c), notice that its position changes from one sample to other.

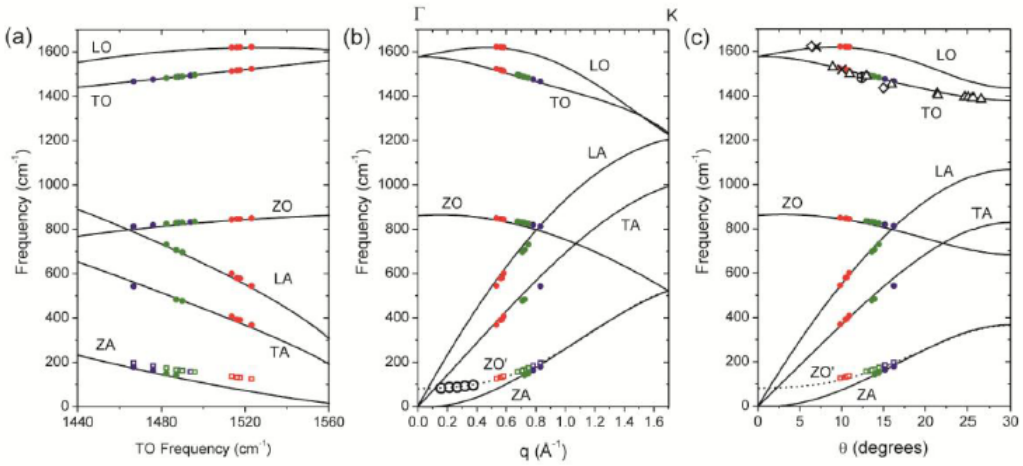

Figure 28 – Raman shifts for graphene phonon branches in function of (a) TO frequencies, (b) moiré reciprocal vector and (c) angle. E_L= 1.96(red), 2.41(green) and 2.54(blue) eV, other points are data from other works (CAMPOS-DELGADO et al., 2013).

According to Wang *et al*, the R band phonon frequencies can be estimated by zone folding the SLG's phonon dispersion in the TBG's reduced Brillouin zone. Figure 29(d) shows the R band position in function of the moiré reciprocal lattice vector(q) size, and the experimental data for R position with the sample angle.

In the other paper by Carozo *et al*(CAROZO et al., 2013), using similar samples as reported by same group in 2011(CAROZO et al., 2011), they reported that R band and G band have similar resonance profiles using 6 laser lines (1.96, 2.33, 2.41, 2.54, 2.71 and 3.81 eV), see Figure 30(a) and (b). Using equation 3.5 considering constant numerator, they obtain E_{vHs}= 2.68 and 2.79 eV, for samples with twisting angles of 12°and 13°, respectively. The broadening parameter ($\gamma = 0.12eV$) was obtained for the 13°G band profile, and considered for the other profiles due to the lack of experimental accuracy.

Another point is a theoretical model for the laser energy that the maximises enhancement factor in function of the angle θ, given by:

$$E_{vHS}(\theta) = E_0|\sin(3\theta)| \tag{4.1}$$

where $E_0 = 3.9eV$, provide the best fitting of the results. In this paper they also present a D-like band, a band that present width and dispersion as the D band, but it has a resonance behavior. A model considering delocalized defects plus the moiré wavevector can scatter the phonon and change the usual D band intensity dependence with laser energy ($I_D/I_G \ \alpha \ E_L^{-4}$) (CANcADO et al., 2006).

Kim *et al.* presented a systematic study of the 2D band in TBGs, and showed a clear difference of the 2D band intensity in samples with lower or higher angles than the

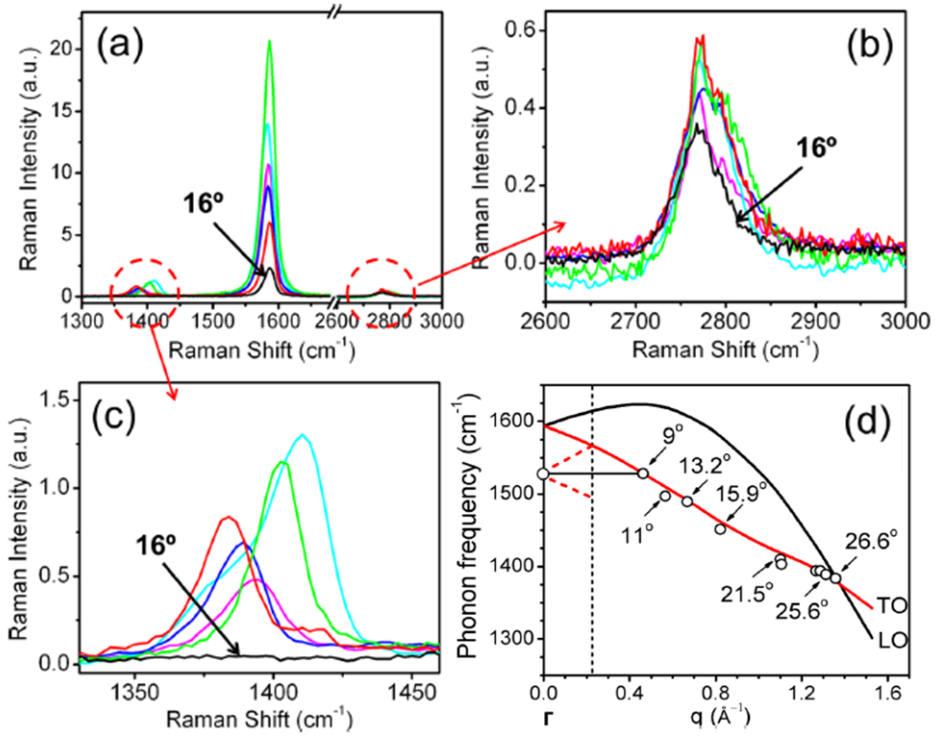

Figure 29 – (a)Raman spectra for high angle samples ($\theta > 16°$). (b) 2D band region of (a). (c) R band region of (a). (d) phonon frequency in function of moiré wavevector, circles represent experimental data, and numbers are the angles relative to these data points (WANG et al., 2013).

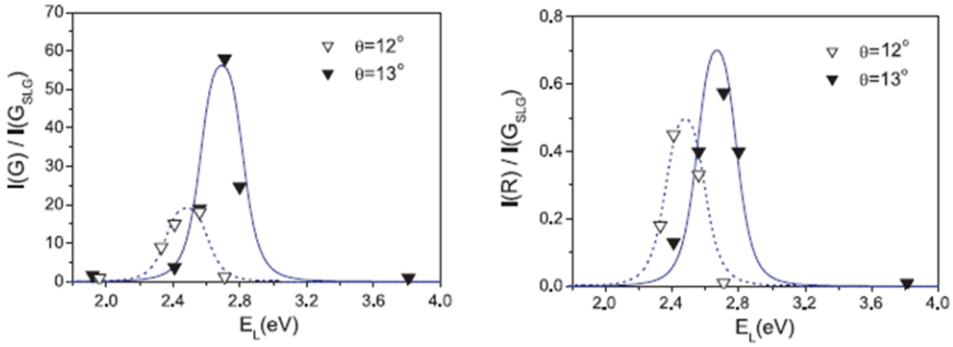

Figure 30 – (left) and (right) Raman resonance profile for 12(dashed) and 13°(solid) for G band and R band, respectively (CAROZO et al., 2013).

critical angle (KIM et al., 2012). Figure 31 shows the dependence of the 2D band on the twisted angle for a laser excitation of 1,96 eV. For this energy the critical angle is around 10°. Figure 31(a) shows the Raman spectra of 2D peaks in four TBG and SLG samples, and the strong dependence of the lineshape of the 2D band on the twisting angle. One can use three regions in this plot to analyze small, high and resonant angles, as shown in (b), (c) and (d).

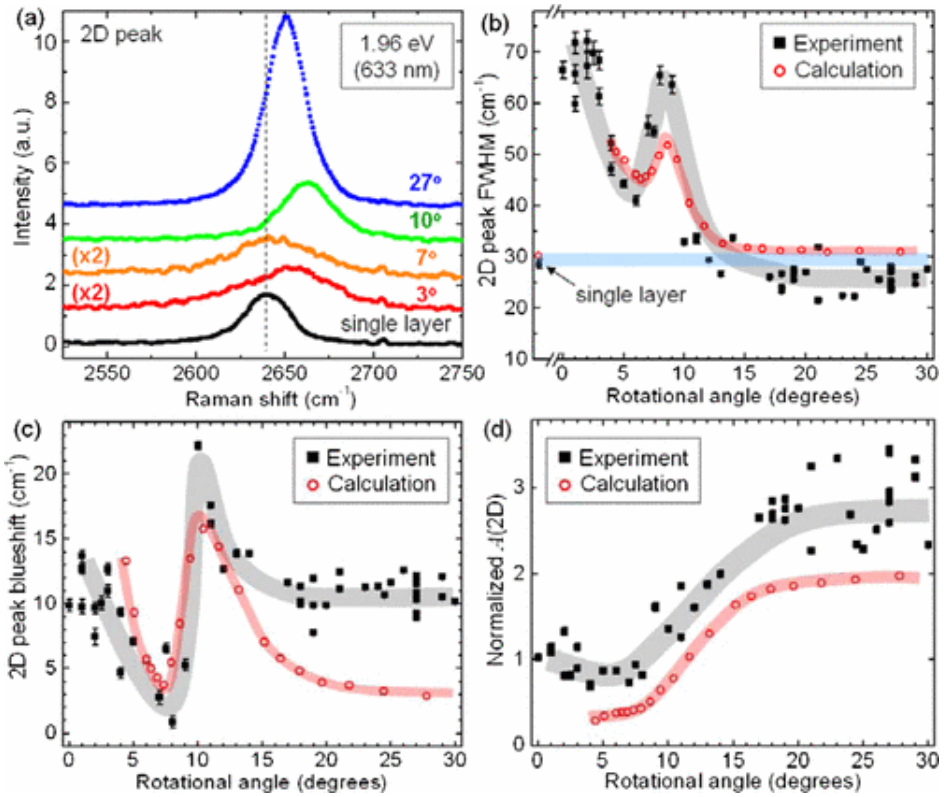

Figure 31 – Twisted angle dependence of Raman 2D peak: (a) Graphene 2D peak for some TBGs and SLG. The vertical dashed line represents the center of SLG. (b) TBG 2D band peak FWHM in function of twisting angle. (c) TBG 2D peak blue-shift in respective to the value from SLG. (d) Integral intensity of 2D peak normalized by SLG intensity. The black points are experimental data and the red points are calculations, the grey and red lines are only for guidance.(KIM et al., 2012)

For the 2D band width, shown in Figure 31(b), samples with small angle have a wider shape than large angle samples, and a peak shape with maximum close to θ_{crit} is observed in resonance. For position, shown in Figure 31(c), a blueshift is expected when compared to SLG for all twisting angles. For large angles, a constant shift of 10 cm^{-1} was obtained. On the other hand, small angles present a complicated behaviour, deceasing the position when angles go closer to the resonant region, which in turn presents another peak shape with maximum at θ_{crit}. The 2D intensity in Figure 31(d) shows the simplest curve, with intensities close to SLGs intensity for small angles, and a bit more than twice SLGs intensity for large angles. For the angle range close to θ_{crit}, There is a smooth increase of

the intensity as a function of the angle θ.

When compared to SLG, those differences in behaviour between small and large angles suggests a strong and weak interaction between the layers in TBG, respectively. This result is quite interesting for a protocol for multi-line excitation measurements. You can effectively filter an assembly of samples with the lower and higher laser lines and create a group in the range of θ_{lower} to θ_{higher}, which are good candidates for REP experiments.

4.3 Sample and Experimental Protocols

In this section we will present our TBG graphene samples, and also the measurement protocols and quality control to select samples that were used to obtain the results presented in chapters 5, 6, and 7.

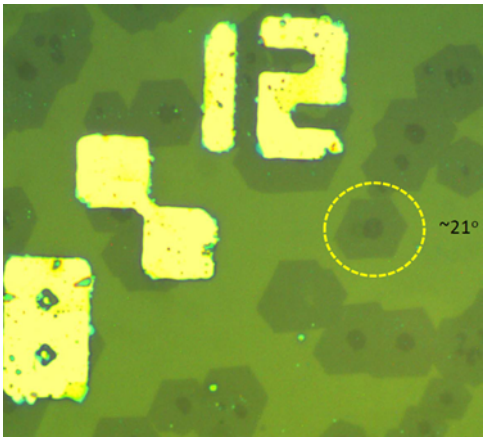

Figure 32 – Optical image of some TBG samples, the circle shows one sample that the angle was measured with the optical image.

Our CVD TBG samples were prepared by Chiuś group from Taiwan. The optical image of some of the structures is presented in Figure 32. The single layer region is measured about 10 μm and a bilayer region is of 2 μm. The sample preparation details can be found in the sample preparation work (LU et al., 2013). They study the dependence on temperature, H_2 pressure, CH_4 concentration and substrate (Cu) thickness in order to obtain a better quality CVD TBG sample. Figure 33 shows the effect of different parameters in the sample.

In one substrate there can be found thousands of samples with these features, but some samples can have a polycrystalline layer, like the one reported by Havener *et al.*(HAVENER et al., 2012). In our case, we prefer to focus only in samples which present a monocrystalline layers. To evaluate the quality of the sample, Raman maps of G, D and 2D bands of graphene have been obtained in those samples in a Witec Alpha 300R.

The diagram in the Figure 34 summarizes the core protocol of the work done in

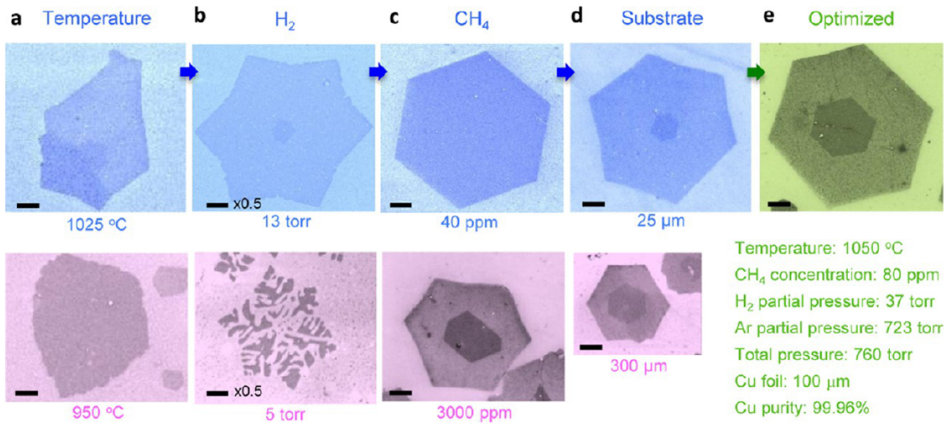

Figure 33 – SEM images showing the dependence of some growing parameters (a) Temperature; (b) H_2 partial pressure; (c) CH_4 concentration; (d) Cu thickness; (e) image of a sample with optimal parameters.(LU et al., 2013)

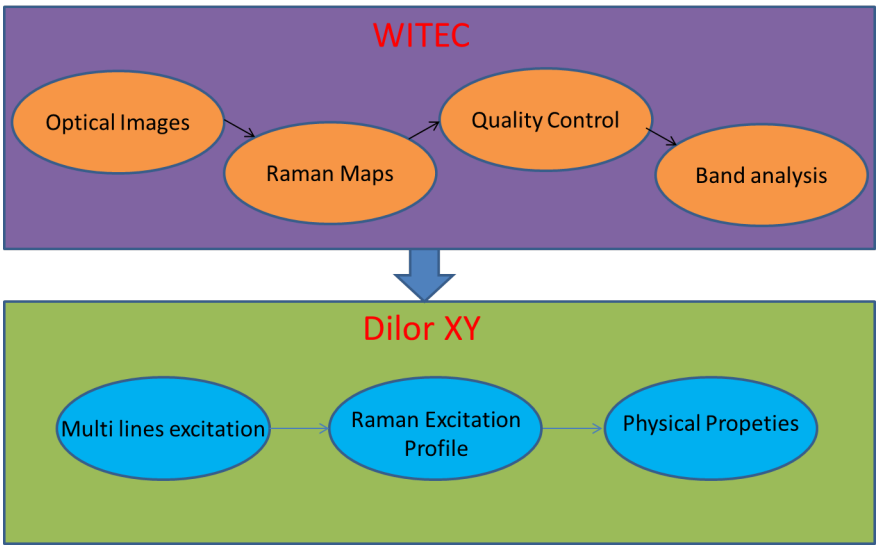

Figure 34 – Algorithm of the working method used in the experiments

this thesis. Witec system was used to obtain optical images and Raman maps, in order to control the quality and uniformity of the sample, verifying the correlation between optical image and Raman maps. In good and uniform samples, a single spectrum was acquired.

Samples previously selected in the Witec system were measured in the Dilor XY and, in this setup, a collection of spectra was obtained for each sample using different laser lines. The Raman excitation profile is obtained, then physical properties of the system could be extracted by analysing these profiles and be used to create a phenomenological model.

Figure 35 shows the G, D and 2D intensities, and 2D band width and the optical image in an arbitrary region of the sample. Using G band filter is easy to differentiate the SLG from BLG. Also we can see some ripples that might have been originated during the

transference process.

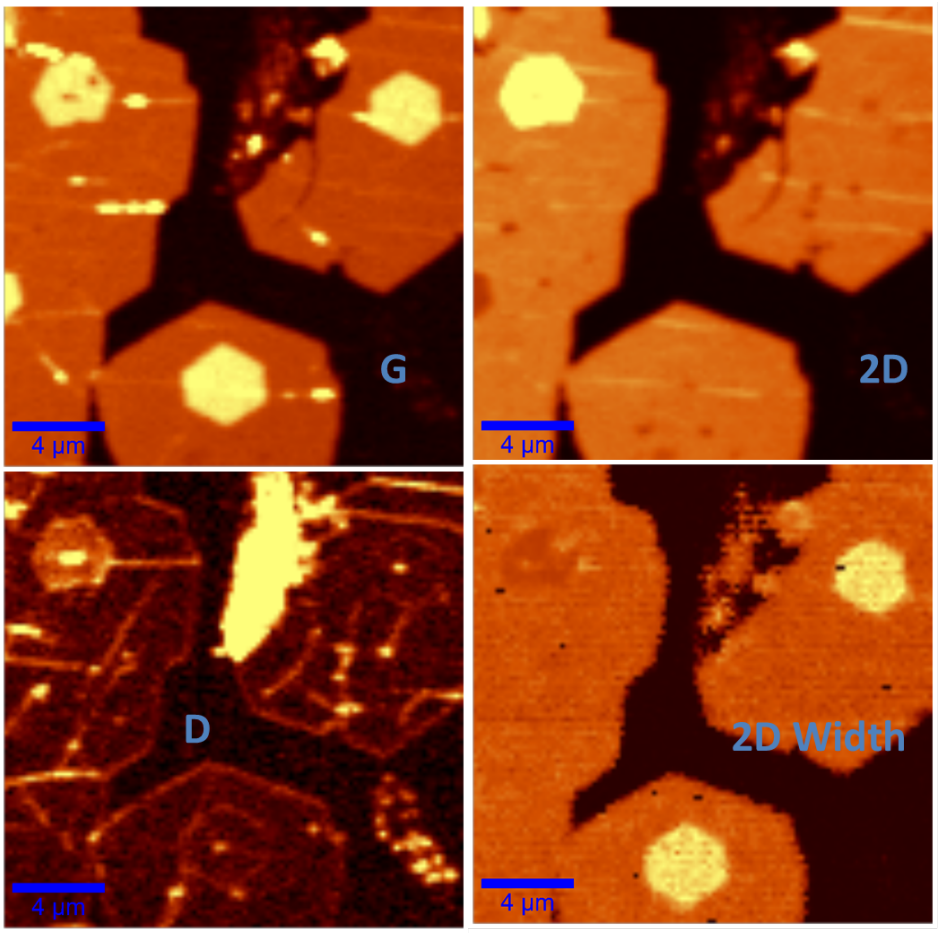

Figure 35 – Raman images of the G(top-left), D(bottom-left) and 2D (top-right) bands, also 2D-band width (bottom-right) for a region of one of our samples. The excitation wavelength is 488 nm.

The D band image helps in the ripples visualisation and also in some grains contours. The grain contour information is important to evaluate the orientation of the graphene samples, because those contours present a small D band, they are in the zigzag orientation (CANCADO et al., 2004). Also monocrystalline hexagonal graphene flakes have a zigzag edge, because the armchair orientation grows faster than the zigzag orientation (LU et al., 2013; WANG et al., 2013). This information is important to evaluate the angle between the layers with the optical image (WANG et al., 2013), this strategy have been used to measure the angle.

The 2D filters shows us that there is a high intensity 2D in one of the bilayer regions, but not so high intenity in the other two. However, as discussed in Figure 31, the 2D width shows a huge difference between those two and the intense TBG. The width of the low intensity ones are considerably bigger than the intense TBG, so the two low intensity peaks are associated to small angle samples and the high intensity one is associated to a high angle sample. This process helps us to discriminate flakes that present a policrystalline

formation. Usually when this happens the angle obtained via optical image measurement does not match with the Raman spectra.

A large number of samples were imaged. In some samples the resonance condition is matched and the G band gets enhanced as shown in Figure 36. Despite this sample being in resonance condition, we can clearly see a black spot in the G band Raman map and a bright spot in the D band Raman map, in which this is generated by a dirt point in the top of the bilayer region, so this sample is reproved in the quality control.

In chapter 5 we report the results of the G band dependence with the angle for those samples mapped in the Witec system.

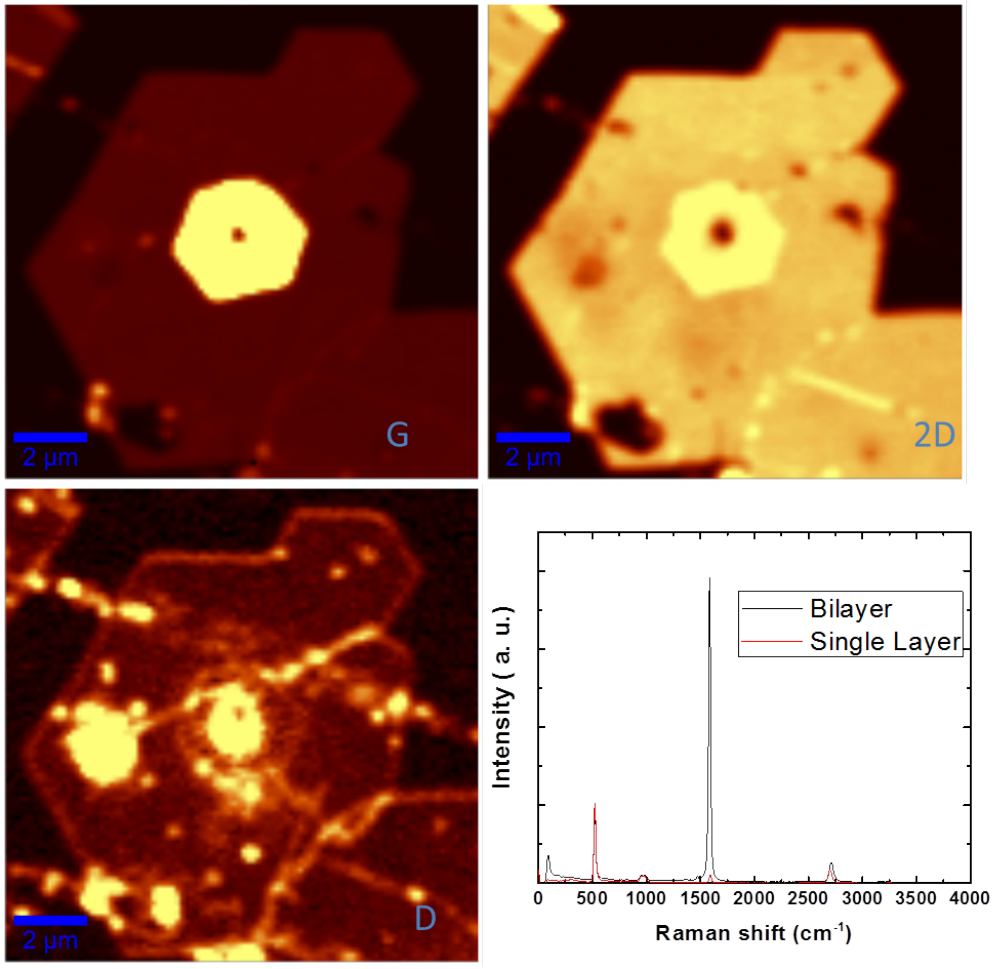

Figure 36 – Raman images of: G(top-left), D(bottom-left) and 2D (top-right) bands, (bottom-right) spectrum of the TBG resonant area (black) and for SLG (red) for an excitation energy of 2.54 eV. In this case the enhancement is more than 60 times. The G band image is saturated for better visualization of the SLG

The next step was to obtain REP. For that we selected the good quality samples in the angle range of 10° to 17° as candidates to REP measurements in Dilor XY. This angle range was selected due to our laser range, from 647 nm to 457 nm, which we can excite in the energy difference between the van Hove singularities. The results of the analysis of the

G band's REP in those samples were reported in chapter 6.

The last step is to study the mechanisms that originated those new peaks, for that we measured those TBG samples in the visible, infrared and ultraviolet ranges. To explain those effects we developed two different models: the intralayer and the interlayer. In few words, the interlayer process depends of the electronic structure of both graphene layers, on the other hand, the intralayer is a model with one graphene layer and a periodic potential. To prove our idea, we did measurements in Graphene/h-BH heterostructures and we could see the intralayer signature. This work is explained in details in chapter 7.

In order to sintetize all the measurements, Table 4.3 shows all the equipment and laser lines and samples used in this thesis.

Equipament	Excitation lasers	Substrate	Laboratory
WITEC 1	488, 532, 633	300 nm SiO_2/Si 90 nm SiO_2/Si Fused silica	Mackgraphe –Mackenzie- SP
Dilor XY	457, 461, 472, 488, 496, 501, 514, 520, 530, 568, 647	300 nm SiO_2/Si	Raman Spectroscopy Laboratory – UFMG
Dilor XY T64000	351, 364, 400	90 nm SiO_2/Si	CEMES/CNRS - Toullouse - FR
Handmade Setup	680,730,830	Fused Silica	Charles Columb Laboratory - Montpellier - FR
WITEC 2	457,532,633	Graphene/h-BN 300 nm SiO_2/Si	CT Nanotubos Physics Departament of UFMG

Table 1 – Equipments, Laser lines, samples substracts and laboratories where we obtained the data for this thesis.

5 The enhancement of the G band in TBG: commensurate superlattice versus moiré quasi-periodic pattern resonances.

The first goal of this PhD thesis was to check the theoretical predictions by Sato et al (SATO et al., 2012) shown in Fig. 12(b). According to this work, resonances should be dependent on the integer numbers, n and m, used to describe the supercell of a commensurate TBGs, and grouped in familes of curves for each m - n equal to a constant. Previous Raman studies in the visible range have reported the enhancement of the G band only in samples with intermediate values of θ (12-16^circ). In principle, as suggested by Sato et al (SATO et al., 2012), the enhancement of the G band could also be observed for samples with small and large values of θ for families of TBGs where m - $n > 1$. This work was done in collaboration with H. B. Ribeiro, from Mackenzie University, Sao Paulo, and results were published in the article "Origin of van Hove singularities in twisted bilayer graphene", by H.B. Ribeiro, K. Sato, G.S.N. Eliel, E.A.T. de Souza, Chun-Chieh Lu, Po-Wen Chiu, R. Saito, M.A. Pimenta, that was published in Carbon vol. 90, 138-145 (2015). The chapter below is based on parts of the article related to the verification of the predictions shown in Fig. 12(b)

Abstract

In this work, we present a resonance Raman spectroscopy study of more than 100 samples of twisted bilayer graphene (TBG) with a continuous distribution of twisting angles from 0 to 30°, using three different laser excitation energies (1.96, 2.33 and 2.54 eV). From the Raman images of all investigated samples we could observe huge enhancements of the G band for samples with twisting angles between 9° and 17°, in agreement with previous Raman studies of TBGs. Although we investigated a large number of samples with low (< 9°) or high (>17°) twisting angles, we could not observe the G-band enhancement that was predicted for these samples from the zone-folding of the single layer graphene electronic structure. Our results allow us to conclude that the van Hove singularities in the density of states are associated with the moiré pattern, which does not necessarily exhibit a translational symmetry.

5.1 Introduction

Twisted bilayer graphene (TBG) is a bilayer graphene sample where the two constitutive layers are rotated by the twisting angle θ_{TW} with respect to each other. For some specific twisting angles θ_{TW}, we can have a commensurate superlattice, and the superlattice unit cell size T_{TW} is denoted by two integers (n, m) (SATO et al., 2012). However, for a general twisting angles, a quasi-periodic structure called moiré pattern can also be observed. The size T_M of the moiré unit cell is not always the same as the superlattice unit cell T_{TW}, and depends only on the twisting angle θ_{TW} (MOON; KOSHINO, 2012).

The electronic energy band structure of TBG shows the presence of van Hove singularities (vHs), that could, in principle, be ascribed to both the commensurate unit cell and the quasi-periodic moiré pattern (SATO et al., 2012; MOON; KOSHINO, 2012; NI et al., 2008; SHALLCROSS et al., 2010; LAISSARDIÈRE; MAYOU; MAGAUD, 2010; MORELL et al., 2010). For the commensurate case, the vHs can be described by zone-folding of the energy band of single layer graphene (SLG), since the energy dispersion becomes flat at the folded zone boundary (SATO et al., 2012). The vHs associated with the moiré pattern can be understood considering the extended Brillouin zone; here, the energy dispersion flat regions appear at the crossing point between the two Dirac cones of the bottom and top layers (SANTOS; PERES; NETO, 2007)

Resonance Raman spectroscopy has shown to be very useful in studying van Hove singularities (vHs) in the DOS of carbon nanotubes (CNT) (SAITO; FANTINI; JIANG, 2008), since the Raman signal is strongly enhanced when both the incident and scattered photons are in resonance with transitions between vHs in the valence and conduction bands (PIMENTA et al., 1998; FANTINI et al., 2004; MOURA et al., 2014; VENEZUELA; LAZZERI; MAURI, 2011). Considering the vHs associated with the commensurate unit cell of TBGs, Sato et al. (SATO et al., 2012) calculated their separation energies, which are denoted by E_{ii}, and showed that they were expected to depend on the (n, m) indices for a commensurate TBG. A plot of E_{ii} was presented in the work as a function of the length of the unit cell T_{TW}, specified by (n, m), which is similar to the Kataura plot for the case of single wall carbon nanotubes (SAITO; DRESSELHAUS; DRESSELHAUS, 2000; SAMSONIDZE et al., 2004; NUGRAHA et al., 2010; KATAURA et al., 1999). Recently Ni *et al* (NI et al., 2009) and Havener *et al* (HAVENER et al., 2012) have observed a very strong enhancement of the G band for a number TBG samples with different twisting angles, and showed that the resonances depend only on the twisting angle θ_{TW}.

In order to understand the origin of the van Hove singularities associated with both the commensurate superlattice unit cell T_{TW} or with the smaller quasi-periodic moiré unit cell T_M, we have performed Raman mapping experiments in more than 100 TBG samples with many different twisting angles between 0° and 30°, measured by direct inspection of

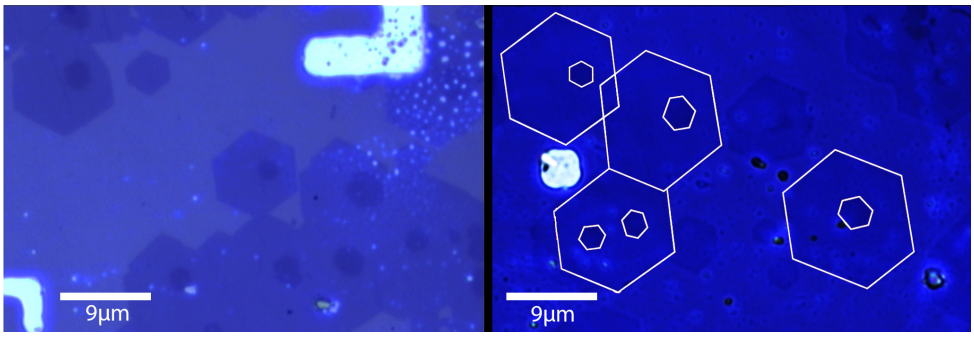

Figure 37 – (Color online) Optical microscopy image of the sample clearly showing different twisted bilayer graphene structures. The white hexagons on the right were made in order to determine the twisting angle between the the bottom and top graphene flakes.

the optical microscope images. We have observed that, using visible laser lines, the G band enhancement occurs only for intermediate twisting angles ($9° < \theta_{TW} < 17°$), in agreement with the previous conclusions by Ni *et al* (NI et al., 2009) and Havener *et al* (HAVENER et al., 2012). Moreover, we could also investigate the behavior of the Raman G band enhancement in non-resonant cases and we observed that the intensity ratio I_{TBG}/I_{SLG} is even smaller than twice of that for single-layer graphene, and that it depends on the laser energy.

Here, we present the results for the Raman G band intensity and linewidth for more than 100 TBG samples with different twisting angles in order to verify experimentally the existence of a Kataura-like plot for TBG.

5.2 Experimental details

Single-crystal TBG samples were grown by the atmospheric pressure CVD of methane (99.99 %) on polycrystalline Cu foils at 1050 °C. In the CVD growth method, methane (80 ppm) was mixed with the flows of 300 s.c.c.m. Ar and of 15 s.c.c.m. H_2 was fed into the reaction chamber for ∼7 min to form bilayer graphene. For graphene transfer, the Cu foil was coated with a thin layer of polycarbonate, followed by etching in HCl aqueous solution. The polycarbonate film, along with the attached graphene, was then transferred onto a Si:SiO_2 substrate with predefined marks. The polycarbonate film was then cleaned up using chloroform.

TBG samples consisting of a large number of islands at the same Cu substrate were obtained (LU et al., 2013). Figure 37 shows the optical microscopy image of the sample, where we can see that both the bottom and top layers exhibit hexagonal shapes. We can thus determine θ_{TW} as the smallest angle between two edges of the two hexagons. The accuracy for θ_{TW} measured by the optical microscope is ±1°. Further θ_{TW} can be

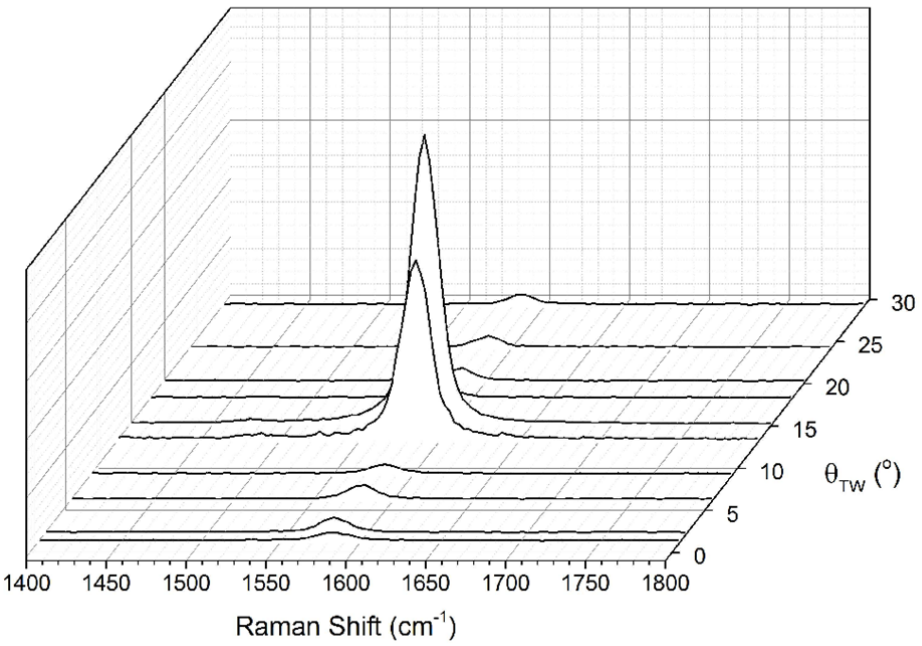

Figure 38 – G-band Raman spectra obtained with the 488 nm laser line for samples of twisted bilayer graphene with different twisting angles.

confirmed by the electron diffraction method, and it was observed that the edge is made of the so-called zigzag structure (KIM et al., 2012).

The micro Raman imaging experiments were obtained using a Witec Alpha 300 instrument, operating with three different laser lines, at 488, 532 and 633nm (2.54, 2.33 and 1.96 eV, respectively). Typical laser intensity and accumulation time are 10^7 W/m^2 and 1 min, respectively.

5.3 Results of Raman Experiments

Raman imaging of more than 100 samples of TBG with different twisting angles were performed, allowing us to make Raman mapping of the main features of the graphene for three different laser wavelengths 488, 532 and 633 nm (2.54, 2.33 and 1.96 eV laser energies, respectively). Raman spectra were obtained between 100 and 3500 cm^{-1}, including the most prominent features such as the G and 2D bands (MALARD et al., 2009), but we will focus only on the analysis of the G band as a function of the twisting angle and the laser energy.

Figure 38 shows the spectra of the G band, obtained with the 488 nm laser line, for samples of TBG with different twisting angles. Notice that the G band starts to be enhanced for twisting angles θ around 12°, reaches a maximum for $\theta = 15°$, and decreases

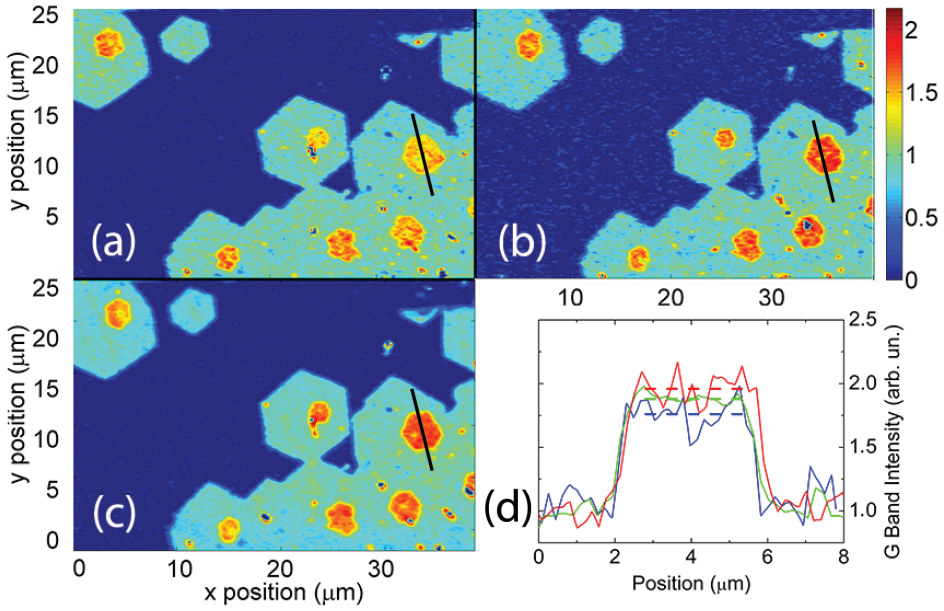

Figure 39 – (Color online) (a), (b) and (c) Raman mapping of a region containing different TBG structures, recorded with the (a) 633 nm, (b) 532 nm and (c) 488 nm laser lines, respectively. (d) Profile of G Band intensity along the lines indicated in (a), (b) and (c). Red, green, and blue lines correspond 633, 532, and 488 nm, respectively. The dashed line is the averaged value of G band intensity over the TBG region.

again with increasing twisting angles.

Figure 39 shows the Raman mapping in a region of the sample with a few TBG structures, where the color scale gives the intensity of the Raman G band. Notice that, as expected, the Raman G band is always more intense in the TBG regions compared with the single layer part. The G-band images obtained with the 488, 532 and 633nm laser lines are shown in Figures 39 (a), (b) and (c), respectively. Figure 39 (d) shows the profile of the G-band intensity along the line shown in Figures 39 (a), (b) and (c), that passes through the single layer and TBG parts of the sample. From profiles similar to those shown in Figure 39 (d), we could obtain experimentally the ratio I_{TBG}/I_{SLG} of the intensities of the G band in TBG with respect to the single layer graphene, for all the different samples investigated in this work.

Figure 40 shows the plot of I_{TBG}/I_{SLG} for all measured samples as a function of the twisting angle θ_{TW}, obtained with the three different laser energies. We observe that a huge enhancement of the TBG G-band occurs for samples with intermediate twisting angles ranging from 9° to 17°, reaching values up to more than 90 times the intensity of the single layer G band. This result agrees with the conclusions previously reported by Ni *et. al.* (NI et al., 2009) and Havener *et. al.*(HAVENER et al., 2012). However, we further observed that, for small ($\theta_{TW} < 9°$) and large ($\theta_{TW} > 17°$) twisting angles, the ratio I_{TBG}/I_{SLG} was always smaller than two, as shown in the insets of Figure 40. Interestingly,

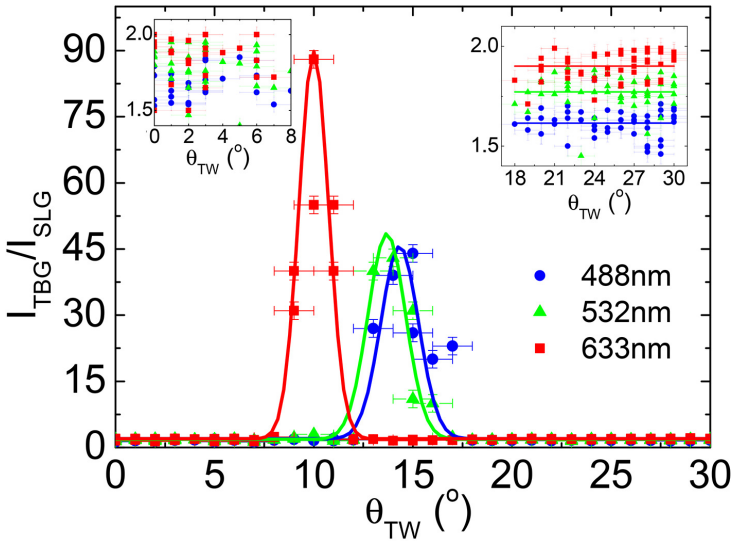

Figure 40 – (Color online) I_{TBG}/I_{SLG} for all 100 samples studied in this work with many different twisting angles between 0° and 30°. Blue, green, and red dots are data taken at 488, 532, 633 nm. Solid lines are the Gaussian fits to the observed angle dependence I_{TBG}/I_{SLG} The insets show a zoom of I_{TBG}/I_{SLG} for low ($< 9°$) and high twisting angles ($> 17°$).

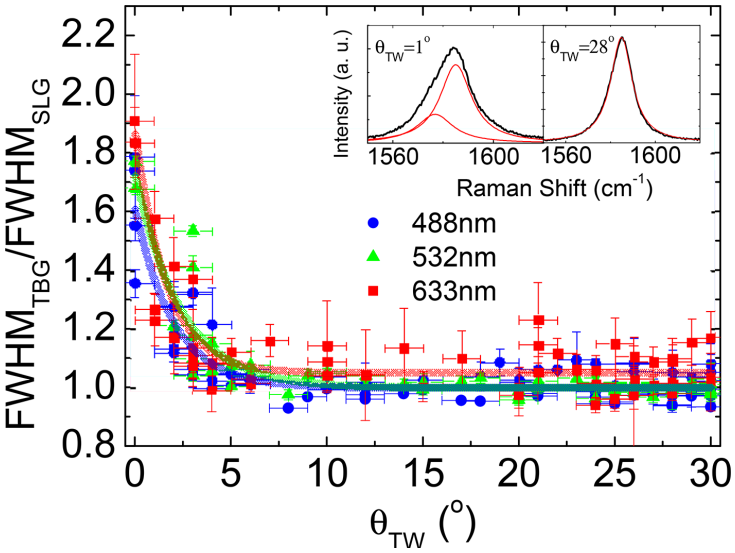

Figure 41 – (Color online) Angular dependence of the ratio between the FWHM of TBG and SLG. The insets show the fitting of the G Band with two and one Lorentzians for $\theta = 1°$ and $\theta = 28°$, respectively.

we observed that, even when we do not see the G-band strong enhancement, the ratio I_{TBG}/I_{SLG} always depends on the laser energy. This effect is particularly clear for high twisting angles ($\theta > 17°$), as shown in the inset of Figure 40, where the ratio I_{TBG}/I_{SLG} is observed to decrease with increasing laser energy.

We have also analyzed the G-band full-width at half maximum (FWHM) of all TBG samples and Figure 41 shows the angular dependence of the ratio between the FWHMs of

the TBG and SLG regions, for all investigated samples. We can see that this ratio is close to one for $\theta_{TW} > 7°$ but it increases with decreasing twisting angle in the low angle range. Insets in Figure 41 show the fitting of the TBG G-band for one sample with large twisting angle (28°) and other with small twisting angle (1°). We can see that the G band is well fitted by just one Lorentzian for large twisting angle, whereas, for low twisting angle, the G band is asymmetric and is fitted by two Lorentzian curves.

5.4 Discussion

We have observed in the experimental results in Figure 40 that, among more than 100 different samples of TBGs, we only could observe G-band enhancement for samples with intermediate angles $9° < \theta_{TW} < 17°$. The experimental results are compatible with the transitions between van Hove singularities originating from the quasi-periodic moiré patterns, but not from superlattice unit cell, since, in this second case, electronic transitions in the visible range would be expected for practically all the range of θ_{TW} from 0° to 30°(SATO et al., 2012).

An explanation for the observed experimental result is that the van Hove singularities associated with the superlattice structures are much weaker than the van Hove singularities originating from the moiré pattern. Although the moiré pattern is not strictly periodic, the local arrangement of atoms is very similar to each other. This similar pattern of the atoms can give a large singularity in the density of states even though they are not strictly periodic. A typical example of this special case is in quasicrystals, in which the lattice is not a periodic structure, but the quasicrystal electronic structure exhibits sharp peaks in the density of states because of self-similar structures.

Let us discuss now the reason why we get values of I_{TBG}/I_{SLG} smaller than 2 for large and small θ_{TW}, and why this value decreases with increasing laser energy, as shown in the inset of Figure 40. When the laser energy increases, the photo-excited carrier can relax by emitting many phonons, which are not relevant to the Raman process. If the relaxation process results in a large linewidth, we get relatively small Raman intensity because some specific Raman processes are suppressed. In the TBG, we have two energy dispersions at similar energy regions and, thus, we get more than two possible relaxation processes when compared to SLG graphene. Although we did not calculate the possible relaxation processes for photo excited carriers, this process can qualitatively explain the experimental results.

Finally, we briefly discuss the θ_{TW} dependence of FWHM of the G band which is shown in Figure 41. The reason why we get a large FWHM of the G band spectra for samples with small θ_{TW} is related to the fact that the G band phonon frequency might be modified by different local stacking arrangements. When θ_{TW} is small, we can clearly find

areas in the unit cell TBG which have either AA or AB stacking arrangements for the two graphene layers. Interlayer interactions for AA or AB stacking should give different phonon frequencies, increasing the total spectral width. Since the phonon mode can see only an averaged potential over the unit cell, especially for longer wavelength phonons, the difference of AA and AB stacking order would be smeared out for a small unit cell (or moiré cell). Therefore, when θ_{TW} is small, the size of the unit cell or moiré cell is sufficiently large, and thus different local phonon frequencies increase the G band FWHM. We expect that this effect should be larger when compared with the lower phonon branches, such as the oTO, because the phonon frequency is higher, and a small change of force constants gives a relatively larger effect to the phonon frequency. Another effect that needs to be considered is the Kohn anomaly effect of the G band phonon(SASAKI et al., 2009). G band phonon frequency is affected by the electronic states near the Fermi energy or the edge structures of a graphene nanoribbon. Thus, different local stacking arrangements might affect the frequency and FWHM of the Raman bands.

5.5 Conclusion

In conclusion, in this work we have investigated the Raman G band of more than 100 samples of TBG covering all values of twisting angle θ_{TW} between 0 and 30°, using three different laser energies. Among the TBG samples, only samples with θ_{TW} from 9 to 17° exhibit a strong enhancement of the Raman intensity, while, for no enhancement was observed for TBG samples with low and high twisting angles. This results allows us to understand the origin of the van Hove singularities contributing to the observed effects, which are associated with the smaller quasi-periodic moiré unit cell T_M, and not with the commensurate superlattice unit cell T_{TW}.

6 Raman excitation profile of the G-band enhancement in twisted bilayer graphene

The results presented in this chapter were published in the article "Raman excitation profile of the G-band enhancement in twisted bilayer graphene", by G.S.N. Eliel, H.B. Ribeiro, K. Sato, R. Saito, Chun-Chieh Lu, Po-Wen Chiu, C. Fantini, A. Righi, M.A. Pimenta, in Brazilian Journal of Physics (ELIEL et al., 2017)

Abstract

A resonant Raman study of twisted bilayer graphene (TBG) samples with different twisting angles using many different laser lines in the visible range is presented. The samples were fabricated by CVD technique and transferred to Si/SiO_2 substrates. The Raman excitation profiles of the huge enhancement of the G-band intensity for a group of different TBG flakes were obtained experimentally, and the analysis of the profiles using a theoretical expression for the Raman intensities allowed us to obtain the energies of the van Hove singularities generated by the moiré patterns and the lifetimes of the excited state of the Raman process. Our results exhibit a good agreement between experimental and calculated energies for van Hove singularities, and show that the lifetime of photoexcited carrier does not depend significantly on the twisting angle in the range intermediate angles (θ between 10° and 15°). We observed that the width of the resonance window ($\Gamma \approx 250$ meV) is much larger than the REP of the Raman modes of carbon nanotubes, which are also enhanced by resonances with van Hove singularities.

6.1 Introduction

After the discovery of graphene in 2004 (NOVOSELOV et al., 2004), many other layered two-dimensional materials have been studied both experimentally and theoretically. In present days, a considerable number of 2D structures with different band gaps, ranging from 0eV(graphene) to 4,7eV in h-BN(MIRO; AUDIFFRED; HEINE, 2014). The combination, like stacking, of those many materials can create electronic devices in a reduced size(GEIM; GRIGORIEVA, 2013).

Since the discovery of graphene in 2004 (NOVOSELOV et al., 2004), it was demonstrated both experimentally and theoretically that the behaviour of electrons in bilayer graphene is very different from monolayer graphene, and strongly dependent of the rotational twisting angle between the two layers. Twisted bilayer graphene (TBG) is

a bilayer graphene sample where the two constitutive layers are rotated by an arbitrary twisting angle θ with respect to each other. A quasi-periodic moiré pattern is observed in TBGs, and the size of the moiré cell increases continuously with increasing twisting angle θ (SANTOS; PERES; NETO, 2007). For some specific twisting angles θ_C, we can have a commensurate superlattice and we define its unit cell by a twisting vector which is denoted by two integers (n, m) (SATO et al., 2012).

The electronic structure of TBGs was calculated by dos Santos *et al* (SANTOS; PERES; NETO, 2007) in a continuum approximation, and it was observed that, for small twisting angles, the low energy dispersion is linear, as in a monolayer, but the Fermi velocity can be significantly smaller than the monolayer value. Li *et al* have shown that the moiré pattern generates van Hove singularities in the density of electronic states (DOS) of TBG (LI et al., 2009), that can be measured by scanning tunnelling spectroscopy, and the separation between these singularities increases with increasing twisting angle θ. (SATO et al., 2012; MOON; KOSHINO, 2013)

Raman spectroscopy has been used to study and characterize TBG samples and to probe the van Hove singularities in the electronic density of states (DOS). Havener *et al* (HAVENER et al., 2012) and Kim *et al* (KIM et al., 2012) reported detailed studies of the Raman spectra in a large number of TBG samples with many different twisting angles between 0 and 30 degrees, and showed that the G band is strongly enhanced when the photons of the Raman scattering process are in resonance with the separation between the van Hove singularities in the valence and conduction bands of TBGs (KIM et al., 2012; HAVENER et al., 2012). It was also shown in these works that the shape and width of the 2D band of bilayer graphene is strongly dependent on the twisting angle θ and on the laser energy (NI et al., 2009; KIM et al., 2012), and can be symmetric for some twisting angles.

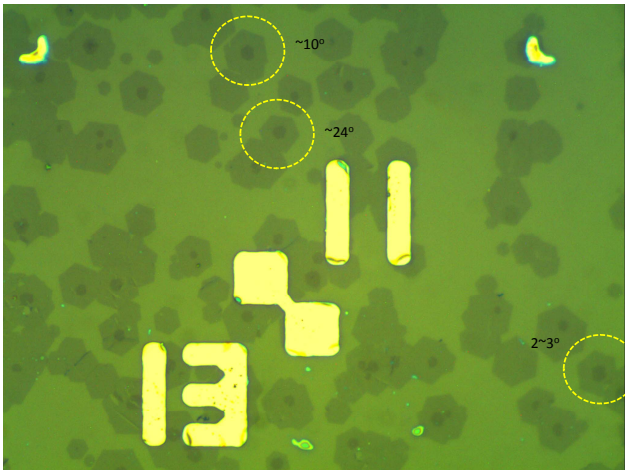

Figure 42 – Optical image of one sample presenting many different TBG flakes. The hexagons of the bottom and top layers are easily observed, and the twisting angle θ can be directly obtained from the optical images.

Ribeiro *et al* (RIBEIRO et al., 2015) also performed a Raman study of more than 100 samples of TBG with twisting angles from 0° to 30° using three laser lines in the visible range. A strong enhancement of G band intensity of TBG was observed only for samples with twisting angles between 9° and 17°, and it was concluded from these results that the van Hove singularity in the density of states does not occur by zone-folding the energy structure of commensurate superlattices, but by the moiré pattern that does not have necessarily a translational symmetry (RIBEIRO et al., 2015).

All the previous Raman studies of twisted bilayer graphene were using only a few number of laser lines, where it was not able to obtain the Raman excitation profile (REP) of the Raman bands and therefore, the exact resonance energy and the width of the resonance profile. For example, Ref. (WANG et al., 2013) only report measurements using 5 laser lines, and results presented in Ref. (HE et al., 2013) were obtained with only two laser lines. The Raman excitation profile (REP) of the G band was not reported in these previous works (WANG et al., 2013; HE et al., 2013) We present in this work a detailed resonance Raman study of samples of twisted bilayer graphene with different twisting angles, using 11 laser lines in the visible range. From the maxima of the REP of the G band we could obtain the precise energy of the optical transition associated with the van Hove singularities of TBGs, and from the width of the profile we were able to determine the broadening constant for the Raman process, which is inversely proportional to the lifetime of the photoexcited electron. Whereas the optical energy depends on the twisting angle of the TBG sample, in agreement with previous studies, we observed that the broadening is not dependent on the twisting angle of TBG samples with intermediate angles (θ between 10° and 15°.

6.2 Experimental Details

Our samples of bilayer graphene were grown by ambient pressure CVD on a polycrystalline Cu substrate. The control of the nucleation in early stage of the growth process allows the constituent layers to form single hexagonal crystals (LU et al., 2013). The samples were transferred to a 300nm Si/SiO_2 substrate for the Raman measurements. More details of sample preparation can be seen in reference (LU et al., 2013). Figure 47 shows the optical image of one sample of the TBG. Since the hexagons of the botton and top layers can be easily observed, the twisting angle of the TBG sample can be directly obtained from the optical images (RIBEIRO et al., 2015). Several different flakes in the of TBG sample were investigated.

The Raman experiments were performed in two different setups. The samples were first characterized in a Witec Alpha 300R pumped with a 488nm, 532nm and 633 nm laser lines, allowing us to obtain the Raman images shown in Figure 47. Samples where the G

band enhancement was observed were then investigated in triple monochromator tunable Raman system (Dylor XY) with a liquid-nitrogen-cooled CCD, and using 11 different lines of an Ar/Kr laser.

6.3 Results and discussion

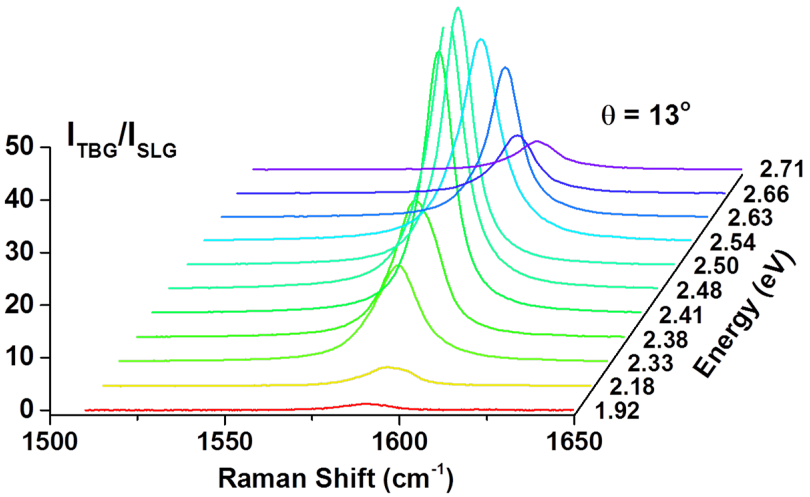

Figure 43 – Raman spectra of a twisted bilayer sample with $\theta = 13°$ recorded with the different excitation energies showed on the right side of the figure. The vertical axis shows the ratio I_{TBG}/I_{SLG} of the intensities of the Raman spectra in TBG and single layer graphene (SLG).

Figure 43 shows the spectra of one sample of TBG with $\theta = 13°$ obtained with many different laser lines. The intensity of the G band of the TBG was normalized by the intensity of the G band of single layer graphene (SLG) and the vertical axis shows the ratio I_{TBG}/I_{SLG}. Notice that the G band intensity is strongly dependent on the laser energy, and reaches a maximum around 2.48 eV, where it is 50 times more intense than the monolayer G-band. We have also obtained the resonance Raman spectra of several other samples of TBG with intermediate twisting angles and using many laser lines, and the results are similar to those reported in Fig. 43.

Figure 48 presents Raman excitation profile (REP) of the G band, that is, the G-band intensity versus laser excitetion energy, for 6 samples with intermediate twisting angles (θ between 12° and 15°) . It is well established that the giant enhancement of the G band in TBG is related to the resonance of the photons of the Raman process with the optical transitions between the van Hove singularities that appear in the cross-over of the two Dirac cones of the lower and upper graphene layers (HAVENER et al., 2012; KIM et al., 2012; WANG et al., 2013). The REP of the G band can be analysed by the equation that describes the intensity of the Raman peak as a function of the laser energy,

considering two discrete electronic levels, and given by:

$$I(E_L) = A \left| \frac{\langle f|H_{e-r}|b\rangle \langle b|H_{e-ph}|a\rangle \langle a|H_{e-r}|i\rangle}{[\hbar\omega_I - (E_A - E_0) - i\gamma_A][\hbar\omega_I - \omega_{ph} - (E_B - E_0) - i\gamma_B]} \right|^2 \tag{6.1}$$

where $\langle f|H_{e-r}|b\rangle$, $\langle b|H_{e-ph}|a\rangle$, and $\langle a|H_{e-r}|i\rangle$ are the matrix elements associated with the electron-photon, electron-phonon and electron-photon interactions, respectively, and E_{vHs} is the energy difference between the maxima of van Hove singularities in the valence and conduction bands. The damping constant Γ is related to the finite lifetime τ of the intermediate states, E_{ph} is the corresponding phonon energy. The full curves in Fig. 48 correspond to the fit of the experimental data by Eq.6.1, in which we assume that the matrix elements are constant, for simplicity. From the fitting we can obtain the precise value of the energies of van Hove optical transitions E_{vHs} and the damping constants Γ.

According to the theoretical predictions of optical absorption spectra by Moon and Koshino (MOON; KOSHINO, 2013), a double-peak structure is expected to be observed for samples with intermediate twisting angle, near 15°, as a consequence of electron-hole asymmetry. However, DFT calculations including electron-hole interaction have shown that this double-structure is washed-out (HAVENER et al., 2014). Moreover, experimental data of optical conductivity, presented in same paper, shows clearly the presence of only one peak (HAVENER et al., 2014).

Figure 45 shows the experimental values of E_{vHs} obtained from the fitting of the

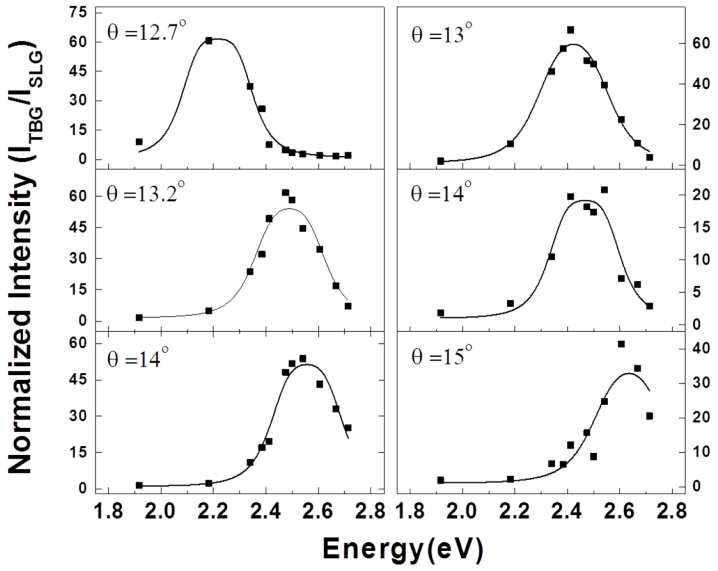

Figure 44 – Resonant Raman profile for the G band in six samples with intermediate twisting angles (θ between 12° and 15°). The vertical axis shows the ratio I_{TBG}/I_{SLG} of the intensities of the Raman spectra in TBG and single layer graphene (SLG).

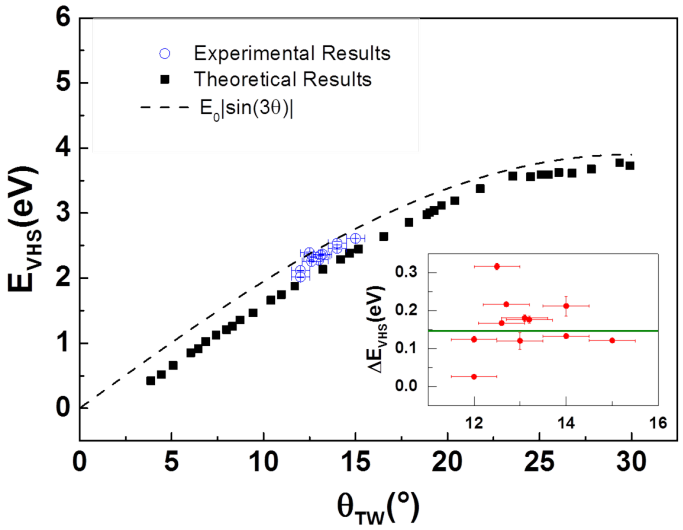

Figure 45 – Experimental (blue) and theoretical (black) values of the energy of the van Hove singularities as a function of the angle θ. The inset shows difference between experimental and theoretical values(red) and the average difference(green line). The dashed curve shows the plot of equation E_{vHs}= 3.9 eV $|sin(3\theta)|$ from Ref. (CAROZO et al., 2013)

REPs in Fig. 48 as a function of the twisting angle θ. The calculated values for E_{vHs} are also shown in Fig. 45 (RIBEIRO et al., 2015). Notice that all experimental points have energies slightly higher than the theoretical points, and the average difference is 0.14eV. The dashed curve in Fig. 45 shows the plot of equation E_{vHs}= 3.9 eV $|sin(3\theta)|$ from Ref. (CAROZO et al., 2013). This phenomenological expression provides a reasonable fitting of our data, but fails to explain the optical conductivity data for $\theta = 30°$, since the dependence of E_{vHs} on $sin(3\theta)$ has no physical basis (HAVENER et al., 2014).

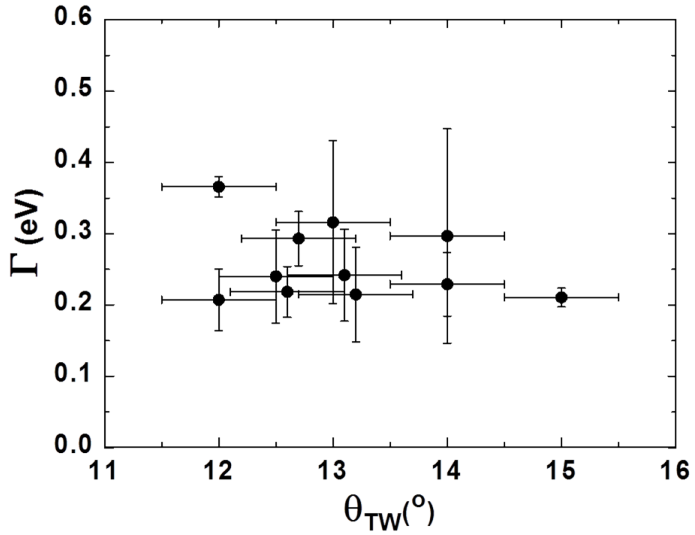

Figure 46 – Damping Constant (Γ) for G band versus angle for a group of samples.

Figure 50 shows the dependence of the damping constant Γ obtained from the fitting of the G band REPs, as function of the twisting angle θ. Notice that the average value around 250 meV is independent of θ in the narrow range of twisting angles investigated in this work (12° to 15°). Future Raman experiments using IR and UV laser lines will be needed to investigate samples with smaller and higher twisting angles and to determine the dependence of the Γ on the twisting angle. It is interesting to observe that this value is significantly higher than the damping constants of the Raman modes in single-wall carbon nanotubes, that are also enhanced by resonances with van Hove singularities in the electronic density of states, which are around 60 meV (FANTINI et al., 2004). This result suggests that additional scattering mechanisms decrease the life-time of photo-excited carriers in TBGs. The origin of these additional mechanisms can be electron-phonon or electron-electron scattering. Future theoretical works including these interactions will be needed to explain this experimental result.

6.4 Conclusions

In this work we presented measurements of the Raman excitation profile (REP) of the G band in twisted bilayer graphene (TBG) samples with different twisting angles, and using twelve different laser lines. From the analysis of the REPs using a theoretical expression for the Raman intensities we obtained the energies of the van Hove singularities generated by the moiré patterns, which agrees with the values measured by optical absorption (HAVENER et al., 2014). We also obtained the width of the resonance window, $\Gamma \approx 250$ meV, and this value does not depend significantly on the twisting angle in the range intermediate angles (θ between 10° and 15°). Finally, we observed that the REP of the G band enhancement in TBG is much broader than the REP of the Raman modes of carbon nanotubes, which are also enhanced by resonances with van Hove singularities, showing that extra electron-hole and electron-electron processes are involved in the resonance Raman process in TBGs.

7 The Intralayer and the Interlayer Electron-Phonon Interactions in Twisted Graphene Heterostructures

The results presented in this chapter were submitted in the article "Intralayer and interlayer electron-phonon interactions in twisted graphene heterostructures", by G.S.N. Eliel, M. V. O. Moutinho, A. C. Gadelha, A. Righi, H.B. Ribeiro, L. C. Campos, Po-Wen Chiu, K. Watanabe, T. Taniguchi, P. Puech, M. Paillet, T. Michel, P. Venezuela, M.A. Pimenta, in Nature Communications.

Abstract

The understanding of interactions between electrons and phonons in atomically thin heterostructures is crucial for the engineering of novel 2D devices. Electron-phonon (el-ph) interactions in layered materials can occur between electrons and phonons in the *same* layer or in $different$ layers. Here we report on the possibility of distinguishing *intralayer* and *interlayer* el-ph interactions in samples of twisted bilayer graphene (TBG) and of probing the *intralayer* process in graphene/h-BN by using Raman spectroscopy. In the *intralayer* process, the el-ph scattering occurs in a single graphene layer and the other layer (graphene or h-BN) imposes a periodic potential that back scatters the excited electron, whereas for the *interlayer* process the el-ph scattering occurs between states in the Dirac cones of adjacent graphene layers. Our methodology of using Raman spectroscopy to probe different types of el-ph interactions can be extended to study any kind of graphene-based heterostructure.

Interlayer electron-electron (el-el) and electron-phonon (el-ph) scattering processes emerge from the coupling of atomic layers in 2D heterostructures, and are essential for describing their physical properties and technological applications. The additional possibility of controlling the twisting angle θ between layers opens a fascinating route to achieve novel tunable quantum devices. For twisted bilayer graphene, the interaction between electrons of different layers generates van Hove singularities (vHs) in the density of electronic states, whose energies are θ dependent (SANTOS; PERES; NETO, 2007; SATO et al., 2012; MOON; KOSHINO, 2013). Electron-phonon coupling is also a fundamental interaction that affects a broad range of phenomena in condensed matter physics such as electron mobility and thermal conductivity. In atomically thin heterostructures, the interaction can involve both electrons and phonons in the same layer (*intralayer* el-ph

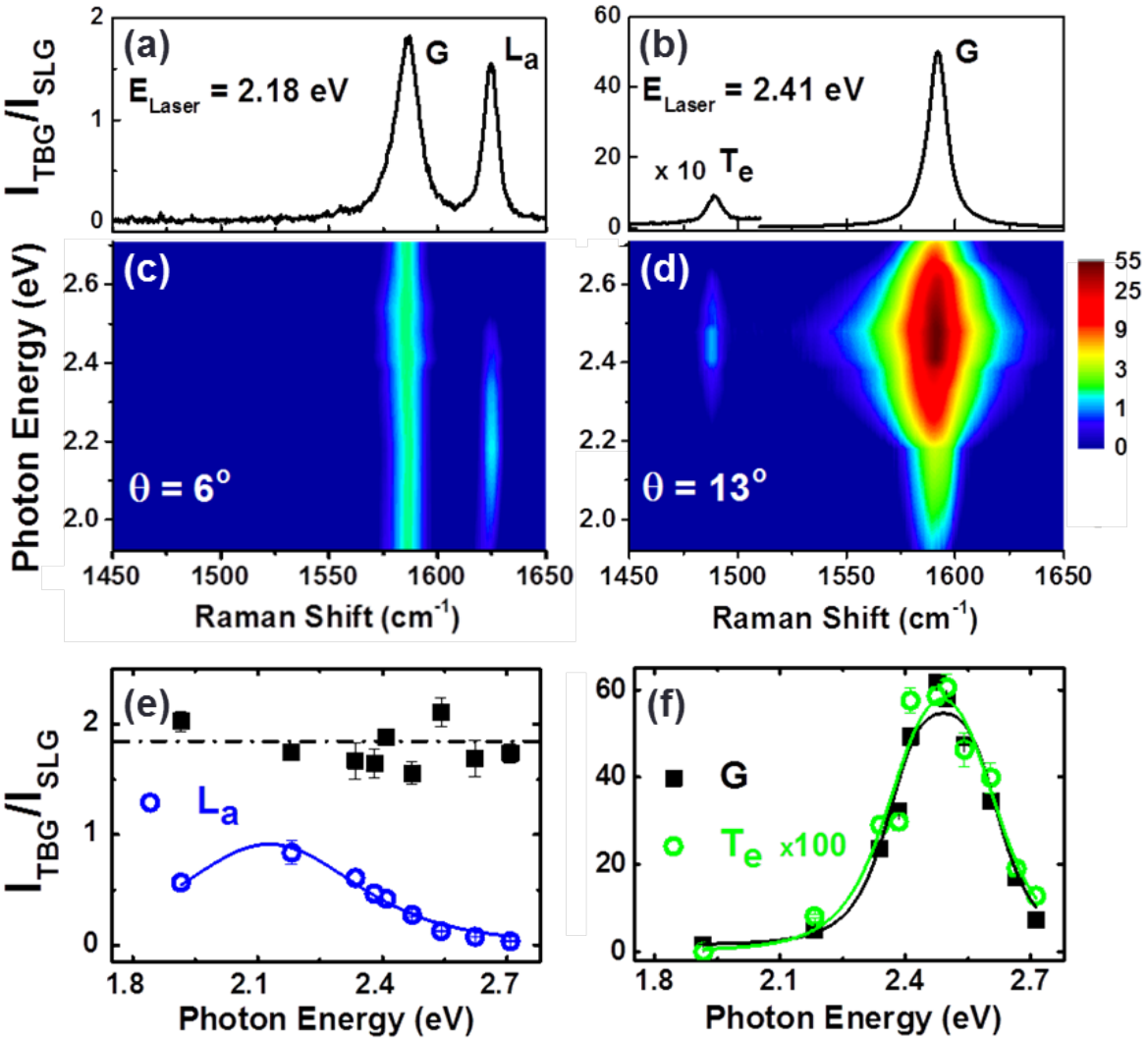

Figure 47 – Raman results of TBG in the visible range. (a) and (b) Raman spectra in two samples of TBG with $\theta = 6^o$ and 13^o recorded with the 2.18 eV and 2.41 eV laser lines, respectively. The vertical scale, I_{TBG}/I_{SLG}, corresponds to the ratio of the peak intensities of the Raman spectra in TBG and single-layer graphene (SLG). The peak around 1620 cm^{-1} in part (a) is called L_a since it comes from the LO phonon branch and is activated by the *intralayer* electron-phonon scattering process, whereas the peak at 1480 cm^{-1} in part (b) is called T_e since it comes from the TO phonon branch and is activated by the *interlayer* process. (c) and (d) Excitation Raman maps of the samples with $\theta = 6^o$ and 13^o recorded with several laser lines with photons energies in the visible range (1.9 to 2.7 eV). (e) Raman excitation profile (REP) of the G band (black squares) and the L_a peak (blue circles) of the sample with low twisting angle ($\theta = 6°$). (f) Raman excitation profile (REP) of the G band (black squares) and of the T_e peak (green circles) of the sample with intermediate twisting angle ($\theta = 13°$). The T_e peak intensity was multiplied by ≈ 100 times for comparison with the G band REP.

interaction) or in adjacent layers (*interlayer* el-ph interaction). The *interlayer* el-ph interaction has been recently observed in WSe_2/h-BN heterostructures (Jin et al., 2017).

Here we report the ability of Raman spectrocopy to probe and distinguish *interlayer* and *intralayer* el-ph interactions in graphene heterostructures. This is experimentally attained by tuning the energy of the excitation photon and observing the resonances of the Raman modes in different samples of twisted bilayer graphene (TBG) and graphene on the top of h-BN (gr/h-BN), with previously determined mismatch twisting angle θ. Prominent new peaks are observed in the Raman spectra of TBG samples and come from phonons within the interior of the Brillouin zone (BZ) of graphene that are folded to the centre of the reduced Moiré pattern BZ. The frequencies of these phonons depend on the twisting angle θ (GUPTA et al., 2010; RIGHI et al., 2011; CAROZO et al., 2011; RIGHI et al., 2013; CAMPOS-DELGADO et al., 2013; CAROZO et al., 2013; WANG et al., 2013). We show here that they can be activated either by the *intralayer* or the *interlayer* processes. The *intralayer* process was also observed in the Raman spectra of gr/h-BN samples and allows the experimental determination of their mismatch angle between the crystallographic axes of graphene and h-BN. In this case, the el-ph process occurs in a graphene monolayer and the h-BN surface imposes a periodic potential needed for the electron backscattering in the resonant Raman process. This effect is expected to be sensitive to the strength of the interaction between monolayer graphene and any other single layer or crystalline surface.

Experiments were first done in TBG flakes, that appear in an optical microscope as an external hexagon (first layer) and an internal one (with two layers) (LU et al., 2013), where the twisting angle θ can be determined from the optical images using the procedure reported in reference (RIBEIRO et al., 2015) (see appendix B). Figures 47(a,b) show Raman spectra in two samples with $\theta = 6°$ and 13°, recorded with the 2.18 eV and 2.41 eV laser lines, respectively. The vertical scale, I_{TBG}/I_{SLG}, corresponds to the ratio of the peak intensities in TBG and single-layer graphene (SLG). The ratio $I_{TBG}/I_{SLG} = 1.8$ for the G band intensity (around 1580 cm^{-1}) of the $\theta = 6°$ sample shown in Fig. 47(a) corresponds to the observed value far from resonances (RIBEIRO et al., 2015). However, for the $\theta = 13°$ sample shown in Fig. 47(b), the G band ratio I_{TBG}/I_{SLG} is more than 50. This huge increase of the G band intensity has already been observed in previous Raman studies of TBGs (NI et al., 2009; KIM et al., 2012; HAVENER et al., 2012; RIBEIRO et al., 2015) and explained by the resonance of the incident photons with the optical transition between van Hove singularities (vHs) in density of electronics states of a TBG.

In addition to the G band, we can observe in Figs. 47(a,b) the presence of extra peaks respectively above and below the G band, around 1620 cm^{-1} and 1480 cm^{-1}. Extra peaks have been observed in many previous Raman studies of TBGs (GUPTA et al., 2010; RIGHI et al., 2011; CAROZO et al., 2011; RIGHI et al., 2013; CAMPOS-DELGADO et

al., 2013; CAROZO et al., 2013; WANG et al., 2013). They arise from phonons of graphene with momentum $\hbar q_M$, where q_M is a vector of the Moiré pattern reciprocal lattice, that are folded to the centre of the reduced BZ and become Raman-active (GUPTA et al., 2010; RIGHI et al., 2011; CAROZO et al., 2011; RIGHI et al., 2013; CAMPOS-DELGADO et al., 2013; CAROZO et al., 2013; WANG et al., 2013). In 2010, Gupta et al. (GUPTA et al., 2010) proposed that the extra peaks were activated by double-resonance Raman (DRR) process where momentum conservation is provided by the potential of the Moiré reciprocal lattice. Carozo et al. (CAROZO et al., 2011) attributed the new peaks below and above the G band position to the intervalley and intravalley DRR processes, and estimated the resonance energies as a function of θ for these two processes. The valleys considered in this work belong to the same graphene layer and, therefore, both cases correspond to an *intralayer* electron-phonon scattering process.

In 2013, Carozo et al. (CAROZO et al., 2013) and Wang et al. (WANG et al., 2013) reported measurements TBG samples with intermediate twistting angles (13°-16°) using different laser lines. In both works, the appearance of new peaks in the range 1380-1450 cm^{-1} was observed to occur in the same spectra where the G band was enhanced. This resonance behaviour could not be explained by the predictions of the DRR process involving the periodic potential of the Moiré (CAROZO et al., 2011), and revealed that a different electron-phonon process involving phonons with momentum $\hbar q_M$ may exist. We will show below that the new phonons observed in these works (CAROZO et al., 2013; WANG et al., 2013) are activated by the *interlayer* electron-phonon scattering processes.

The extra peaks below and above the G band position have been called in the literature as the R and R′ peaks (CAROZO et al., 2011; CAROZO et al., 2013). Since they can be activated either by the *intralayer* or the *interlayer* electron-phonon scattering process, we will adopt for these peaks the notation A_α, where $A = T$ or L refers to the branch (TO or LO) of the unfolded phonon and α refers to the electron-phonon scattering mechanism (a or e for *intralayer* and *interlayer* processes, respectively). It will be clear below that the extra peaks above and below the G band shown in Figs. 47(a,b) might be called L_a and T_e, respectively.

In order to explain the different resonance behaviour of the Raman peaks in TBGs, we first made multiple-excitation Raman measurements using many different laser lines in the visible range (see section Experimental Methods), which allowed us to obtain the accurate Raman excitation profile (REP) of Raman peaks in samples with small and intermediate twisting angles. Figures 47(c,d) shows the multiple-excitation Raman results for the samples with $\theta = 6°$ and $\theta = 13°$ samples, respectively. The vertical scale corresponds to the energy of the incident photon, and the peak intensities are represented by the colour bar on the right side. We can observe in Fig. 47(c) that the G band ratio I_{TBG}/I_{SLG} of the $\theta = 6°$ sample does not depend on the photon energy and is always

around 1.8, an expected value far from resonance conditions (RIBEIRO et al., 2015). On the other hand, the L_a peak clearly exhibits a resonance behaviour and reaches the maximum intensity for photon energies around 2.2 eV, where it becomes as intense as the G band in SLG. Figure 47(d) shows that results for the $\theta = 13°$ sample exhibit a different behaviour. Now, both the G band and the T_e peak exhibit a resonance behaviour and are enhanced in the same excitation energy range.

Figures 47(e,f) show the Raman excitation profile (REP) of the G, L_a and T_e peaks, that is, the intensity of each peak as a function of the photon energy, for the $\theta = 6°$ and $\theta = 13°$ samples, respectively. Figure 47(e) shows that the REP of the L_a peak exhibits maximum enhancement at approximately 2.2 eV and has a width γ around 0.7 eV. This value of γ agrees with the result in a previous UV Raman study of TBGs (RIGHI et al., 2013). In the case of the $\theta = 13°$ sample shown in Fig. 47(f), the G band and the T_e peak exhibit very similar REPs, except for the fact that the intensity of the extra peak was multiplied by ≈ 100 for comparison. The data in Fig. 47(f) were fitted by the expression of the Raman-cross section based on the third-order perturbation model (CAROZO et al., 2013), where the fitting parameters are the energies of the optical transitions between vHs, E_{vHs}, and the width γ of the REP. The values of the parameters that fit the experimental data in Fig. 47(f) are $E_{vHs} = 2.37$ eV and $\gamma = 0.25$ eV. Notice that this value of γ agrees with the width of the peaks in the optical absorption spectra of TBGs (HAVENER et al., 2014). Several other samples with low (4°-6°) and intermediate (12°-16°) twisting angles were investigated using multiple excitation Raman measurements, and results similar to those shown in Figure 47 are presented in the Supplementary Material. The dependence of the values of E_{vHs} and γ for the G band on the twisting angle θ is shown in Ref. (ELIEL et al., 2017).

In order to understand the origin of the results presented above, we performed a theoretical simulation considering two different electron-phonon processes that take part in the Raman scattering. Details of the calculations are given in the Theoretical Methods section. In one case, the excited electronic state from one layer is scattered by phonon with momentum $\hbar\mathbf{q}_M$ to another state in the same layer (*intralayer* process) whereas, in the other case, the excited electron is scattered to an state of the other layer (*interlayer* process). We will show that these two mechanisms give rise to resonances at different energies.

Figure 48(a) shows the Brillouin zones of two graphene layers A and B twisted by $\theta = 13.2°$ and represented, respectively, by the grey and black hexagons. The vectors q_1 , q_2 and q_3 correspond to the unit vectors of the Moiré reciprocal lattice (we will consider in this work that $\mathbf{q}_M = q_1$ or q_2 or q_3). The reduced BZ of the Moiré superlattice is shown by the small red hexagon in the centre of Fig. 48(a). The *intralayer* and *interlayer* processes are represented in the energy versus momentum curves calculated for the $\theta = 13.2°$ TBG

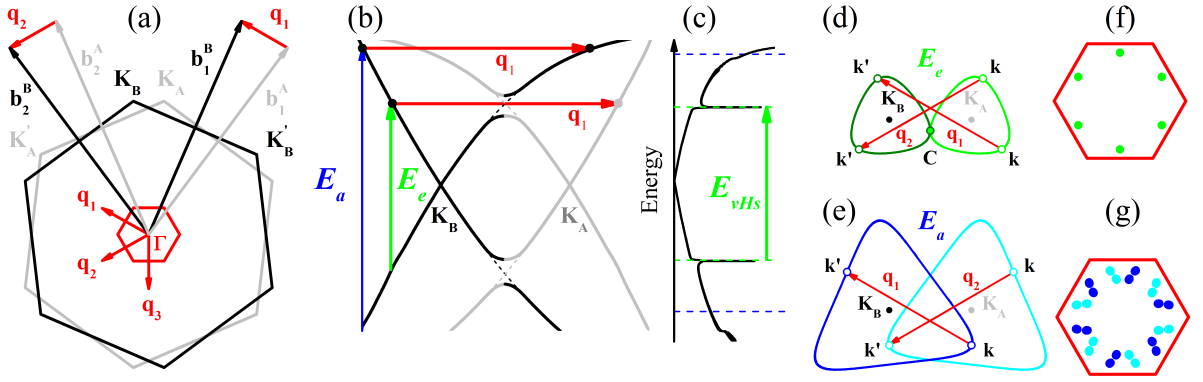

Figure 48 – (Colour online) Intralayer and interlayer el-ph scattering processes. (a) The grey and black hexagons correspond to the Brillouin zones (BZ) of two graphene layers, denoted by A and B, twisted by the angle $\theta = 13.2°$. The small red hexagon represents the reduced BZ and the vectors q_1 , q_2 and q_3 correspond to the unit vectors of the Moiré reciprocal lattice. (b) Energy versus momentum diagram calculated for $\theta = 13.2°$. The grey (black) curves represent the Dirac cone of layer A (layer B). The vertical blue arrow represents the optical transition for the *intralayer* process, and the vertical green arrow represents the transition for the *interlayer* case. The horizontal red arrows represent the wave vector q_1 of the phonon. (c) Density of electronic states (DOS) of the TBG and optical transition between vHs in the valence and conduction bands. (d) *Interlayer* el-ph process where a phonon with momentum $\hbar q_1$ connect the states k and k'. The light and dark green curves correspond to the equi-energies E_e around K_A and K_B. (e) *Intralayer* el-ph process where both states k and k' are in the equi-energies E_a of the same layer (light and dark blue curves around K_A and K_B, respectively). (f) *Interlayer* (green dots) and (g) *intralayer* (blue dots) electronic states k and k' represented in reduced BZ scheme.

and shown in Fig. 48(b). In the *intralayer* process, an incident photon with energy E_a (represented by the vertical blue arrow) creates an electron-hole pair, and a phonon with momentum $\hbar q_M$ (represented by the horizontal red arrow) scatters the excited electron to another state in the same Dirac cone (layer B in this case). For simplicity, we are not plotting in this figure the change in energy between these two states since the phonon energy is much smaller than the energy of visible photons. In the *interlayer* process also represented in Fig. 48(b), an incident photon represented by the green vertical arrow and with energy E_e creates one electron-hole pair, but now the electron from one layer (layer B) is scattered to a state of the other layer (layer A) by a phonon with momentum $\hbar q_M$. In both cases, the electron is then scattered back elastically to the first excited state by the Moiré potential, with wave vector $\mathbf{q}_M$, for electron-hole recombination and emission of the scattered photon.

Figure 48(d) illustrates the *interlayer* process in the graphene reciprocal space. The dark and light green curves correspond to the equi-energy curves E_e around the Dirac

points K_B and K_A, respectively. An excited electron with momentum $\hbar$k from the Dirac cone of one layer (dark green curve) is scattered by a phonon with momentum $\hbar q_M$ (red arrows) to an state with momentum $\hbar k'$ in the Dirac cone of the other layer (light green curve). The lowest possible value of E_e occurs when the equi-energies curves of the two layers tangentiate, as shown in Fig. 48(d). In this situation, the anti-crossing between states of the Dirac cones gives rise to van Hove singularities (vHs) in the density of states (DOS), shown in Fig. 48(c). For photons with energies below E_e, the difference $|k - k'|$ is always smaller than $|q_M|$ and the *interlayer* condition cannot be satisfied. Therefore, the minimum energy for the *interlayer* scattering process, E_e^-, corresponds to the energy separation E_{vHs} between the vHs in the valence and conduction bands of a TBG.

The *intralayer* el-ph scattering process is schematically represented in Fig. 48(e). Now, the light and dark blue curves around K_A and K_B, respectively, correspond to the curves of constant energy E_a. In this case, the excited states with momenta $\hbar k$ and $\hbar k'$ belong to the Dirac cones of the same layer (dark or light blue curves). The *intralayer* process is similar to the double-resonance Raman (DRR) mechanism that gives rise to the disorder-induced D and D′ bands in the Raman spectrum of graphene (PIMENTA et al., 2007). For the disorder-induced bands, the electron is scattered back to the initial excited state by a defect whereas, in the case of TBG, the back-scattering is provided by a periodic potential of the Moiré pattern. This DRR process, where momentum conservation is provided by a vector q_M of the Moiré lattice, has been called previously as the umklapp DRR process (RIGHI et al., 2011).

So far, we discussed the two processes in the extended BZ scheme, where the activated phonons have finite q_M. In the reduced BZ scheme, they are folded to the centre of the reduced BZ and have zero momentum. The first-order Raman process can be accomplished in this scheme since the two excited states k and k' in the extended BZ in Figure 48(d) are folded to the same point in the reduced BZ, which are represented by the green dots in Fig. 48(f). They are located at the saddle point in the electronic structure of TBG, near the M point in the reduced BZ, that gives rise to a van Hove singularity (vHs). The *intralayer* process can be also represented in the reduced BZ scheme. Figure 48(g) shows that the two excited states k and k' in the extended BZ in Figure 48(e) are folded to the blue dots within the reduced BZ. Differently from the case of the *interlayer* process, that occurs near the M point of the reduced BZ, the *intralayer* process occur for states at general positions within the interior of the reduced BZ.

In order to determine the resonance energies E_a and E_e, we calculated the restricted density of joint electronic states that satisfy the *intralayer* and *interlayer* conditions. For the calculation, we divided the graphene BZ in a 2400 × 2400 **k**-points grid and, for each twisted angle θ, we stored the number of joint electronic states satisfying the restriction $|E^\alpha(\mathbf{k}) - E^\alpha(\mathbf{k}')| \leq \varepsilon$ where the superscript α symbolises the valence or the

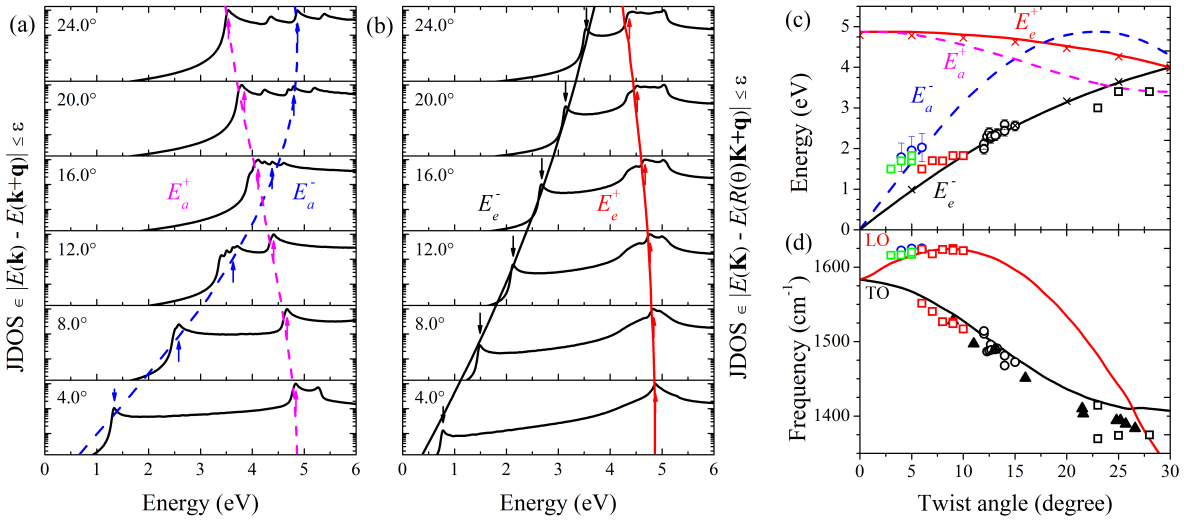

Figure 49 – Resonance energies and phonon frequencies for the intralayer and interlayer e-ph processes. (a) and (b) Joint density of states that satisfy the *intralayer* and *interlayer* processes, respectively, for some twisting angles θ. (c) The dashed blue, full black, dashed pink and full red curves represent the calculated values of E_a^-, E_e^-, E_a^+ and E_e^+ as a function of function of the twisting angle θ. The blue and black open circles correspond to the resonance energies of the extra peaks observed in the visible Raman spectra in samples with, respectively, small and intermediate angles. The green and red open circles correspond to the laser energies where the extra peaks observed in the IR Raman spectra in samples with θ in the ranges 3-5° and 6-0° have the maximum intensity. The black open squares correspond to the resonance energies of the extra peaks observed in the UV Raman spectra for samples with large twisting angles (22-28°). The black crosses correspond the the energies of the peaks in the optical absorption spectra of TBG reported in Ref. (HAVENER et al., 2014). (d) The red and black curves represent the dependence of the TO and LO phonon frequencies as a function of θ. The blue, black, green and red open circles and the black squares correspond to the frequencies of the extra peaks observed in the visible, IR and UV Raman spectra as described in part (c). The black triangles correspond to the results reported by Wang et al (WANG et al., 2013).

conduction bands and $\varepsilon = 0.02$ eV is an arbitrary tolerance. For the *intralayer* case we have $\mathbf{k}' = \mathbf{k} + \mathbf{q}_M$ because the two electronic states, $\mathbf{k}$ and $\mathbf{k}'$, are connected by $\mathbf{q}_M$ while, for the *interlayer* process, $\mathbf{k}' = R(\theta)\mathbf{k} + \mathbf{q}_M$, being $R(\theta)$ the rotation matrix that takes the Dirac cone of one layer into the Dirac cone of the other layer. For a better understanding of this model see Appendix A.

Figures 49(a,b) show the calculated joint density of states (JDOS) that satisfy the *intralayer* and *interlayer* resonance conditions, respectively. The results were smoothed by Lorentzian functions with 0.04 eV of FWHM and normalised by the maximum intensity for best visualisation of the peaks. In both cases, some peaks are observed in the restricted

JDOS, and their energies depend on the twisting angle θ. The position of the low energy peaks increase whereas the position of the high energy peaks decrease with increasing values of θ. These two maximum are associated with electronic transitions close to K and M points of the graphene, and will be called E^- and E^+. For the *intralayer* process, the positions of E_a^- and E_a^+ are indicated by the blue and purple arrows in Fig. 49(a), respectively, and the positions of E_e^- and E_e^+ for the *interlayer* process are marked in Fig. 49(b) by the black and red arrows. Notice in Fig. 49(b) that E_e^- corresponds in fact to the onset for the *interlayer* process, which occurs when the Dirac cones touch each other as shown Fig. 48(d), giving rise to vHs in the valence and conduction bands with energy separation E_{vHs}.

Figure 49(c) shows the calculated values of E_a^-, E_e^-, E_a^+ and E_e^+ as a function of the twisting angle θ represented by the dashed blue, full black, dashed pink and full red curves, respectively. The experimental values of the resonance energies obtained from the analysis of the REPs of the extra Raman peaks are also plotted in Fig.49(c). The blue open circles in Fig. 49(d) represent the resonance energies of the peaks in the range 1600-1620 cm^{-1} that are observed in samples with small angles (4° to 6°). They nicely agree with the calculated E_a versus θ results represented by the dashed blue curve. The values of the resonance energies obtained from the REPs of the extra peaks in the range 1450-1550 cm^{-1} for samples with intermediate twisting angles (12°-16°) are plotted as full and open black circles in Figure 49(c). These points are close to the black curve that represents E_e^- as a function of θ. The crosses in Figure 49(c) represent the experimental values of optical transition energies E_{vHs} measured directly by optical conductivity (HAVENER et al., 2014). It is interesting to note that, despite the fact that our model does not consider electronic coupling between the layers that opens a mini-gap which split the valence and the conduction bands in TBL, the agreement between the minimum possible value E_e^- shown in Fig. 49(a) and the experimental values of the optical transitions (HAVENER et al., 2014) is remarkable.

The red and black curves in Fig. 49(d) display, respectively, the calculated frequencies of LO and TO phonons with momenta $\hbar q_M$ as a function of θ. The frequencies of the extra peaks of samples with small (intermediate) values of θ are plotted as open blue (black) circles in Fig. 49(d). By comparing our experimental results with the calculated results of the resonance energies and phonon frequencies shown in Figs. 49(c,d) we conclude that, using visible photons, the Raman peaks below the G band come from TO phonons and are activated by the *interlayer* process, whereas the peaks above the G band come from the LO phonon branch and are activated by the *intralayer* process.

In principle, the *interlayer* electron-phonon scattering process can also activate LO phonons and gives rise to the L_e peak for samples with intermediate angles. The L_e peak was not observed in our experiments using visible photons, since it is close to the

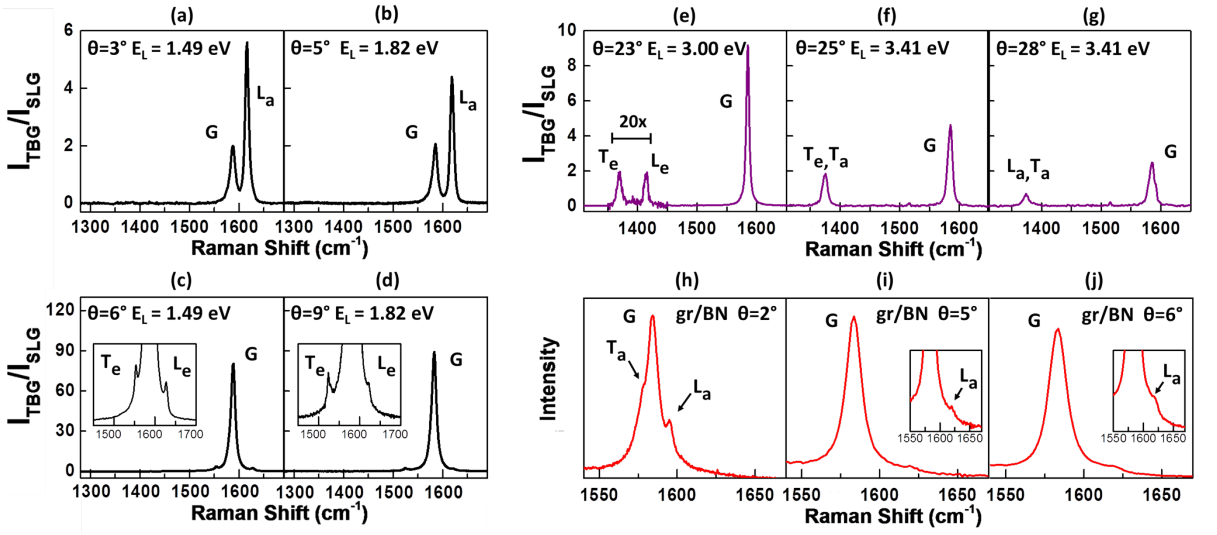

Figure 50 – Raman results in TBGs using IR and UV radiation and results in gr/h-BN samples. (a-d) IR Raman spectra in four samples TBG samples with $\theta = 3°$, 5°, 6° and 9°, recorded with the 1.49 or 1.82 excitation energy, as indicated in each figure. (e-g) UV Raman spectra of three TBG samples $\theta = 23°$, 25° and 28°, recorded with the 3.00 or 3.41 excitation energy. (h-j) Raman spectra in three different samples of graphene on the top of h-BN, with twisting angles $\theta = 2°$, 5° and 6°, recorded with the 1.96 eV excitation energy

G band and possibly masked by the huge G band enhancement. However, for samples with θ around 10° and measured using the 1.96 eV laser line, Campos-Delgado et al. (CAMPOS-DELGADO et al., 2013) reported the observation of a peak at 1622 cm^{-1}, that might be assigned to the L_e. We can also expect to observe the activation of phonons of the TO branch by the *intralayer*, but we did not observe any T_a peak in the investigated TBG samples using visible excitation energies.

The calculated results presented in Fig. 49(c) show that, for TBG samples with small twisting angles, both the *intralayer* and the *interlayer* processes are expected be observed using infrared excitation energies (below 1.9 eV). This prediction was indeed observed in our IR Raman results performed in many different samples with θ in the range 2°-9°, using three laser lines in the IR with energies 1.49 eV, 1.70 eV and 1.82 eV (see Experimental Methods). The IR Raman spectra for samples with $\theta = 3°$, 5°, 6° and 9° are presented in Figs. 50(a-d). In the spectra of the samples with $\theta = 3°$ and 5°, shown in Figs. 50(a,b), the ratio I_{TBG}/I_{SLG} of the G band around 2 reveals that the LO phonon is activated by the *intralayer* el-ph process. Interestingly, the L_a peak is stronger than the G band, suggesting that the electron-phonon coupling for the LO phonon increases with decreasing θ, when the wave vector q_M tends to the centre Γ of the BZ. In contrast, the *interlayer* el-ph process occurs for the TBG samples with $\theta = 6°$ and 9° shown in Figs. 50(c,d), where a huge enhancement $I_{TBG}/I_{SLG} \approx 80$ is observed. In the tails of the G band we can observe two extra peaks below and above the G band that are assigned,

respectively, as the T_e and L_e peaks. The new result here is the observation of a LO phonon activated by the *interlayer* el-ph process (L_e peak), that was not observed in the results obtained with visible photons and shown in Fig. 47). This result can also be explained by the increase of electron-phonon coupling for the LO phonons when q_M tends to zero. The laser energies where the extra peaks observed in the IR Raman spectra in samples with θ in the ranges 3°-5° and 6°-9° have the maximum intensity are shown, respectively, by the green and red open circles in Fig. 49(c). The frequencies of the corresponding peaks are plotted in Fig. 49(d) and are in nice agreement with the calculated values.

The theoretical predictions in Fig. 49(c) for samples with large twisting angles θ show that extra peaks are expected to appear in the UV Raman spectra (for excitation energies above 3 eV). Figure 49d shows that the activated phonons are close to the K point of the single-layer graphene, and come from both the TO and LO branches, with frequencies in the range 1350-1420 cm^{-1}. In the pioneer Raman study of graphene folded onto itself, Gupta et al. (GUPTA et al., 2010) observed non-dispersive extra peaks in the range 1370-1395 cm^{-1}, and showed that they were enhanced in the UV Raman spectrum (E_{laser} = 3.41 eV). Righi et al (RIGHI et al., 2011) studied the UV Raman spectra of TBGs and observed several extra peaks in the range 1370-1420 cm^{-1}, but the twisting angles θ were not determined in this work. In both studies (GUPTA et al., 2010; RIGHI et al., 2011) the appearance of new peaks was not accompanied by the enhancement of the G band, as expected for an *intralayer* el-ph process. In contrast, the UV data of Wang et al (WANG et al., 2013) in TBG samples with large values of θ show the activation of new peaks in spectra where the G band also exhibits an enhancement of 5 to 20 times, indicating thus an *interlayer* electron-phonon scattering. The laser energies where the extra peaks of the samples with large values of θ in the ranges 22°-28° exhibit the largest intensity and the frequencies of these peaks observed in the UV Raman spectra are represented by the black open squares in Figs. 49(c,d), respectively. The results for the phonon frequencies reported by Wang et al (WANG et al., 2013) are also plotted in Fig. 49(d), and represented by the black triangles.

Figures 50(e-g) show the UV Raman spectra of three samples with θ = 23°, 25° and 28°, performed with the 3.00 and 3.41 eV excitation energies (details are described in the section Experimental Methods). The vertical scale gives the ratio I_{TBG}/I_{SLG}. We can see in the spectra new peaks with frequencies in range 1370-1420 cm^{-1}, as predicted in Figs. 49(c,d). Notice in Fig. 49(c) that for large twisting angles, both the *intralayer* (E_a^+) and *interlayer* (E_e^-) resonances occur in the same energy range (3-4 eV). In principle, we can distinguish these two processes by observing the enhancement of the G band of TBG, which is a signature of the *interlayer* process.

In the spectrum of the θ = 23° sample recorded with the 3.00 eV line and shown in Fig. 50(e), the ratio I_{TBG}/I_{SLG} for the G band is ≈ 9, suggesting that the two peaks around

1380 cm^{-1} and 1410 cm^{-1} come from phonons of the TO and LO branches, respectively, and are activated by the *interlayer* el-ph process (T_e and L_e peaks). On the other hand, in the spectrum of the $\theta = 28°$ sample recorded with the 3.41 eV line and shown in Fig. 50(g), the ratio $I_{TBG}/I_{SLG} \approx 2$ reveals the activation by the *intravalley* el-ph process. We thus assign the extra feature around 1370 cm^{-1} as a L_a peak, although we can not rule out the possibility of being a T_a peak, since, as shown in Fig. 49(d), the LO and TO phonon branches are close to each other in the range of large θ. In Figure 50(g), the ratio I_{TBG}/I_{SLG} for the G band is around 4 and only one extra peak is observed. In this case, possibly both processes are occurring simultaneously. The peak position around 1380 cm^{-1} suggests that it comes from a phonon of the TO branch, and it can be thus assigned as a T_a/T_e peak. The laser energies where the extra peaks shown in Figs. 50(e-h) exhibit the largest intensity and their positions are also plotted in Fig. 49(c) and (d), respectively, and compared with the calculated TO or LO branches near the K point of graphene. The agreement between the experimental and theoretical values of the phonon frequencies is not as good as in the case of the results in the visible range. This is due to the shift in the calculated phonon frequencies described in the Theoretical Methods section.

As discussed above, the *intralayer* electron-phonon process occurs in one graphene layer, and the second layer only imposes a periodic potential needed for momentum conservation in the double-resonance Raman process. Therefore, extra peaks are also expected to appear in the Raman spectra of graphene deposited on the top of any atomically flat substrate, assuming that the interaction graphene/substrate is strong enough to scatter electrons. In a recent study of graphene on the top of h-BN, Eckmann et al. (ECKMANN et al., 2013) reported the observation of weak extra peaks both below and above positions of the the G band in graphene, and suggested that they arise from the graphene/h-BN interaction.

In order to check this assumption, we prepared graphene/BN samples by transferring single-layer graphene to the top of a h-BN crystal. From the analysis of optical images, where the crystallographic edges of graphene and BN are evidenced, we can estimate the twisting angle θ (see appendix B). Raman measurements were performed in graphene/h-BN samples with different twisting angles, specially in range of small θ where the *intralayer* process occurs for photons in the visible range. Figures 50(h-j) show the Raman spectra in three samples of graphene/h-BN, with $\theta = 2°$, 5° and 6°, in the range 1550-1650 cm^{-1} In the three cases, we can observe very weak peaks above the G band frequency, assigned as L_a peaks. In the case of the $\theta = 2°$ sample, we can also observe in Fig. 50(h) a sharp peak below the G band, and this result is thus an experimental manifestation of the T_a process. The positions of the extra peaks in graphene/BN are approximately the same of TBG graphene, except for the case of samples with very small twisting angles (θ <2°) (ECKMANN et al., 2013). They are much less intense than the extra peaks in bilayer graphene, showing that the imposed potential of h-BN on graphene is much weaker than

graphene-graphene interaction. Results shown in Figs. 50(h-j) thus demonstrate that extra peaks enhanced by the *intralayer* electron-phonon process in TBG occur whenever graphene interacts with an atomically flat crystalline surface that imposes a periodic potential for the electrons of graphene.

In summary, we report in this work the observation of *intralayer* and *interlayer* electron-phonon interactions in twisted graphene heterostructures with different mismatch twisting angles by Raman spectroscopy. Measurements performed with many different laser excitation energies allowed us to conclude that phonons of graphene with momenta q_M can be activated by two different resonant electron-phonon processes: the *interlayer* process, where the electron scattering occurs between the Dirac cones of different graphene layers, and the *intralayer* process which occurs in a single graphene layer, and the other layer or substrate only imposes a periodic potential that activate the phonons in the Raman spectrum. The observation of new peaks in the Raman spectrum of single layer graphene on the top of h-BN crystals proves that the *intralayer* electron-phonon process can occur not only in TBG, but also whenever graphene is in contact with any periodic layer or substrate. The intensity of these extra peaks is expected to provide the strength of the interaction between monolayer graphene and the substrate. On the other hand, the activation of new phonons by the *interlayer* electron-phonon process reported in many previous studies in the literature occur only in TBGs.

This work highlights the importance of understanding fundamental electron-phonon interactions in heterostructures of 2D materials, which affect thermal and transport properties in these systems. The possibility of distinguishing *intralayer* and *interlayer* electron-phonon interactions in bilayer graphene, and of studying the interaction of monolayer graphene with a crystalline substrate using light scattering allow new ways to design devices applications of 2D heterostructures and is crucial for the engineering of new devices.

8 Conclusions and Pespectives

We have experimentally investigated a large number of TBG samples with different twisting angles θ using visible laser excitation. We have shown the enhancement of the G band as a function of θ for three laser energies. We presented the dependence of the G band width with θ showing that, for small angles, the width increases asymmetrically, and this result can be associated with the increase in number of phonon branches that present energies near to the G band in the Γ point of the phonon dispersion. We reported for the first time resonant Raman profile of the relevant Raman features of TBG samples using 11 laser lines. We have obtained the relevant parameters of the G band REP, the resonance energy and the width. From the resonance energy results, we could validate the continuum model of van Hove singularities, but the energy obtained from the experimental data was higher than that of theoretical data for the same angle. Comparing these widths with the van Hove singularity width and the width of the optical absorption, we show that electron-electron and electron-hole interactions play a major role in the REP‘s width.

We also reported on the observation of intralayer and interlayer electron-phonon interactions in TBG samples with different twisting angles θ. Measurements performed with many different laser excitation energies in the visible range allowed us to obtain the REP of the different bands. From the resonance behavior of these peaks, we concluded that there are two different resonant electron-phonon processes: the interlayer process, where the electron scattering occurs between the Dirac cones of different layers, and the intralayer process involving states in the same Dirac cone. The interlayer mechanism is responsible for the G band‘s huge enhancement in a broad range of energies ($\gamma \approx 250$) meV, and we show that accurate values of the resonance energy E_e can only be obtained from the analysis of the G band REP. Phonons with wavevectors q_M are folded to the center of the TBG BZ, and give rise to extra peaks in the spectra, like T_e peak, the interlayer process from TO branch. We show that T_e band is non-dispersive and has almost the same resonance profile as the G band. Moreover, we observed that the T_e Raman resonant profile is similar to that of G band. Using the fact that T_e position does not change with the excitation energy, we conclude that the use of the T_e is a good strategy to obtain the angle when close to a resonance.

The intralayer el-ph scattering process occurs in a single layer and a periodic potential imposed by the second layer provides momentum conservation. This process can be understood in the extended BZ scheme as a specific double-resonance Raman (DRR) process in graphene, where momentum conservation is provided by the wavevector of the moiré lattice (a moiré DR or M-DR process). Our results show that the intralayer el-ph process occurs whenever graphene is in contact with another periodic layer or substrate.

In particular, we were able to observe these new phonons in the Raman spectrum of graphene/h-BN bilayer samples with small twisting angle. On the other hand, the interlayer electron-phonon process is expected to occur only in TBG, since the resonance mechanism involves the vHs in the DOS of TBG, which only arises due to the coupling of the Dirac cones of the two layers. This thesis highlights the importance of understanding the intralayer and interlayer electron-phonon interactions in heterostructures of 2D materials, that can affect thermal and transport properties in these systems. The possibility of distinguishing intralayer and interlayer electron-phonon interactions in bilayer/multilayer suggests new ways to design devices made of 2D heterostructure where graphene is one of the layers, which is crucial for the engineering of new devices.

As perspectives, we will study more systematically both mechanisms, mainly in UV and IR range, trying to understand better the electron-phonon interaction with the Dirac‘s delta-like defects generated by the moiré patterns.

Calculations of modulating potential for heterostructures with graphene and the production of those structures to evaluate the relation of this potential and the intralayer mechanism Raman signal is an important direction to pursue.

Another perspective is the generalization of the model presented in this Thesis to other materials, opening the posibility of easily obtaining stacking angles and to probe electron-phonon interactions using this modulation potential to activate specific regions of the Brillouin zone.

A Density of states that satisfies the umklapp double-resonance Raman process in twisted bilayer graphene

In this appendix we explain the process that gives the laser energies where we expect to find Raman features in twisted bilayer graphene (TBG) associated with the intralayer double resonance Raman process. In this process, momentum conservation is provided by a wavevector of the moire lattice (umklapp double-resonance process or U-DR). It occurs when the moiré wavevectors connect two real electronic states in the graphene electronic structure of one layer. Figure 51 shows the Brillouin zone of the top and bottom layers of the TBG and the three wavevectors $\vec{M}_1$, $\vec{M}_2$, and $\vec{M}_3$ of the moiré lattice.

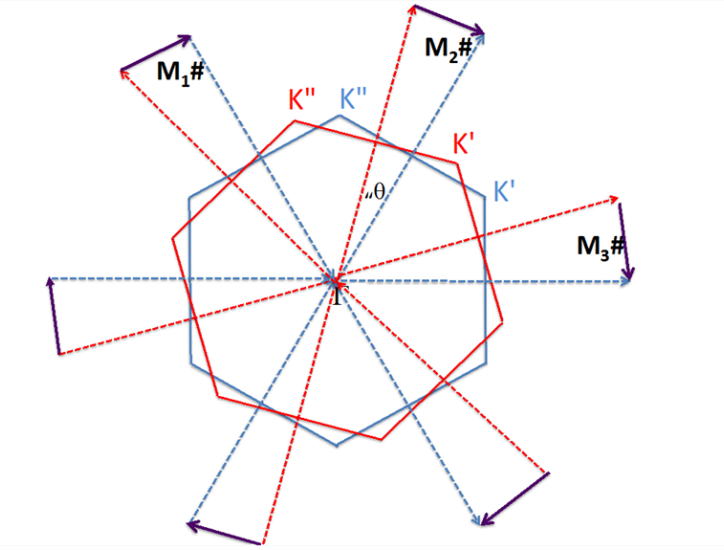

Figure 51 – Reciprocal lattice of twisted bilayer graphene in the extended picture, $\vec{M}_1$, $\vec{M}_2$ and $\vec{M}_3$ are the moiré wavevectors.

If the two electronic states are in the same Dirac cone, we call a intra-valley U-DR process, whereas electronic states in different Dirac cones (K and K' points) give rise to the inter-valley U-DR process. Figure 52 illustrates the intra-valley and inter-valley processes. A important point is that we are only considering electronic states with different slope signs of the electronic dispersion along the moiré vector direction.

Based on this idea, a computer program was made to evaluate the laser excitation energies in which this process happens. For illustration purposes, we use the very simplified graphene electronic structure here. In order to obtain the energy difference between the

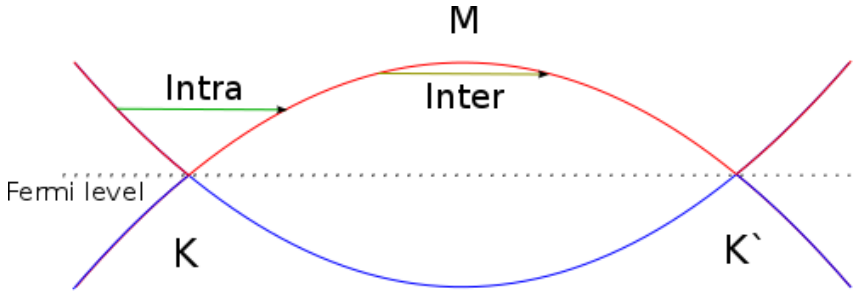

Figure 52 – Intra-valley and inter-valley process for the same moiré vector.

valence and conduction bands, we used the equation below (JORIO et al., 2011):

$$E(k_x, k_y) = 2 * t\sqrt{1 + 4\cos\frac{3k_x a}{2}\cos\frac{\sqrt{3}k_y a}{2} + 4\cos^2\frac{k_y a}{2}} \tag{A.1}$$

where t=3.033eV is the tight-binding hopping parameter for first neighbors calculation. Notice that using this very simple equation we do not consider the asymmetry between the valence and conduction bands. The purpose of this appendix is only to present the physical model, since a detailed work using a more realistic electronic structure was done in chapter 7.

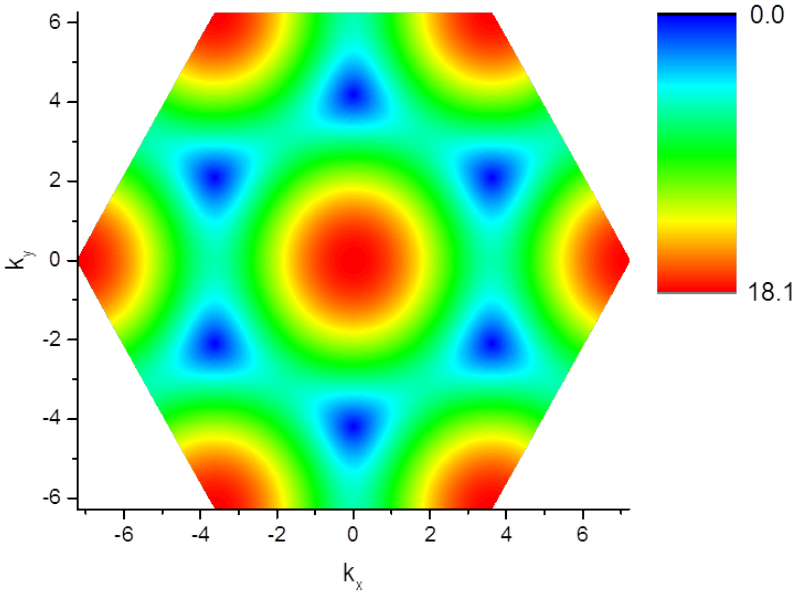

Figure 53 – Energy difference between valence and conductive band for π electrons in graphene.

A plot of equation A.1 is shown in Figure 53, The K points are in the middle of the blue triangles and the Γ points are in the middle of the red circles.

In order to calculate the energies where the U-DR processes occurs, we first map the energies where the moiré wavevector can connect two real electronic states. For that we consider the condition below:

$$E(\vec{k}+\vec{M}) - E(\vec{k}) = 0 \tag{A.2}$$

For a numerical implementation, we consider that the difference in Eq. 2 is not exactly zero, but smaller than a constant.

$$E(\vec{k}+\vec{M}) - E(\vec{k}) < 0.1eV \tag{A.3}$$

The value of 0.1eV was set arbitrarily, and was used just to present the results of the model. In fact this value has the order of magnitude of graphene optical phonons.

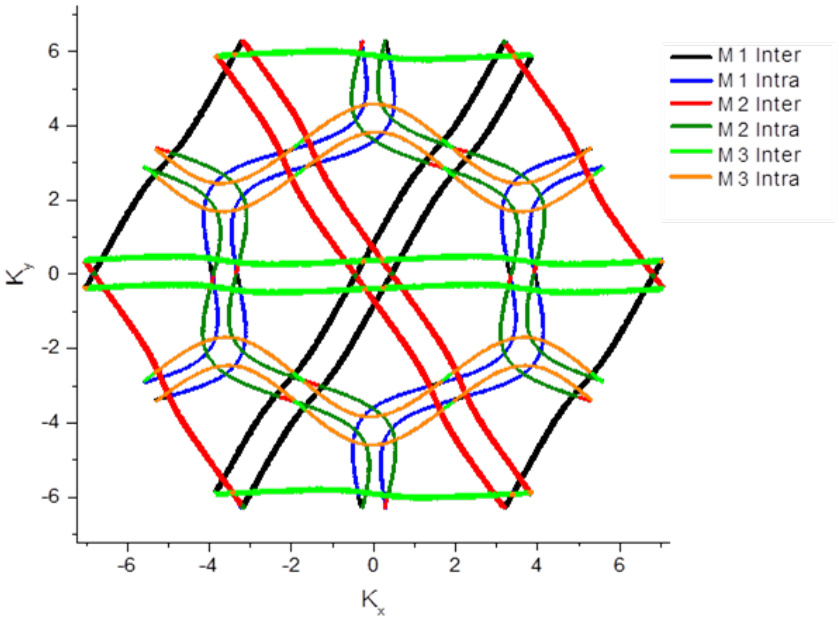

Figure 54 – Solutions for equation A.3 for all 3 moiré vectors for a twisting angle of 6°

Figure 54 shows the curves in the BZ of graphene formed by all points in which Eq. (3) is satisfied, considering a twisting angle of 6°. We are considering in this figure all the three wave vectors $\vec{M}_1$, $\vec{M}_1$ and $\vec{M}_1$ shown in Figure 51, and the intra-valley and inter-valley processes shown in Figure 52. As we will be showing as follows, we just need to consider the processes given by one wave vector ($\vec{M}_1$) since the other ones have the same results rotated by ±120°.

Figure 55 shows the evolution of the solution in function of the twisting angle, given by the curves formed by the solutions of Equation A.3. Red points are the intravalley process and black points are the intervalley process for TBG with different angles, only considering the wave vector $\vec{M}_1$.

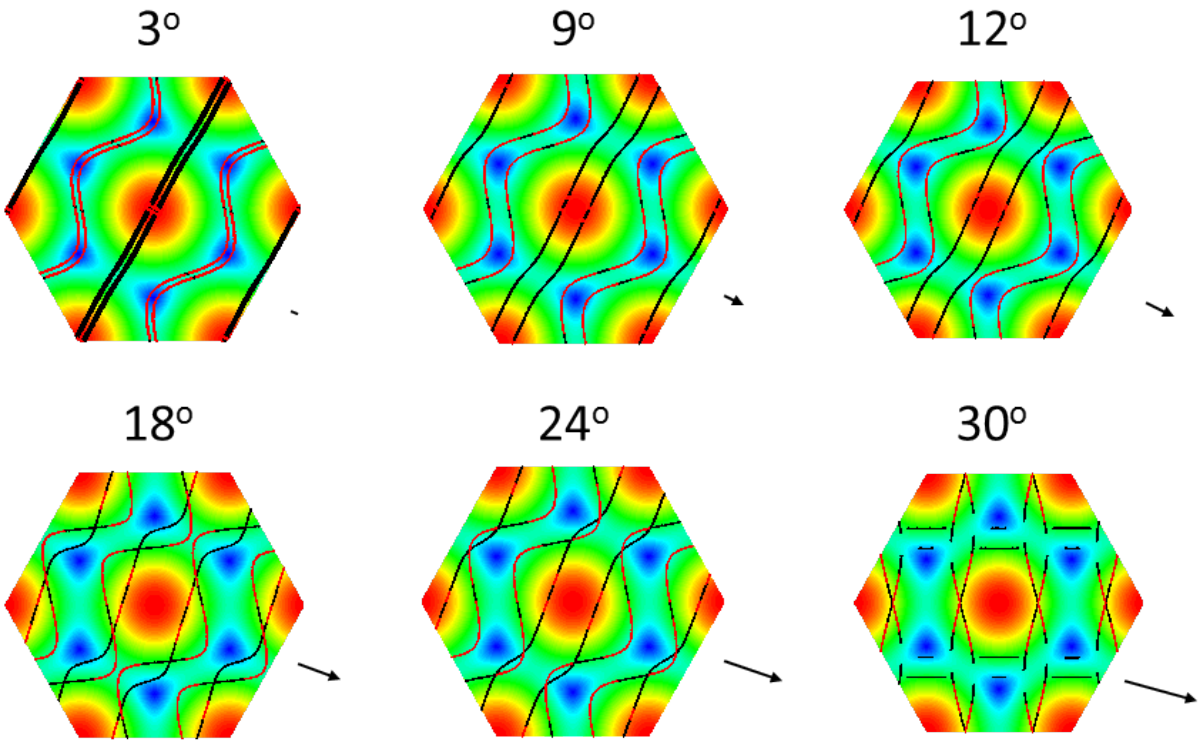

Figure 55 – Intravalley(red) and intervalley(black) process solutions for $\vec{M}_1$ for different angles, arrow represents the moiré vector.

Using the solutions in Figure 55, we can obtain the density of electronic states that satisfy Equation A.3, that we will call here uDR-DOS(E), does that is the number of states with energies between E and E+ΔE, where ΔE in this case is 0.02 eV.

Figure 56 shows the uDR-DOS(E) of the intravalley and intervalley process for TBGs with different twisting angles θ. The results for θ>24°are shown in the right part of Figure 56, and present a different behaviour due our transitions rules.

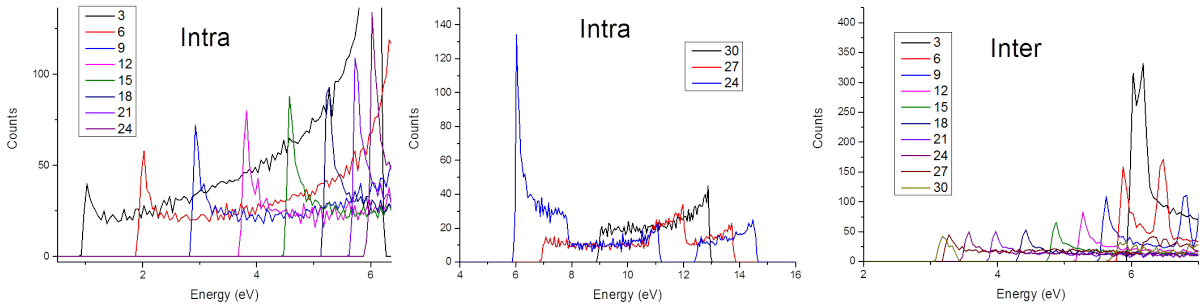

Figure 56 – Intravalley density of states for different twisting angles, in (a) angles up to 24°and in (b) from 24 to 30°. In (c) intervalley density of states

It is very interesting to note that there are some maxima in the uDR-DOS shown in Figure 56. The first maximum is associated with the expected transition energy for each process. In 57, we plot the energies of the first peaks shown in Figure 56 as a function of

the twisting angles θ. These energies correspond to the laser energies (E_laser) in which we expect to see Raman peaks activated by these mechanisms.

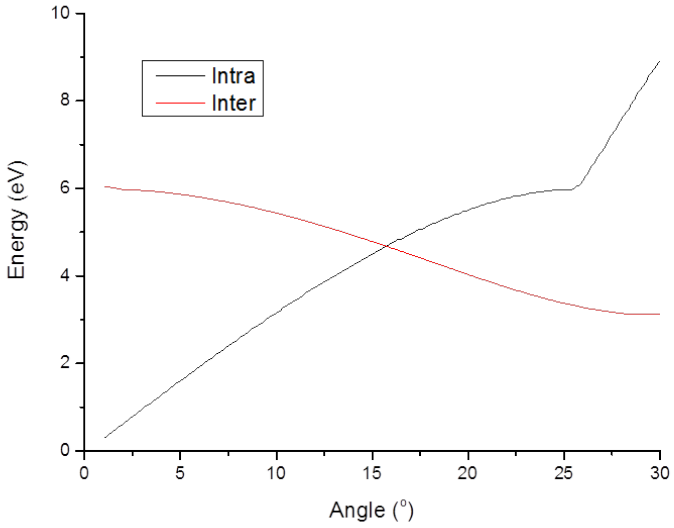

Figure 57 – Energy of the first peak in jDOS for intravalley(black) and intervalley(red) u-DR processes.

B The Intralayer and the Interlayer Electron-Phonon Interactions in Twisted Graphene Heterostructures: Additional information

In this appendix, we provide additional information for the results presented in the chapter 7.

B.1 Theoretical Methods

The electronic and phonon structures were obtained by folding the SLG calculation results. For SLG we follow the calculation procedure given in(VENEZUELA; LAZZERI; MAURI, 2011). The electronic structure calculations are based on a tight-binding approach in which the parameters are fitted to reproduce density functional theory (DFT) calculations with many-body corrections, while the phonon dispersion was obtained from many-body corrected DFT calculations. The many-body corrections change the phonon slope of the highest optical branch near **K** (with respect to DFT), reproducing the Kohn anomaly and providing a much better agreement with inelastic x-ray scattering measurements for graphite (MAULTZSCH et al., 2004). These curves describe accurately the D band of graphene when a red shift of 40 cm^{-1} is applied for phonons close to the **K** point. However, in order to reproduce the phonons close to the graphene G band, we blue shifted all frequencies by 20 cm^{-1}. Even though the calculations were done only by folding the SLG results, the physics of the *intralayer* and *interlayer* processes in TBG is nicely captured.

B.2 Sample Characterization

The twisted bilayer graphene (TBG) samples were obtained via CVD method as detailed in Ref. PoWen, and transferred to different substrates: a 300 nm SiO_2/Si substrate for visible measurements, 90 nm SiO_2/Si substrate for UV measurements, and fused silica for IR measurements. Each graphene layer presents a hexagonal shape with zigzag edges (LU et al., 2013). The mismatch twisting angle θ can be obtained from the analysis of the optical images, as shown in Figures 58(a) and (d). We can clearly see in the Raman maps represented in Figures 58(b),(c),(e) and f the difference of the response for the 4° sample (Figs. 58(b) and (c) and the 13° sample (Figs. 58 (e) and (f)), excited with 1.92 eV (633 nm) and 2.33 (532 nm) laser lines, respectively. Notice in Figs. 58(c) and (f) that the extra peaks appear only in the TBG regions.

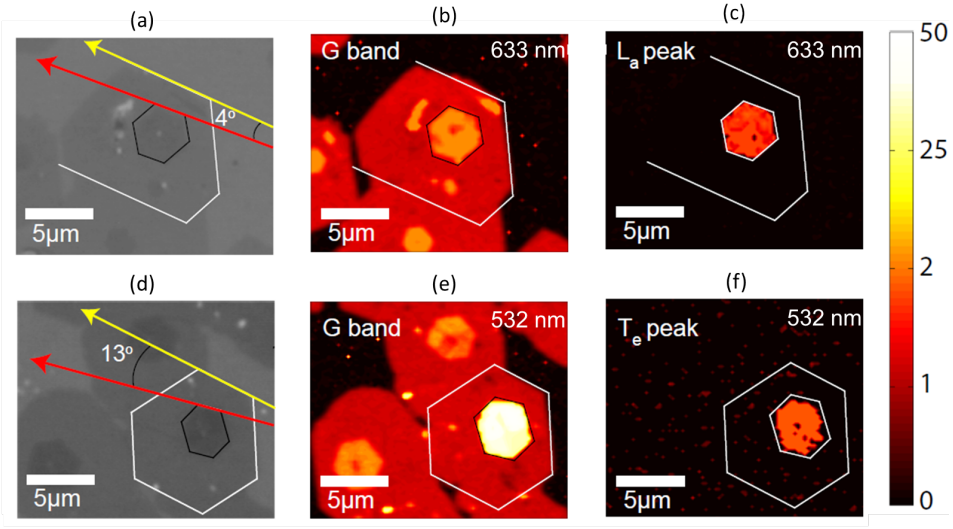

Figure 58 – (a),(d) Optical images for two different samples used to obtain the twisting angle θ. (b),(e) Raman maps of the G band for the samples shown in parts (a) and (d), respectively. (c) Raman map of the L_a peak and (f) Raman map of T_e peak.

The gr/BN samples were produced by mechanical exfoliation of graphene, which was then transferred to a h-BN substrate, providing the gr/h-BN heterostructure with a given mismatch twisting angle θ. Figure 59(a) shows the AFM phase image of a gr/BN sample, where we can observe the h-BN and graphene flakes by contrast. Figures 59(b-d) show Raman images of three different gr/BN samples. To obtain these images, we mapped the G band of graphene (in blue) and the h-BN peak at 1366 cm^{-1} (in red). In the region where h-BN is covered with graphene, the image presents a purple color. In these figures, the graphene and h-BN edges are highlighted by black and white lines, respectively. The mismatch twisting angles θ between graphene and h-BN edges were obtained from the analysis of the images and the obtained values are shown in the Figures. The real angle can be θ or $\theta + 30$ due to the unknown orientation of graphene edges.

B.3 Raman spectra of different samples using visible light

For the multiple excitation measurements in the visible range, we used an Ar/Kr laser that provides many different excitation lines from 1.92 to 2.71 eV. Figure 60(a-c) show the spectra for three samples in the *interlayer* resonance condition. In these cases, we can clearly observe the G band enhancement of almost 70 times, and the appearance of the T_e peak, in the spectral range of 1450 to 1530 cm^{-1} for these samples. The Raman spectrum of the sample with $\theta = 5°$ shown in Fig. 60(d) shows the presence the L_a peak. The intensity of the G band is almost constant, whereas the L_a peak exhibits a resonance profile.

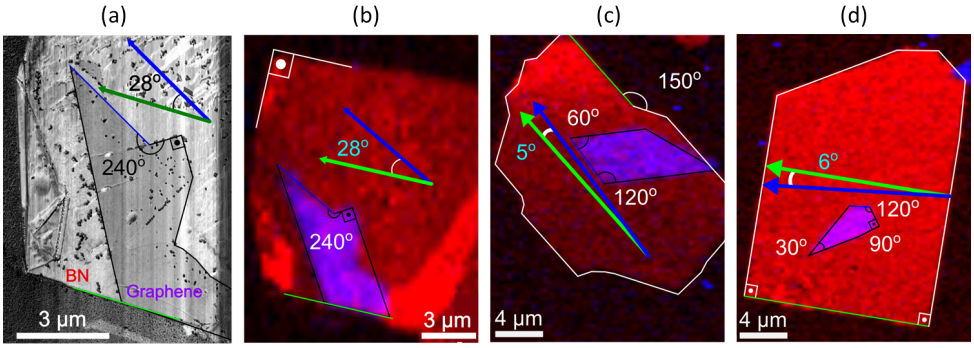

Figure 59 – (a) AFM image of a gr/BN sample. (b-d) Raman maps of the G band (blue) and h-BN band (red) for three different gr/BN heterostructures, where the numbers in light blue represent the mismatch twisting angle between the crystallographic edges of graphene and h-BN.

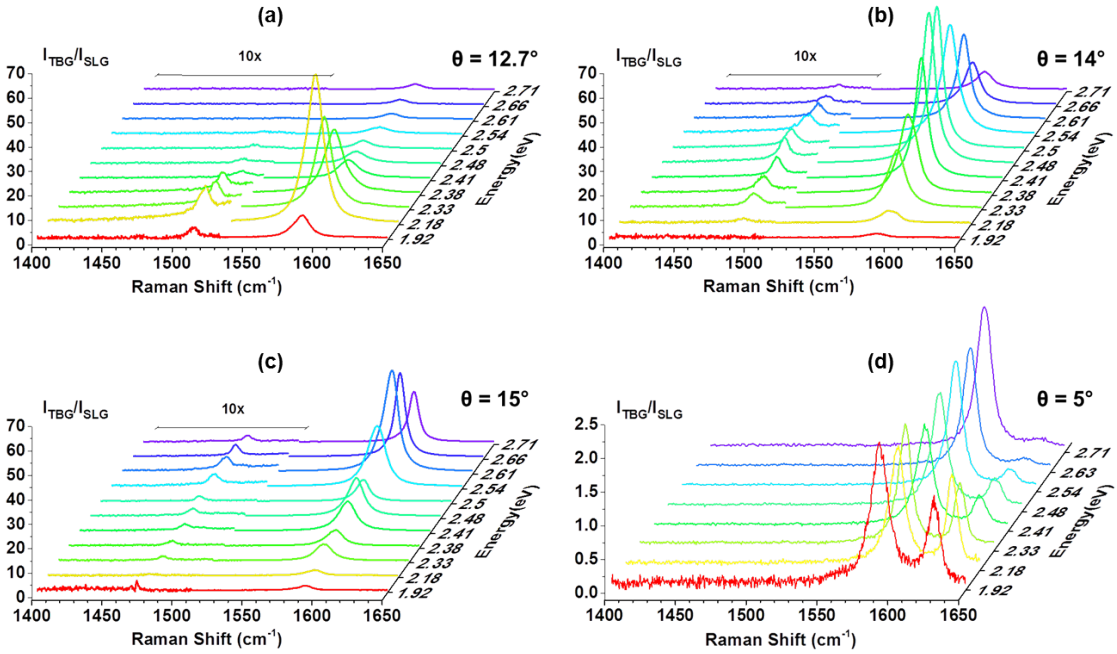

Figure 60 – Raman spectra for four different TBG samples using using different laser lines in the visible range. The twisting angles θ are represented in the figures.

Figure 61 show the REP of both peaks in different TBG samples, normalized for the SLG intensity. The intensity of the T_e peak was multiplied by $\approx 100\times$ for comparison. The REP results for the intralayer process for two samples that presented the L_a peak are presented in Figure 62. The G band intensity is constant in this case.

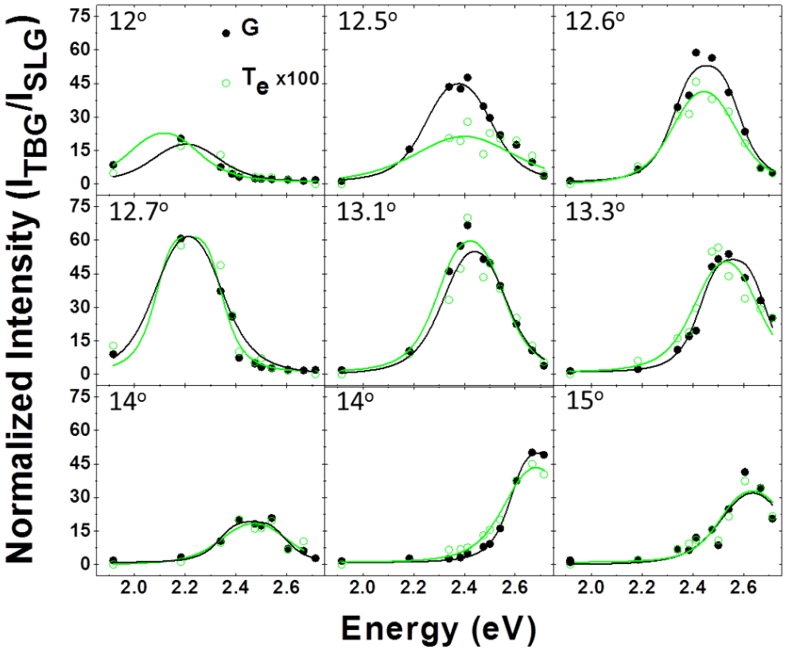

Figure 61 – Raman excitation profiles (REP) of the G (black squares) and T_e (green circles) bands in different samples. The values of θ for each sample are presented in the figures.

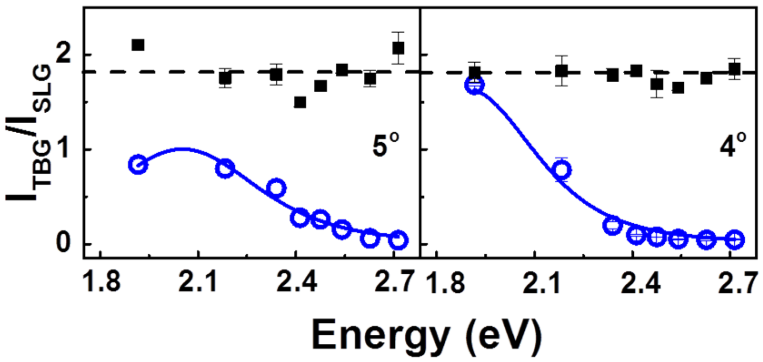

Figure 62 – Raman excitation profiles (REP) of the L_a (blue circles) bands in two different samples. The dashed black line is the average relative intensity of the G band, around 1.8.

B.4 Analysis of the Raman excitation profiles in twisted bilayer graphene

The full curves in Figure 61 correspond to the best fit of the experimental data by the expression of the Raman-cross section based on the third-order perturbation process model, and given by:

$$I(E_L) = \left| \frac{K}{(E_L - E_R - i\Gamma)(E_L - E_{ph} - E_R - i\Gamma)} \right|^2 \tag{B.1}$$

where E_L, E_R and E_{ph} are the laser energy, the resonance energy and the phonon energy, respectively. K is a constant related with the product of the transition matrix elements.

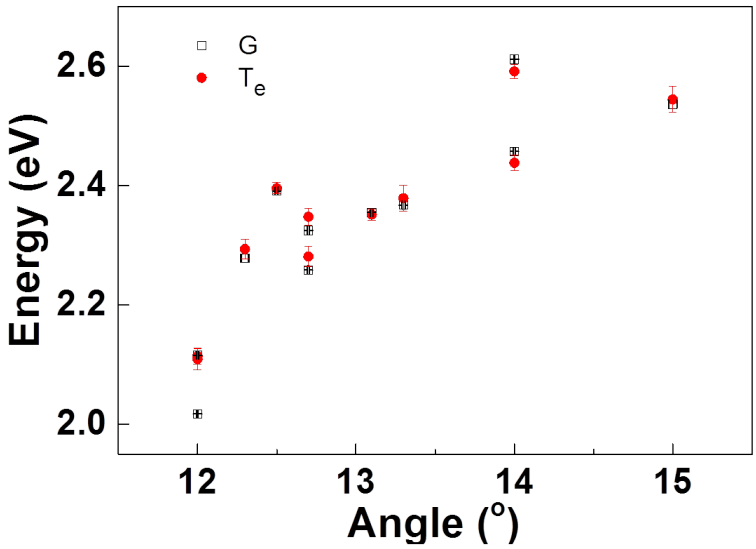

Figure 63 – Energy as a function of the twisted angle for G (black squares) and T_e (red circles) bands obtained via REP analysis

The values of E_R that fit the of G and T_e bands shown in Figure 62 as a function of θ are presented in Figure 63. Notice that the values of E_R for these two bands are practically the same, within the precision of the experiments, showing that these peaks are enhanced by the same effect, which is the transition involving the van Hove singularities. In conclusion, the analysis of the REPs of the G and Te bands with Eq. B.1 provides an accurate determination of of the E_{vHs} values.

Figure 64 shows the values of the damping constant Γ of all obtained REPs. In the case we can observe a considerable difference for the G and T_e bands. In the case of G band (black squares), the average value of the damping constant Γ is around 250 meV, but for T_e (red triangles) this value increases, being around 330 meV. Considering that both processes are first-order Raman process in the reduced Brillouin zone, we can conclude

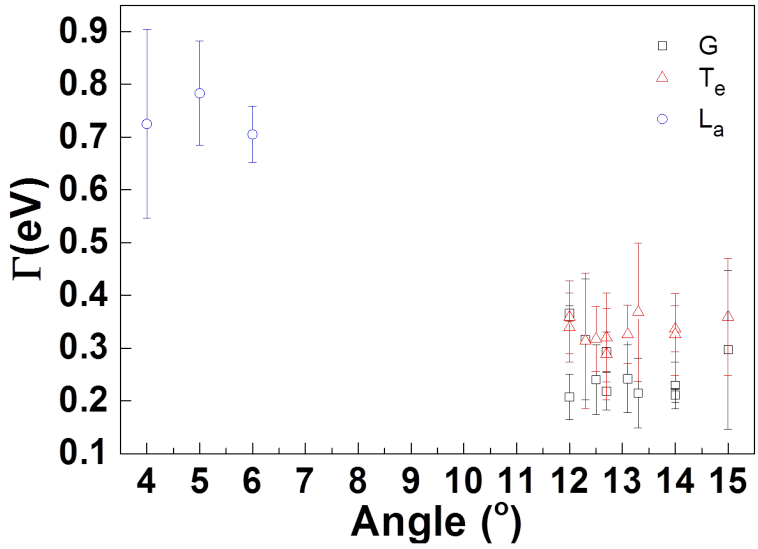

Figure 64 – REP's damping constant as a function of the twisted angle for G (black squares),T_e (red triangles) and L_a (blue circles) bands.

that this difference arises from the different electron-phonon interaction, that decreases the photoexcited electron lifetime.

For the intralayer case, the resonance energies E_a are shown in Figure 49. The width Γ of resonance is around 0.7 eV and it is also represented by the blue circles in Figure 64.

B.5 Raman spectra of different samples using infrared light

For the Raman measurements performed in the infrared range, three laser lines were used: 680, 730 and 830 nm. In this case, we used a fused silica substrate to avoid interference effects. Figure 65 shows all results for samples that present an enhanced signal for interlayer (a) and intralayer (b) mechanisms. Due to the few number of laser lines, no resonance profile can be obtained. Therefore, the data presented in Figure 49 correspond to the laser line energy of the spectrum where the Raman peaks exhibit the maximum enhancement.

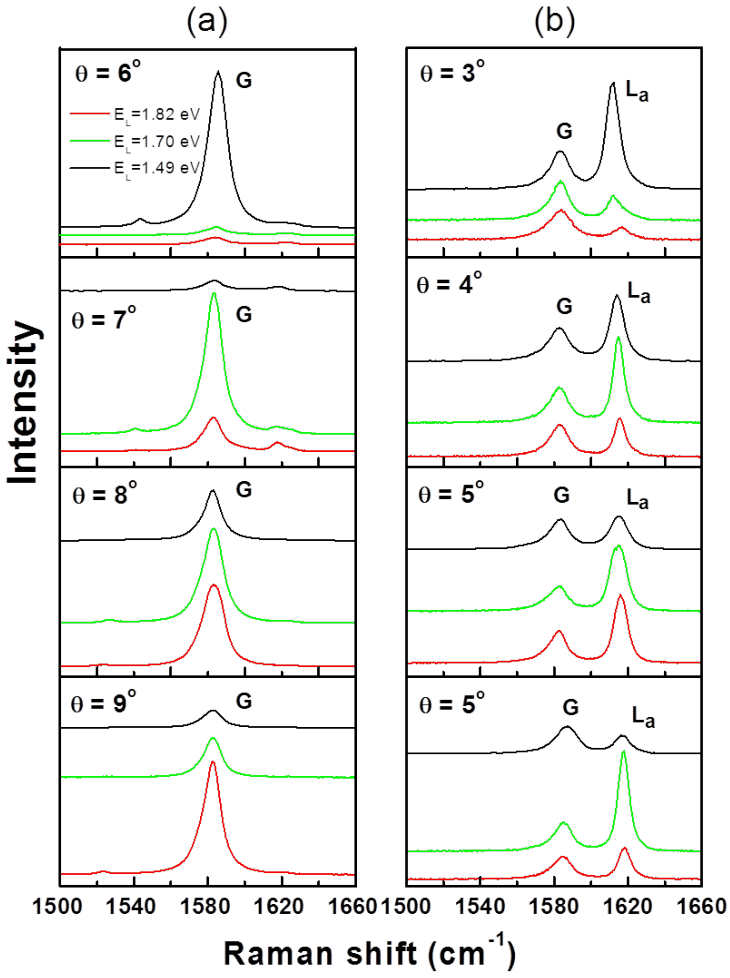

Figure 65 – Raman spectra for samples with low twisting angle θ excited using IR excitation. (a) Interlayer case, (b) intralayer case.

Bibliography

ACS; IACS. *American Chemical Society International Historic Chemical Landmarks. The Raman Effect*. 1998. Disponível em: <http://www.acs.org/content/acs/en/education/whatischemistry/landmarks/ramaneffect.html>. Citado 3 vezes nas páginas ii, 17, and 18.

BALANDIN, A. A. et al. Superior thermal conductivity of single-layer graphene. *Nano Letters*, v. 8, n. 3, p. 902–907, 2008. PMID: 18284217. Disponível em: <http://dx.doi.org/10.1021/nl0731872>. Citado na página 9.

BERGER, C. et al. Electronic confinement and coherence in patterned epitaxial graphene. *Science*, v. 312, n. 5777, p. 1191–1196, 2006. Disponível em: <http://www.sciencemag.org/content/312/5777/1191.abstract>. Citado na página 12.

BLANK, V. et al. Ultrahard and superhard phases of fullerite c60: Comparison with diamond on hardness and wear. *Diamond and Related Materials*, v. 7, n. 2–5, p. 427 – 431, 1998. ISSN 0925-9635. Disponível em: <http://www.sciencedirect.com/science/article/pii/S092596359700232X>. Citado na página 5.

CAMPOS-DELGADO, J. et al. Raman scattering study of the phonon dispersion in twisted bilayer graphene. *Nano Research*, Tsinghua Press, v. 6, n. 4, p. 269–274, 2013. Citado 6 vezes nas páginas iv, 30, 31, 57, 58, and 64.

CANCADO, L. et al. Influence of the atomic structure on the raman spectra of graphite edges. *Physical review letters*, APS, v. 93, n. 24, p. 247401, 2004. Citado na página 36.

CANcADO, L. G. et al. General equation for the determination of the crystallite size la of nanographite by raman spectroscopy. *Applied Physics Letters*, v. 88, n. 16, p. 163106, 2006. Disponível em: <http://dx.doi.org/10.1063/1.2196057>. Citado na página 31.

CAROZO, V. et al. Resonance effects on the raman spectra of graphene superlattices. *Physical Review B*, American Physical Society, v. 88, n. 8, p. 085401, 2013. Citado 9 vezes nas páginas iv, v, 30, 31, 32, 52, 57, 58, and 59.

CAROZO, V. et al. Raman signature of graphene superlattices. *Nano letters*, American Chemical Society, v. 11, n. 11, p. 4527–4534, 2011. Citado 6 vezes nas páginas iii, 29, 30, 31, 57, and 58.

CHOI, T.-Y. et al. Measurement of the thermal conductivity of individual carbon nanotubes by the four-point three- method. *Nano Letters*, v. 6, n. 8, p. 1589–1593, 2006. PMID: 16895340. Disponível em: <http://dx.doi.org/10.1021/nl060331v>. Citado na página 5.

CONG, C. et al. Raman characterization of aba- and abc-stacked trilayer graphene. *ACS nano*, v. 5 11, p. 8760–8, 2011. Citado na página 25.

ECKMANN, A. et al. Raman fingerprint of aligned graphene/h-bn superlattices. *Nano Letters*, v. 13, n. 11, p. 5242–5246, 2013. PMID: 24156357. Disponível em: <http://dx.doi.org/10.1021/nl402679b>. Citado na página 66.

ELIAS, D. et al. Dirac cones reshaped by interaction effects in suspended graphene. *Nature Physics*, Nature Publishing Group, v. 7, n. 9, p. 701–704, 2011. Citado na página 8.

ELIEL, G. S. N. et al. Raman excitation profile of the g-band enhancement in twisted bilayer graphene. *Brazilian Journal of Physics*, Aug 2017. ISSN 1678-4448. Disponível em: <https://doi.org/10.1007/s13538-017-0526-8>. Citado 2 vezes nas páginas 47 and 59.

FANTINI, C. et al. Optical transition energies for carbon nanotubes from resonant raman spectroscopy: Environment and temperature effects. *Phys. Rev. Lett.*, American Physical Society, v. 93, p. 147406, Sep 2004. Disponível em: <http://link.aps.org/doi/10.1103/PhysRevLett.93.147406>. Citado 2 vezes nas páginas 40 and 53.

FASOLINO, A.; LOS, J.; KATSNELSON, M. I. Intrinsic ripples in graphene. *Nature materials*, Nature Publishing Group, v. 6, n. 11, p. 858–861, 2007. Citado na página 1.

FERRARI, A. C. et al. Raman spectrum of graphene and graphene layers. *Phys. Rev. Lett.*, American Physical Society, v. 97, p. 187401, Oct 2006. Disponível em: <http://link.aps.org/doi/10.1103/PhysRevLett.97.187401>. Citado 2 vezes nas páginas 23 and 25.

GEIM, A.; GRIGORIEVA, I. Van der waals heterostructures. *Nature*, Nature Publishing Group, v. 499, n. 7459, p. 419–425, 2013. Citado 4 vezes nas páginas i, 3, 4, and 47.

GEIM, A. K.; NOVOSELOV, K. S. The rise of graphene. *Nat Mater*, Nature Publishing Group, v. 6, n. 3, p. 183–191, mar. 2007. ISSN 1476-1122. Disponível em: <http://dx.doi.org/10.1038/nmat1849>. Citado 2 vezes nas páginas i and 6.

GUPTA, A. K. et al. Nondispersive raman d band activated by well-ordered interlayer interactions in rotationally stacked bilayer graphene. *Phys. Rev. B*, American Physical Society, v. 82, p. 241406, Dec 2010. Disponível em: <https://link.aps.org/doi/10.1103/PhysRevB.82.241406>. Citado 6 vezes nas páginas iii, 27, 28, 57, 58, and 65.

HARTSCHUH, A. New techniques for carbon-nanotube study and characterization. In: _____. *Carbon Nanotubes: Advanced Topics in the Synthesis, Structure, Properties and Applications*. Berlin, Heidelberg: Springer Berlin Heidelberg, 2008. p. 371–393. ISBN 978-3-540-72865-8. Disponível em: <https://doi.org/10.1007/978-3-540-72865-8_12>. Citado na página 10.

HASS, J. et al. Why multilayer graphene on 4h-SiC(000$\bar{1}$) behaves like a single sheet of graphene. *Phys. Rev. Lett.*, American Physical Society, v. 100, p. 125504, Mar 2008. Disponível em: <http://link.aps.org/doi/10.1103/PhysRevLett.100.125504>. Citado 2 vezes nas páginas i and 12.

HAVENER, R. W. et al. Van hove singularities and excitonic effects in the optical conductivity of twisted bilayer graphene. *Nano Letters*, v. 14, n. 6, p. 3353–3357, 2014. PMID: 24798502. Disponível em: <http://dx.doi.org/10.1021/nl500823k>. Citado 7 vezes nas páginas vii, 51, 52, 53, 59, 62, and 63.

HAVENER, R. W. et al. Angle-resolved raman imaging of interlayer rotations and interactions in twisted bilayer graphene. *Nano letters*, American Chemical Society, v. 12, n. 6, p. 3162–3167, 2012. Citado 10 vezes nas páginas iii, 26, 27, 34, 40, 41, 43, 48, 50, and 57.

HE, R. et al. Observation of low energy raman modes in twisted bilayer graphene. *Nano Letters*, v. 13, n. 8, p. 3594–3601, 2013. PMID: 23859121. Disponível em: <http://dx.doi.org/10.1021/nl4013387>. Citado na página 49.

IIJIMA, S. Helical microtubules of graphitic carbon. *nature*, London), v. 354, n. 6348, p. 56–58, 1991. Citado na página 5.

Jin, C. et al. Interlayer electron-phonon coupling in WSe_2/hBN heterostructures. *Nature Physics*, v. 13, p. 127–131, fev. 2017. Citado na página 57.

JORIO, A. et al. *Raman spectroscopy in graphene related systems*. Wiley-VCH, 2011. ISBN 9783527408115. Disponível em: <http://www.worldcat.org/isbn/9783527408115>. Citado 4 vezes nas páginas i, 9, 10, and 72.

KATAURA, H. H. et al. Optical properties of single-wall carbon nanotubes. *Synth. Met.*, v. 103, p. 2555–2558, 1999. Citado na página 40.

KIM, B. et al. Inkjet printed circuits based on ambipolar and p-type carbon nanotube thin-film transistors. *Scientific Reports*, Nature Publishing Group, v. 7, 2 2017. ISSN 2045-2322. Citado na página 6.

KIM, K. et al. Raman spectroscopy study of rotated double-layer graphene: Misorientation-angle dependence of electronic structure. *Phys. Rev. Lett.*, American Physical Society, v. 108, p. 246103, Jun 2012. Disponível em: <http://link.aps.org/doi/10.1103/PhysRevLett.108.246103>. Citado 8 vezes nas páginas i, iv, 13, 33, 42, 48, 50, and 57.

Kroto, H. W. et al. C(60): Buckminsterfullerene. , v. 318, p. 162, nov. 1985. Citado na página 5.

LAISSARDIERÈ, G. Trambly de; MAYOU, D.; MAGAUD, L. Localization of dirac electrons in rotated graphene bilayers. *Nano Letters*, v. 10, n. 3, p. 804–808, 2010. Citado na página 40.

LAPSHIN, R. V. Automatic lateral calibration of tunneling microscope scanners. *Review of Scientific Instruments*, v. 69, n. 9, 1998. Citado na página 1.

LI, G.; LUICAN, A.; ANDREI, E. Y. Scanning tunneling spectroscopy of graphene on graphite. *Phys. Rev. Lett.*, American Physical Society, v. 102, p. 176804, Apr 2009. Disponível em: <http://link.aps.org/doi/10.1103/PhysRevLett.102.176804>. Citado na página 12.

LI, G. et al. Observation of van hove singularities in twisted graphene layers. *Nature Physics*, Nature Publishing Group, v. 6, n. 2, p. 109–113, 2009. Citado 2 vezes nas páginas 12 and 48.

LU, C.-C. et al. Twisting bilayer graphene superlattices. *ACS Nano*, v. 7, n. 3, p. 2587–2594, 2013. PMID: 23448165. Disponível em: <http://dx.doi.org/10.1021/nn3059828>. Citado 8 vezes nas páginas iv, 34, 35, 36, 41, 49, 57, and 77.

MALARD, L. et al. Raman spectroscopy in graphene. *Physics Reports*, v. 473, n. 5–6, p. 51 – 87, 2009. ISSN 0370-1573. Disponível em: <http://www.sciencedirect.com/science/article/pii/S0370157309000520>. Citado 6 vezes nas páginas ii, 21, 23, 24, 25, and 42.

MAULTZSCH, J. et al. Phonon dispersion in graphite. *Phys. Rev. Lett.*, American Physical Society, v. 92, p. 075501, February 2004. Citado na página 77.

MCCANN, E.; FAL'KO, V. I. Landau-level degeneracy and quantum hall effect in a graphite bilayer. *Phys. Rev. Lett.*, American Physical Society, v. 96, p. 086805, Mar 2006. Disponível em: <http://link.aps.org/doi/10.1103/PhysRevLett.96.086805>. Citado na página 11.

MELE, E. J. Commensuration and interlayer coherence in twisted bilayer graphene. *Phys. Rev. B*, American Physical Society, v. 81, p. 161405, Apr 2010. Disponível em: <http://link.aps.org/doi/10.1103/PhysRevB.81.161405>. Citado na página 13.

MERMIN, N. D. Crystalline order in two dimensions. *Phys. Rev.*, American Physical Society, v. 176, p. 250–254, Dec 1968. Disponível em: <http://link.aps.org/doi/10.1103/PhysRev.176.250>. Citado na página 1.

MIRO, P.; AUDIFFRED, M.; HEINE, T. An atlas of two-dimensional materials. *Chem. Soc. Rev.*, The Royal Society of Chemistry, v. 43, p. 6537–6554, 2014. Disponível em: <http://dx.doi.org/10.1039/C4CS00102H>. Citado 5 vezes nas páginas i, 1, 2, 3, and 47.

MOON, P.; KOSHINO, M. Energy spectrum and quantum hall effect in twisted bilayer graphene. *Phys. Rev. B*, v. 85, p. 195458, 2012. Citado na página 40.

MOON, P.; KOSHINO, M. Optical absorption in twisted bilayer graphene. *Phys. Rev. B*, American Physical Society, v. 87, p. 205404, May 2013. Disponível em: <http://link.aps.org/doi/10.1103/PhysRevB.87.205404>. Citado 6 vezes nas páginas ii, 15, 16, 48, 51, and 55.

MORELL, E. S. et al. Flat bands in slightly twisted bilayer graphene: Tight-binding calculations. *Phys. Rev. B*, v. 82, p. 121407, 2010. Citado na página 40.

MOURA, L. G. et al. Raman excitation profile of the G band in single-chirality carbon nanotubes. *Phys. Rev. B*, v. 89, p. 035402, 2014. Citado na página 40.

NETO, A. H. C.; GUINEA, F. Electron-phonon coupling and raman spectroscopy in graphene. *Phys. Rev. B*, American Physical Society, v. 75, p. 045404, Jan 2007. Disponível em: <https://link.aps.org/doi/10.1103/PhysRevB.75.045404>. Citado na página 21.

NETO, A. H. C. et al. The electronic properties of graphene. *Rev. Mod. Phys.*, American Physical Society, v. 81, p. 109–162, Jan 2009. Disponível em: <http://link.aps.org/doi/10.1103/RevModPhys.81.109>. Citado 4 vezes nas páginas i, 8, 9, and 11.

NI, Z. et al. g-band raman double resonance in twisted bilayer graphene: Evidence of band splitting and folding. *Phys. Rev. B*, American Physical Society, v. 80, p. 125404, Sep 2009. Disponível em: <http://link.aps.org/doi/10.1103/PhysRevB.80.125404>. Citado 8 vezes nas páginas iii, 25, 26, 40, 41, 43, 48, and 57.

NI, Z. et al. Reduction of fermi velocity in folded graphene observed by resonance raman spectroscopy. *Phys. Rev. B*, v. 77, p. 235403, 2008. Citado na página 40.

Nika, D. L.; Balandin, A. A. Two-dimensional phonon transport in graphene. *Journal of Physics Condensed Matter*, v. 24, n. 23, p. 233203, jun. 2012. Citado na página 9.

NOVOSELOV, K. S. et al. Electric field effect in atomically thin carbon films. *Science*, v. 306, n. 5696, p. 666–669, 2004. Disponível em: <http://www.sciencemag.org/content/306/5696/666.abstract>. Citado 2 vezes nas páginas 1 and 47.

NUGRAHA, A. R. T. et al. Dielectric constant model for environmental effects on the exciton energies of single wall carbon nanotubes. *Appl. Phys. Lett.*, v. 97, p. 091905, 2010. Citado na página 40.

PAINTER, G. S.; ELLIS, D. E. Electronic band structure and optical properties of graphite from a variational approach. *Phys. Rev. B*, American Physical Society, v. 1, p. 4747–4752, Jun 1970. Disponível em: <https://link.aps.org/doi/10.1103/PhysRevB.1.4747>. Citado na página 7.

PIMENTA, M. A. et al. Studying disorder in graphite-based systems by raman spectroscopy. *Phys. Chem. Chem. Phys.*, The Royal Society of Chemistry, v. 9, p. 1276–1290, 2007. Disponível em: <http://dx.doi.org/10.1039/B613962K>. Citado na página 61.

PIMENTA, M. A. et al. Raman modes of metallic carbon nanotubes. *Phys. Rev. B*, American Physical Society, v. 58, p. R16016–R16019, Dec 1998. Disponível em: <http://link.aps.org/doi/10.1103/PhysRevB.58.R16016>. Citado 2 vezes nas páginas 5 and 40.

RAMAN, C. V.; KRISHNAN, K. S. A New Type of Secondary Radiation. *Nature*, v. 121, p. 501–502, 1928. Citado na página 17.

RIBEIRO, H. et al. Origin of van hove singularities in twisted bilayer graphene. *Carbon*, v. 90, p. 138 – 145, 2015. ISSN 0008-6223. Disponível em: <http://www.sciencedirect.com/science/article/pii/S0008622315002857>. Citado 4 vezes nas páginas 49, 52, 57, and 59.

RIGHI, A. et al. Graphene moiré patterns observed by umklapp double-resonance raman scattering. *Phys. Rev. B*, American Physical Society, v. 84, p. 241409, Dec 2011. Disponível em: <http://link.aps.org/doi/10.1103/PhysRevB.84.241409>. Citado 7 vezes nas páginas iii, 28, 29, 57, 58, 61, and 65.

RIGHI, A. et al. Resonance raman spectroscopy in twisted bilayer graphene. *Solid State Communications*, v. 175–176, p. 13 – 17, 2013. ISSN 0038-1098. Special Issue: Graphene V: Recent Advances in Studies of Graphene and Graphene analogues. Disponível em: <http://www.sciencedirect.com/science/article/pii/S0038109813002548>. Citado 3 vezes nas páginas 57, 58, and 59.

SAITO, R.; DRESSELHAUS, G.; DRESSELHAUS, M. S. Trigonal warping effect of carbon nanotubes. *Phys. Rev. B*, v. 61, p. 2981–2990, 2000. Citado na página 40.

SAITO, R.; FANTINI, C.; JIANG, J. Excitonic states and resonance raman spectroscopy of single-wall carbon nanotubes. *Topics in Applied Physics*, v. 111, p. 251–286, 2008. Citado na página 40.

SAITO, R. et al. Electronic structure of chiral graphene tubules. *Applied Physics Letters*, v. 60, n. 18, 1992. Citado 2 vezes nas páginas 5 and 9.

SAMSONIDZE, G. G. et al. Family behavior of the optical transition energies in single-wall carbon nanotubes of smaller diameters. *Appl. Phys. Lett.*, v. 85, n. 23, p. 5703–5705, 2004. Citado na página 40.

SANTOS, J. M. B. Lopes dos; PERES, N. M. R.; NETO, A. H. C. Graphene bilayer with a twist: Electronic structure. *Phys. Rev. Lett.*, American Physical Society, v. 99, p. 256802, Dec 2007. Disponível em: <http://link.aps.org/doi/10.1103/PhysRevLett.99.256802>. Citado 5 vezes nas páginas 12, 13, 40, 48, and 55.

SASAKI, K. et al. Kohn anomalies in graphene nanoribbons. *Phys. Rev. B*, v. 80, p. 155450, 2009. Citado na página 46.

SATO, K. et al. Zone folding effect in raman g-band intensity of twisted bilayer graphene. *Phys. Rev. B*, American Physical Society, v. 86, p. 125414, Sep 2012. Disponível em: <http://link.aps.org/doi/10.1103/PhysRevB.86.125414>. Citado 8 vezes nas páginas i, 13, 14, 39, 40, 45, 48, and 55.

SCHMIDT, H. et al. Tunable graphene system with two decoupled monolayers. *Applied Physics Letters*, AIP Publishing, v. 93, n. 17, p. 172108, 2008. Citado na página 12.

SHALLCROSS, S. et al. Electronic structure of turbostratic graphene. *Phys. Rev. B*, American Physical Society, v. 81, p. 165105, Apr 2010. Disponível em: <http://link.aps.org/doi/10.1103/PhysRevB.81.165105>. Citado 2 vezes nas páginas 14 and 40.

SMEKAL, A. Zur quantentheorie der dispersion. *Naturwissenschaften*, v. 11, n. 43, p. 873–875, Oct 1923. ISSN 1432-1904. Disponível em: <https://doi.org/10.1007/BF01576902>. Citado na página 17.

TREACY, M. M. J.; EBBESEN, T. W.; GIBSON, J. M. Exceptionally high young's modulus observed for individual carbon nanotubes. *Nature*, v. 381, n. 6584, p. 678, Jun 20 1996. Copyright - Copyright Macmillan Journals Ltd. Jun 20, 1996; Última atualização em - 2012-11-14; CODEN - NATUAS. Disponível em: <https://search.proquest.com/docview/204468346?accountid=134127>. Citado na página 5.

VENEZUELA, P.; LAZZERI, M.; MAURI, F. Theory of double-resonant raman spectra in graphene: Intensity and line shape of defect-induced and two-phonon bands. *Phys. Rev. B*, American Physical Society, v. 84, p. 035433, Jul 2011. Disponível em: <http://link.aps.org/doi/10.1103/PhysRevB.84.035433>. Citado 6 vezes nas páginas ii, 8, 24, 25, 40, and 77.

VIJAYARAGHAVAN, A. et al. Ultra-large-scale directed assembly of single-walled carbon nanotube devices. *Nano Letters*, v. 7, n. 6, p. 1556–1560, 2007. PMID: 17488050. Disponível em: <http://dx.doi.org/10.1021/nl0703727>. Citado na página 6.

WALLACE, P. R. The band theory of graphite. *Phys. Rev.*, American Physical Society, v. 71, p. 622–634, May 1947. Disponível em: <https://link.aps.org/doi/10.1103/PhysRev.71.622>. Citado 2 vezes nas páginas 6 and 7.

WANG, Y. et al. Resonance raman spectroscopy of g-line and folded phonons in twisted bilayer graphene with large rotation angles. *Applied Physics Letters*, v. 103, n. 12, p. –, 2013. Disponível em: <http://scitation.aip.org/content/aip/journal/apl/103/12/10.1063/1.4821434>. Citado 11 vezes nas páginas iv, vii, 30, 32, 36, 49, 50, 57, 58, 62, and 65.

WEI, L. et al. Thermal conductivity of isotopically modified single crystal diamond. *Phys. Rev. Lett.*, American Physical Society, v. 70, p. 3764–3767, Jun 1993. Disponível em: <http://link.aps.org/doi/10.1103/PhysRevLett.70.3764>. Citado na página 5.

YAN, J.-A.; RUAN, W. Y.; CHOU, M. Y. Phonon dispersions and vibrational properties of monolayer, bilayer, and trilayer graphene: Density-functional perturbation theory. *Phys. Rev. B*, American Physical Society, v. 77, p. 125401, Mar 2008. Disponível em: <https://link.aps.org/doi/10.1103/PhysRevB.77.125401>. Citado na página 11.